INAUGURAL - DISSERTATION
zur
Erlangung der Doktorwürde
der
Naturwissenschaftlich - Mathematischen
Gesamtfakultät
der Ruprecht - Karls - Universität
Heidelberg

vorgelegt von
M.Sc. Lukas Brückner
aus Nürnberg

Tag der mündlichen Prüfung: 02.12.2016

Exploring the Potential of Nonlinear Optical Microscopy with Tailored Femtosecond Pulses

Gutachter: Prof. Dr. Marcus Motzkus
Prof. Dr. Dirk-Peter Herten

Abstract

In this thesis, the high degree of control offered by the combination of a broadband femtosecond excitation source and a pulse shaper is exploited to achieve high spectral resolution nonlinear optical microscopy. Especially the coherent anti-Stokes Raman scattering (CARS) process is very important for nonlinear microscopy since it provides label-free three-dimensional contrast based on the vibrational atomic motion. The flexibility of the developed setup not only allows to switch between optimal conditions for the generation of CARS and other nonlinear signals but enables their simultaneous measurement. The complementary contrast of signals like second-harmonic generation (SHG), two-photon fluorescence (TPEF) and the CARS process in a multimodal imaging scheme provides additional information to identify structures and the composition of complex biological samples. It is shown how the individual control over the frequencies taking part in the CARS process can be used to achieve resonant vibrational imaging, overcoming the limitations usually associated with the unspecific excitation of using broadband pulses. Within this *tailored spectral focusing* approach, CARS signals are enhanced by an order of magnitude and SHG and TPEF intensities are boosted even more, as demonstrated by multimodal imaging of skin tissue. Furthermore, the method can be directly applied to control the difference frequency generation process occurring when focusing the laser on a nonlinear crystal, to form a tunable broadband infrared (IR) light source. Besides the direct characterization of the IR spectrum by this method, absorption spectroscopy becomes possible in a single-beam approach. A whole new frequency region is thereby unlocked, paving the way for retrieving complementary information from Raman as well as IR interactions in the same setup for the first time.

Zusammenfassung

Im Rahmen dieser Doktorarbeit werden die vielseitigen Möglichkeiten der Phasenformung eines breitbandigen Femtosekundenlasers im Hinblick auf die Weiterentwicklung der spektral aufgelösten nichtlineare optische Mikroskopie aufgezeigt. Insbesondere kohärente anti-Stokes Raman Streuung (CARS) ist hier von Interesse, da es einen markierungsfreien Kontrast auf Basis von Molekülschwingungen und darüber hinaus intrinsische, dreidimensionale Auflösung bietet. Durch die hohe Flexibilität des Messaufbaus wird nicht nur die Optimierung einzelner nichtlinearer Signale, sondern auch deren simultane Detektion ermöglicht. Die erzeugten Signale von Zwei-Photonen-Fluoreszenz (TPEF), Frequenzverdopplung (SHG) und CARS liefern komplementäre Informationen und ermöglichen so die Identifizierung von Strukturen und Zusammensetzung komplexer biologischer Proben im Rahmen sogenannter multimodaler Bildgebung. Der Pulsformer ermöglicht es zudem, die Nachteile der unspezifischen Anregung mit breitbandigen Pulsen zu umgehen. Durch die spektrale Fokussierung der Energie auf ein Schwingungslevel kann resonanter CARS Kontrast erzeugt werden. Die individuelle Kontrolle der erzeugenden Frequenzkomponenten des Signals erreicht darüber hinaus eine bedeutende Steigerung der CARS, SHG und TPEF Intensitäten, was durch multimodale Bildgebung menschlicher Hautproben gezeigt wird. Die entwickelte Methode kann weiterhin direkt zur Kontrolle der Differenzfrequenzmischung (DFG) in einem nichtlinearen Kristall genutzt werden. So ist es nicht nur möglich das erzeugte breitbandige Infrarotspektrum zu charakterisieren, sondern zugleich IR-Absorptionsspektroskopie in einem Einzelstrahlaufbau durchzuführen. Die Erschließung des Infrarotbereichs erlaubt es erstmals, Informationen über IR und Raman Anregungen in einem Aufbau zu erhalten.

Publications

- *A Tunable Infrared Light Source for Single-Beam Absorption Spectroscopy*, L. Brückner and M. Motzkus, in preparation

- *Exploring the Potential of Tailored Spectral Focusing*, L. Brückner, T. Buckup and M. Motzkus in J. Opt. Soc. B **33** (2016), 1482-1491

- *Exploring the Potential of Tailored Probing for a Flexible Coherent Raman Excitation Scheme*, L. Brückner, T. Buckup and M. Motzkus, Proceedings Ultrafast Phenomena XX, Springer, Berlin (2016), in press

- *Enhancement of Coherent Anti-Stokes Raman Signal via Tailored Probing in Spectral Focusing*, L. Brückner, T. Buckup and M. Motzkus in Opt. Lett. **40** (2015), 5204-5207

- *Multimodal Nonlinear Optical Microscopy with Shaped 10 fs Pulses*, J. Rehbinder*, L. Brückner*, A. Wipfler, T. Buckup and M. Motzkus in Opt. Express **22** (2014), 28790-28797; * Authors contributed equally to this work

Oral Presentations

- *Exploring the Potential of Tailored Spectral Focusing*, L. Brückner, T. Buckup and M. Motzkus; ECONOS 2016, Gothenburg, Sweden.

- *Enhancement of CARS Signal via Tailored Probing in Spectral Focusing*, L. Brückner, T. Buckup and M. Motzkus; DPG 2016, Hannover, Germany.

- *Multimodal nonlinear optical microscopy with shaped 10 fs pulses*, L. Brückner, J. Rehbinder, T. Buckup and M. Motzkus; MicroCOR 2014, Heidelberg, Germany.

- *Biological samples imaged by multimodal nonlinear microscopy with 10 fs pulses*, L. Brückner, J. Rehbinder, T. Buckup and M. Motzkus; MicroCOR winter school 2014, Les Houches, France.

- *Biological samples imaged by multimodal nonlinear microscopy with 10fs pulses*, L. Brückner, J. Rehbinder, T. Buckup and M. Motzkus; DPG 2013, Hannover, Germany.
- *Tailored broadband pulses for multimodal nonlinear imaging of biological samples*, J. Rehbinder, L. Brückner, A. Wipfler, T. Buckup and M. Motzkus; Focus on microscopy 2013, Maastricht, Netherlands.

Poster Presentations

- *Exploring the Potential of Tailored Probing for a Flexible Coherent Raman Excitation Scheme*, L. Brückner, T. Buckup and M. Motzkus; Ultrafast Phenomena XX 2016, Santa Fe, USA.
- *Spectral Focusing with Flexible Shaped Laser Pulses for Chemical Imaging*, L. Brückner, T. Buckup and M. Motzkus; DPG 2016, Hannover, Germany.

Table of Contents

1 Nonlinear Optical Imaging

1.1 Motivation

The general aim in optical microscopy is to achieve distinct contrast between different structures or molecules, usually at micrometric or even nanometric spatial resolution. Many specialized techniques have been developed to meet the needs of a variety of fields ranging from materials science to biomedical imaging. Although invented already in the first half of the 20^{th} century, Raman and fluorescence microscopy in particular are both still very active fields of research. The unmatched sensitivity of fluorescence as well as the intrinsic vibrational contrast provided by Raman microscopy led to many discoveries in the life-sciences. Especially the development of sub-diffraction limited, or 'super-resolution' fluorescence microscopy had a major impact on many connected fields. Consequently, the Nobel prize in chemistry 2014 was awarded to E. Betzig [1, 2], W. E. Moerner [3, 4] and S. W. Hell [5, 6], highlighting the importance of optical microscopy in general.

Nonetheless, the mentioned techniques are limited to certain samples and are not generally applicable without restrictions. For biomolecular imaging in particular, there still is a strong demand for powerful new techniques offering endogenous contrast while maintaining the sample integrity [7]. The ideal technique should not only show intrinsic label-free contrast with a high spectral and three-dimensional spatial resolution but should also provide high signal intensities to enable video-rate imaging on live samples. The development of nonlinear optical techniques has opened a door in this respect [7–14]. In particular, coherent Raman processes have shown to provide vibrational contrast in biological tissues at imaging speeds up to video-rate for live cell imaging [15, 16]. Combining several simultaneously generated nonlinear signals in a multimodal approach furthermore provides additional contrast and complementary information about structures and the molecular composition, as shown in fig. 1.1 [7].

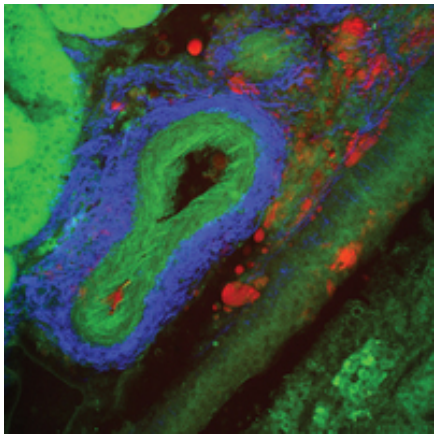

Figure 1.1: 300 µm x 300 µm multimodal image of a blood vessel in kidney tissue. Adipose cells are shown by the coherent anti-Stokes Raman scattering (CARS) signal in red, collagen generates the blue second-harmonic signal (SHG) while intracellular NADH as well as elastin in the vascular wall leads to two-photon excited fluorescence (TPEF, green). The pixel dwell-time was only 4 µs. The image and explanations thereof are taken from [7].

Fig. 1.2 shows the energy diagrams and the signal generation mechanisms of some important microscopy techniques grouped into linear and nonlinear methods. As mentioned above, the most prominent and widely used example is fluorescence microscopy, where an electronic state of a molecule is excited and leads to fluorescence emission. Besides many advantages like the unmatched sensitivity or the possibility to perform super-resolution microscopy, the method requires labeling with specifically designed fluorescent markers. This poses serious problems due to possible alterations of the functionality of molecules and structures. Also, the labeling itself can be challenging and is only applicable to known samples. Although different fluorescent molecules can in some cases be distinguished based on their absorption or emission profiles, the actual contrast is actually achieved by the selectivity of the labeling process [14]. In vibrational spectroscopy the contrast arises from the vibrational resonances of the molecules under study. In infrared (IR) absorption microscopy the IR-active vibrational bands are directly excited by the incoming light. On the downside, standard refractive optics cannot be used and even diffraction-limited resolutions are only in the range of several micrometers. Observing details on the cellular level is therefore not possible. Also, the strong IR-absorption band of water is problematic when

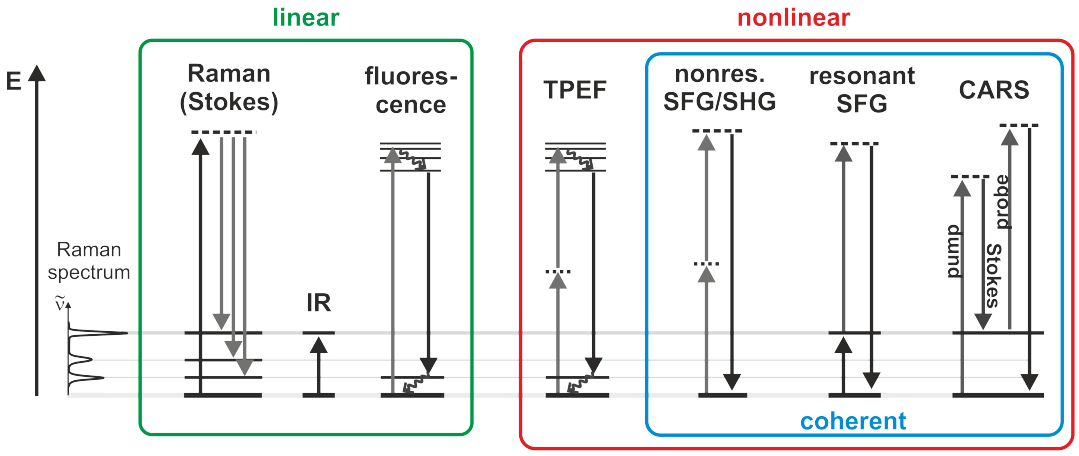

Figure 1.2: Examples of widely used spectroscopic techniques grouped into linear and nonlinear methods. Additionally, the coherent signal generation mechanisms are highlighted (blue box). While Raman, IR, SFG and CARS microscopy contain vibrationally resonant information, SHG, fluorescence and TPEF are generated under vibrationally nonresonant conditions. Note that the differences of common experimental excitation energies ($\sim 12\,500\,\mathrm{cm}^{-1}$) and the energy levels (max. $\sim 3000\,\mathrm{cm}^{-1}$) is higher than shown here. The dotted lines represent virtual and the solid lines vibrational levels.

imaging biological samples [13].

By exploiting the spontaneous Raman process, these disadvantages can be overcome. Incoming laser light interacts with the electron cloud of a molecule, which induces a dipole and leads to a macromolecular polarization by the joint interaction of many molecules with the laser. The valence electrons are driven with the frequency of the excitation light ω_{exc} and radiate an electric field that is usually referred to as Rayleigh scattering. By coupling of the electron cloud with vibrational motions ω_{vib} that lead to a change of the polarizability, the oscillation frequency is modulated. The Stokes and anti-Stokes frequencies are generated at $\omega = \omega_{\mathrm{exc}} \pm \omega_{\mathrm{vib}}$ [17]. The interaction is usually depicted by virtual levels shown as dashed lines in the energy diagrams (fig. 1.2). The spontaneous Raman process therefore allows to directly measure a vibrational spectrum of a molecule. Furthermore, confocal setups enable imaging with sub-micrometer spatial resolution. Because of the off-resonant excitation, the excitation wavelength can be varied in order to shift the Raman signal to a suitable spectral region. The influence of water absorption is minimized, which

led not only to widespread application in material science but in biological imaging as well. Today, Raman spectroscopy still is the standard technique for vibrational microscopy.

On the downside, the strength of spontaneous Raman signals is generally very low. Due to the small cross sections, only 1 out of 10 million photons is Raman-scattered when light travels through 1 cm of organic liquid [12]. In order to collect spectra with satisfactory signal levels, long integration times are required. Especially in microscopy the signal is reduced even further because of the small interaction volumes and the accordingly small absolute number of atoms within the focal volume. Also, to prevent samples from photo-damage, the laser power cannot be increased infinitely. Methods like resonant Raman or surface enhanced Raman scattering (SERS) [18, 19] have been developed to increase the signal. These techniques require special preparation and circumstances and can therefore not generally be applied. High-speed or even video-rate imaging is thus not possible and requires the development of other methods. Nonlinear techniques on the other hand enable high signal intensities so that even video-rate measurements are possible. Coherent Raman scattering (CRS) techniques, namely coherent anti-Stokes Raman scattering (CARS) and stimulated Raman scattering (SRS), probe the same molecular properties as in Raman spectroscopy with label-free and noninvasive vibrational contrast but with the advantage of high signal intensities. The possibility to perform live cell imaging shows the importance and the potential of these methods [16].

1.2 Description of Nonlinear Optical Signals

The discussed traditional techniques are generated by the interaction of the sample with a single photon and are therefore linearly dependent on the laser intensity. At very high laser intensities, however, higher-order processes that involve the simultaneous interaction of multiple photons can occur (fig. 1.2). Depending on the number of interacting fields, they are classified as 2^{nd}, 3^{rd} or even higher-order processes. The interaction can be described by an expansion of the induced polarization in terms of

the electric field

$$P = \varepsilon_0(\chi^{(1)}\vec{E} + \underbrace{\chi^{(2)}\vec{E}\vec{E} + \chi^{(3)}\vec{E}\vec{E}\vec{E} + \ldots}_{nonlinear}) \quad . \tag{1.1}$$

The excitation laser light polarizes a molecule by slightly separating positive and negative charges in the focus. Because of the extreme intensities the polarization is overdriven, i.e., it does not follow the excitational field but is the source of new frequencies: the nonlinear signals (as expressed in the nonlinear wave equation) [7]. The molecules, represented by the susceptibility $\chi^{(n)}$, act as mixing medium for the frequencies taking part in the nonlinear optical process. In the case of parametric generation (e.g. SHG, CARS in fig. 1.2) energy is solely exchanged between the different fields where the quantum state of the molecules is left unchanged. Other non-parametric processes like two-photon excited fluorescence (TPEF) and SRS lead to an electronic or vibrational excitation of the molecule. The actual nonlinear signal measured by a detector is given by the squared modulus of the nonlinear polarization $I = |P^{(n)}|^2$. Focusing to a small volume not only highly increases their intensity but makes nonlinear signals accessible for microscopy. Because the signal is nonlinearly dependent on the laser intensity, the generation is confined to the focal volume. This intrinsic 3D sectioning capability is one of the main reasons for the wide application, especially in the biomedical sector [9].

Some typical processes used in nonlinear microscopy are depicted together with their corresponding energy schemes in fig. 1.2. Two-photon excited fluorescence **(TPEF)** is a noncoherent process based on two-photon absorption into an excited electronic level with subsequent spontaneous emission of fluorescence. It can be generated by endogenous fluorophores in biological tissue, like NADH, melanin or elastin, or by artificial fluorescent markers [8, 10, 20]. Since usually excitation wavelengths in the near-infrared are used, reduced scattering and the intrinsic 3D sectioning capability leads to an increased penetration depth. Second-harmonic generation **(SHG)** is a special case of sum-frequency generation, where two degenerate photons interact off-resonantly generating signal at 2ω. The method is intrinsically surface-sensitive because it can only be generated in media without inversion symmetry, i.e. at interfaces. On the contrary, in sum-frequency generation **(SFG)** vibrational contrast is

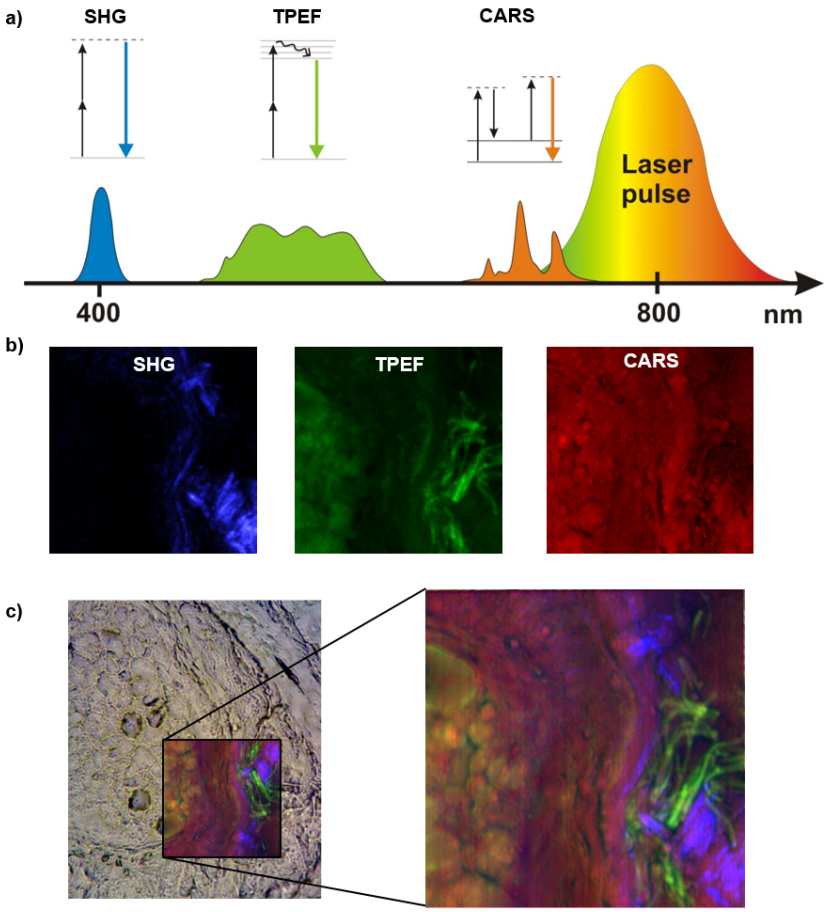

Figure 1.3: Single-beam multimodal nonlinear microscopy on human skin tissue. a) Signal mechanisms and typical spectral position of SHG, TPEF and the CARS process. b) Recorded 100 µm × 100 µm images showing complementary contrast. c) Comparison of a brightfield image and the combined RGB multimodal image of the recorded area. Multimodal imaging provides contrast based on the molecular properties of the sample without staining and thereby allows a detailed look on the sample composition on cellular level.

achieved because of resonant enhancement of the signal when incoming IR laser light matches the energies of molecular vibrations. Coherent anti-Stokes Raman scattering **(CARS)** is a 3rd-order process. The difference of two frequencies, called pump and Stokes, is tuned to match the energy of a Raman level. A coherence of ground and excited state is induced that can be probed by the third frequency to generate the blue-shifted CARS signal. CARS is sensitive to the same vibrational states as in spontaneous Raman scattering.

With an ultrashort femtosecond excitation source, not only one but several nonlinear optical signal can be generated simultaneously. Because each modality is sensitive to specific structures or molecules, combining the provided information into a multimodal image greatly helps in interpreting complex samples [9, 21, 22]. Especially in the biomedical sector, the complementary information provided in multimodal imaging is greatly appreciated and has been frequently used for, e.g., cancer research [23, 24], lipid metabolism [25, 26] or investigation of skin tissue [27, 28]. Multimodal imaging can also easily be implemented in a single-beam CARS setup as shown in fig. 1.3 [22]. The image obtained by combining SHG, TPEF and the nonresonant CARS signal in fig. 1.3c highlights the complementary contrast provided and allows to distinguish structures based on molecular properties with cellular resolution.

Coherent Signal Generation

In spontaneous Raman scattering the generated field is described by radiating dipoles. On the microscopic level the signal of an individual scatterer i is given by $S = |E_i|^2$. Because the vibrational motion of the adjacent molecules is not coupled, they vibrate with a random phase difference. Since the emitted fields are modulated by the vibrational motion, their phase shows a random phase correlation as well. The macroscopic signal is therefore given by the sum of all microscopic signals $S_{Raman} = \sum_i^N |E_i|^2$ [17]. In *coherent* anti-Stokes Raman scattering (valid also for other parametric processes), the electron motion is actively driven and dictated by the phase of the laser fields. To generate a strong macroscopic signal, the microscopic signals generated at different positions have to be in phase with each other as well as with the excitation frequency. This phase-matching condition arises from the fact that not only the energy ($\omega_{CARS} = 2\omega_P - \omega_{St}$) but also the momentum has to be conserved. Due to the dispersion of the refractive index, collinearly traveling excitation frequencies and the generated waves will have different group velocities. The forward directed signals generated at different positions in the sample will not be in phase and no significant macroscopic signal will be generated. Thus, certain noncollinear beam geometries are required in order to minimize the wavevector-mismatch $\Delta k = k_{CARS} - k_P + k_{St} - k_{Pr}$. By choosing the right angles of the interacting beams, dispersion effects are compensated for so that signals generated at different positions in the sample are in phase.

A strong macroscopic signal is generated only in this direction by coherent addition of the individual signals i, which is expressed as $S_{CARS} = |\sum_i^N E_i|^2$. Because the CARS electric field is proportional to the number of scattering molecules, this coherent additional results in a quadratic dependence of the measured signal intensity on the concentration.

However, in nonlinear *microscopy* the phase-matching condition is relaxed and even fulfilled for collinear beam geometries due to what is known as the *tight focusing condition* [29, 30]. When focusing with a high numerical aperture objective, the interaction length is very small so that the walk-off and therefore the phase-difference of different frequencies is minimized. Also, the very large cone angles of the wavevectors achieved assure that combinations of different angles of all contributing frequencies are provided so that there are always enough combinations present that are phase-matched.

1.3 Femtosecond Pulse-Shaping for Optimal Excitation

The generation of multiphoton signals requires extreme light intensities at the sample position, which is usually realized by using pulsed lasers. Pulsed lasers show high peak intensities at low average powers and thereby allow an efficient nonlinear generation with minimized photon-load on the sample. Focusing with a microscope objective then enables label-free imaging with spatial resolutions comparable to confocal Raman microscopy but with considerably higher signal intensities. In order to efficiently generate the signals, the pulses must not only be focused in space but also in time. Compared to continuous-wave illumination, two-photon absorption is enhanced by a factor of $1/(\tau f)^{n-1}$, where τ is the pulse duration and f the repetition rate of the laser [10]. Thus, the signal intensities highly benefit from using shorter pulses in the femtosecond regime.

Laser pulses can be equivalently well described in the time and frequency domain. The domains are connected by Fourier relations, which illustrates that the shortest pulses always show a broadband spectrum and, vice versa, that an ultrashort pulse can only be achieved by the interaction of many different mode-locked (i.e. constant zero phase) frequencies (see also sec. 2.2.1). The titanium-sapphire (Ti:Sa) laser used throughout this work has a transform-limited pulse duration $< 10\,\text{fs}$ and a

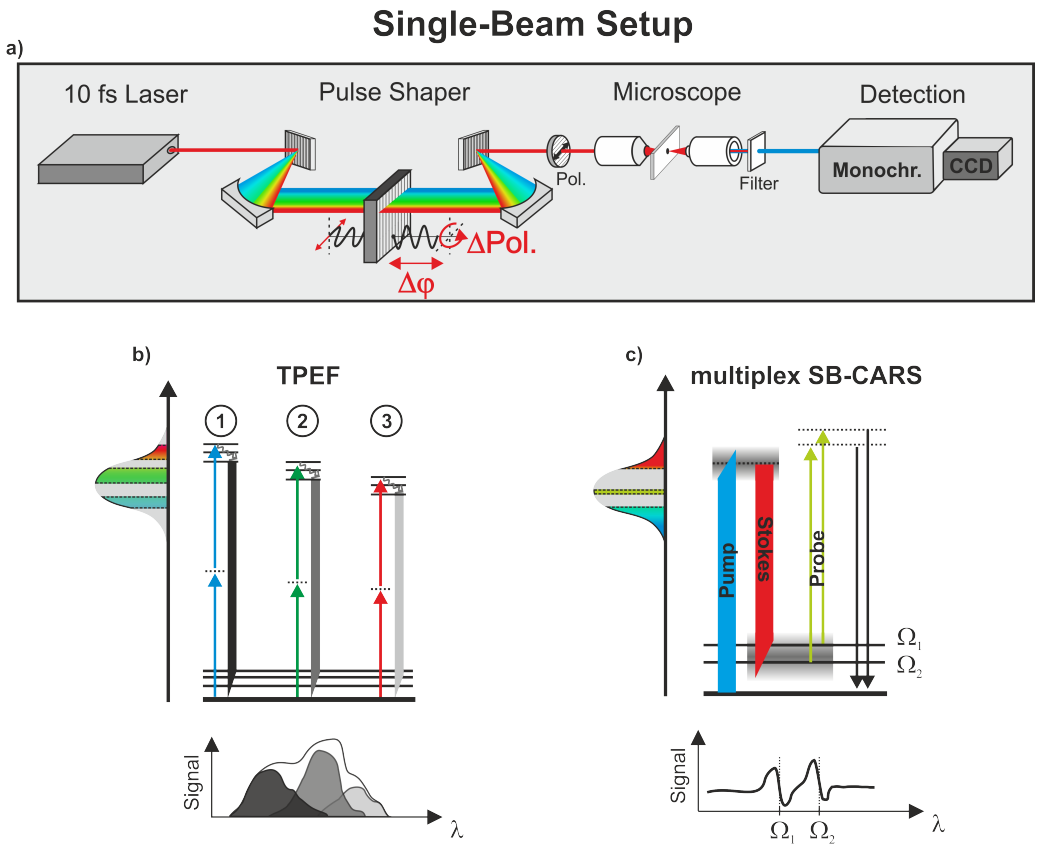

Figure 1.4: a) Experimental setup for single-beam nonlinear microscopy. The broadband spectrum of a sub-10 fs laser is coupled into a pulse shaper, which controls the phase and amplitude of the individual frequencies. A polarizer then translates the polarizations into amplitudes and enables amplitude shaping. Nonlinear signal is generated in the focus of a microscope and, after cutting off the excitation light, detected by a spectrometer or photomultipliers (not shown). b) shows an example how amplitude shaping can be used to distinguish three different fluorophores 1, 2 & 3. A TL-pulse leads to emission from all fluorophores simultaneously (white signal below), while cutting out specific frequencies from the spectrum allows to address each one individually. c) shows how amplitude shaping is used to generate multiplex-CARS spectra. The blue (pump) and red (Stokes) frequencies lead to an excitation of several levels and a narrowband (green) region prevents the lines from overlapping (as would be the case when probing with a broadband pulse) and allows for a distinct mapping in the spectral domain.

spectrum ranging from $670 - 930\,\mathrm{nm}$. Refractive elements have a high influence on the temporal profile of the pulse. Initially very short pulses are stretched in time, making an accurate correction of the introduced dispersion and higher order phase

distortions necessary to assure (nearly) transform-limited pulses at the focus. Usually, this is achieved by precompensating with grating/prism compressors or negatively chirped mirrors but can also be easily done by or in combination with a pulse shaper. Furthermore, using fs-pulses offers additional and very interesting opportunities like time-resolved measurements.

The choice of the optimal excitation source strongly depends on the nonlinear process as well as the contrast one wants to achieve. Broadband femtosecond lasers are highly favorable in terms of signal intensity for instantaneous electronic signals like SHG, TPEF or the nonresonant CARS signal (which provides a map of the density of scatterers). However, when aiming for resonant contrast in CARS microscopy, high background signal prevents the extraction of resonant vibrational information. Here, ps-lasers with bandwidths matching the width of the addressed Raman lines are the best choice [30, 31]. Even for TPEF measurements ps-pulses are sometimes advantageous. A broadband spectrum can lead to the simultaneous excitation of several fluorophores if their spectra are close-lying or even overlapping. By excitation with longer ps-pulses (narrow spectral width) the electronic levels can be addressed and their individual signal specifically collected.

Due to the different generation mechanisms and requirements of specific experiments, there obviously cannot be one perfect laser source for every application. However, the combination of a single sub-10 fs laser with a pulse shaper creates a simple but very flexible and powerful light source as shown in fig. 1.4a. A computer-controlled liquid crystal (LC) mask controls the spectral phase and polarization of the spatially separated frequencies in every of several hundred discrete pixels independently. A polarizer transmits only polarization components along its axis transforming polarization into amplitude shaping. Thereby, light intensities of certain frequencies can be reduced or even whole spectral regions cut out. Signal is generated by focusing the laser beam onto a sample in a microscope and then recorded by a spectrometer. Fig. 1.4b depicts a comparatively simple case where amplitude shaping is applied to differentiate between three fluorophores with different excitation spectra. While all three fluorophores are excited when the whole spectrum is transmitted, cutting out unwanted frequencies allows to address a specific excited state. In this way, the individual emission spectra can be obtained as indicated. A

more complicated example is shown in fig. 1.4c. Here amplitude shaping is used to generate a multiplex-CARS spectrum, i.e., a CARS spectrum is generated in one shot without scanning laser frequencies. Except one small portion, the central region of the spectrum is cut out. The interaction of the pump (blue part) and the Stokes (red part) leads to a broad excitation of all frequencies within their width. The narrowband probe assures that only one signal is generated from each resonance so that a CARS spectrum can be recorded. Note that no vibrational contrast can be achieved when probing with a broad spectrum because the signals from different resonances will overlap on the detector when probed with different frequencies. Additionally, a stronger nonresonant background will be generated (see section 2.1 for a detailed description).

The presented single-beam approach offers many advantages. Different signals usually only accessible by applying special laser sources can now be generated in one setup. Time-consuming frequency tuning of the laser is no longer necessary because all frequencies are already contained within the spectrum. By amplitude shaping, the spectrum can be divided into several light sources, which are intrinsically phase-locked and overlapping in space. Besides the amplitude, the phase of different frequency components can be independently controlled. It is thereby possible to introduce a time-delay in one part while applying a chirp (dispersion) in another region. Since the nonlinear response of a molecule highly depends on the coherent interaction of at least two electric fields, their relative phase has a high influence on the signal generation. Based on the knowledge of their individual phase dependence, different nonlinear signals cannot only be generated with the same broadband laser but their generation efficiency actually coherently controlled by phase shaping.

In summary, nonlinear optical techniques circumvent the need of labeling specific samples or structures. Image contrast is based on molecular properties and noninvasive measurements can be performed with the additional feature of intrinsic three-dimensional resolution. The high signal levels achieved by using pulsed lasers allow to reduce integration times for maximum imaging speed. Especially coherent anti-Stokes Raman scattering is a powerful technique with contrast based on the *resonant* interaction of light with vibrational Raman modes. Unlike in spontaneous Raman measurements, video-rate and even live cell imaging becomes possible [15]. When im-

plementing nonlinear optical imaging in a single-beam setup, pulse shaping enables to control the nonlinear signals. The beauty lies within the flexibility of the setup, where switching between different phase and/or amplitude functions allows to exploit the advantages of femtosecond and picosecond lasers for high signal intensity as well as high spectral resolution. Not only can different nonlinear signals be optimized individually, even simultaneous measurement providing complementary contrast in a multimodal approach is possible. Altogether, the switching speed between different contrast mechanisms as well as the possibility to adapt and even improve many already developed methods from other fields makes femtosecond single-beam pulse shaping a versatile and very powerful tool for spectroscopy and microscopy applications.

1.4 Thesis Outline

In this thesis it will be shown how pulse shaping can be applied to control broadband laser pulses, achieving high spectral resolution and distinct contrast for nonlinear microspectroscopy.

- In order to establish a basis for understanding sophisticated coherent anti-Stokes Raman scattering (CARS) implementations, a detailed theoretical description of the CARS process is given in **chapter 2**. The influence of different pulse lengths on the signal is discussed, motivating the implementation of a single-beam CARS approach. The combination of an ultrabroadband fs-oscillator and a pulse shaper offers many opportunities for coherently controlling nonlinear processes by imprinting tailored phase functions on the spectrum.

- In **chapter 3**, a first approach of controlling the CARS signal is presented. Despite the broadband excitation source, the spectral focusing technique allows to achieve high spectral resolution by flexibly applying equal dispersion to the pump and Stokes frequencies. The method can be directly added as resonant CARS modality to multimodal imaging, as shown on biological tissue. A general time-frequency picture provides a deeper understanding of the underlying idea and paves the way for an important development: the independent control of all frequency regions participating in the signal generation. Thereby, a signal

increase of one order of magnitude is obtained. Furthermore, it will be shown how the independent control can be exploited to achieve contrast based on the coherence times of different vibrations, as well as the applicability throughout the spectrum even reaching the fingerprint region.

- The potential and broad applicability of the developed concept is presented in **chapter 4**. A broadband infrared spectrum can be obtained by difference frequency generation (DFG) of a broadband Ti:Sa excitation source in a suited nonlinear crystal. It is shown how pulse shaping allows to mimic interferometric measurements to easily characterize the generated spectrum through Fourier-transformations. More importantly, the spectral focusing approach can be directly applied for controlling the IR generation to obtain a tunable infrared light source. It is presented how this implementation cannot only be used to characterize the IR spectrum in a precise way, but also how it actually enables performing infrared absorption spectroscopy starting from only a single excitation source for the first time.

- By implementing a multiplex approach in the single-beam setup, it is possible to record a full CARS spectrum in a single shot measurement. However, to retrieve Raman-like vibrational information, four measurements are required. In **chapter 5**, a concept is developed that allows to increase the recording speed tremendously. The potential to record the desired spectra in a single measurement within only a few milliseconds is presented in simulations and demonstrated experimentally.

- In **chapter 6**, the control over yet another nonlinear process is explored for pulse compression. Applying combined phase and amplitude shaping to sum-frequency generation (SFG) allows to individually retrieve the spectral phase of small frequency regions from the broadband pulse. It is explained how this idea enables precise phase compensation even in the low-intensity wings of the spectrum, not accounted for in other pulse compression methods. The working principle is shown in detailed simulations and on experimental results. Challenges in the current experimental implementation as well as proposals for solutions are discussed.

The thesis is concluded with a summary and ends with an outlook and suggestions for further developments based on the results of the presented work.

2 Background

This chapter deals with the theoretical background necessary to understand the generation process of the CARS signal when applying broadband pulses. Because the development of sophisticated methods throughout this thesis is mainly based on the control over the spectral phase, the working principle, experimental setup of the pulse shaper and or course the effect on the CARS signal in particular are discussed as well. Since the vast amount of different approaches, developed methods and performed measurements cannot even be remotely covered, the reader is advised to follow important reviews and key publications covering the CARS process [30, 32–34] and pulse shaping [35–41].

2.1 Coherent Anti-Stokes Raman Scattering

Coherent anti-Stokes Raman scattering (CARS) microscopy [29] has become a widely used technique during the last 15 years. In the CARS process, usually two narrowband lasers are tuned in frequency to obtain a spectrum or set to a specific Raman transition for microscopy applications. Interaction of the probe with the induced coherence generates signal at $\omega_{CARS} = (\omega_P - \omega_{St}) + \omega_{Pr}$ that is resonantly enhanced whenever the difference frequency of pump and Stokes matches the vibrational frequency of a molecule (fig. 2.2, details in section 2.1.2). As a third-order process, CARS shows intrinsic 3D sectioning capability while the superposition of coherently generated signal assures high sensitivity. CARS spectroscopy was originally invented and explored for the investigation of flames and combustion processes [42, 43]. It has evolved into a powerful technique with application in many fields and has been developed in particular for microscopy [29]. Signal levels orders of magnitude higher than in spontaneous Raman spectroscopy enable video-rate detection, which can even be applied for live cell imaging circumventing the need for staining [15]. These ad-

vantages led to many applications, especially in life-sciences for biomedical imaging [44–47] but also for monitoring artificially engineered materials [48–50].

2.1.1 The Molecular Susceptibility

The generation of different nonlinear signals by the interaction of electric fields with the sample is described by the nonlinear polarization, which was given in a general form in eq. (1.1). The nonlinear susceptibilities $\chi^{(n)}$ are molecule specific properties that contain all information about resonant and nonresonant vibrational contributions. It is the aim of any vibrational spectroscopic technique to somehow gain access to this information. The molecular response highly depends on the orientation of the vibrational motion with respect to the incoming polarization of light [a]. Often, the interaction of light and matter is strongest when the polarization is parallel to the vibration. To describe all possible orientations of n interacting light fields as well as the orientation of the generated signal, $\chi^{(n)}$ has to be a tensor of the rank *n+1*.

2nd-order Susceptibility

Starting from eq. (1.1), a more detailed view describes the SFG signal generated along one axis i, which is given by

$$P_i^{(2)}(\omega_m + \omega_n) = \sum_{jk} \sum_{(mn)} \chi_{ijk}^{(2)} \, E_j(\omega_m) \, E_k(\omega_n). \tag{2.1}$$

The indices i, j, k define the polarizations of the generated signal and the two incoming fields with respect to the molecular symmetry. Due to symmetry properties of the molecule the number of independent tensor elements is usually drastically reduced [51]. The combination of the right choice of the incoming polarizations and a polarizer in front of the detector allows to probe specific tensor elements as shown in eq. 2.2. In this example only two independent tensor elements exist that require a specific polarization geometry to generate signal but on the other hand also allow to

[a] The term 'polarization' used here describes the orientation of the incoming electric field, i.e., in which plane the field is oscillating with respect to the geometry of the molecule or the laboratory frame and must not be confused with the induced polarization of a molecule by interaction with the electric fields.

distinguish these elements.

$$P^{(2)} = \underbrace{\chi^{(2)}_{xxy} E_x(\omega_m)\, E_y(\omega_n)}_{x-polarized} + \underbrace{\chi^{(2)}_{yyy} E_y(\omega_m)\, E_y(\omega_n)}_{y-polarized} \tag{2.2}$$

This fact was particularly often applied for studying collagen orientation for a possible early diagnosis of diseases of skin tissue.

3rd-order Susceptibility

Similarly, the CARS signal as a 3rd-order process is described by

$$P^{(3)}_i(\omega_{CARS}) \propto \sum_{jkl} \chi^{(3)}_{ijkl}(-\omega_{CARS}; \omega_1, -\omega_2, \omega_3)\; E_j(\omega_1)\, E^*_k(\omega_2)\, E_l(\omega_3). \tag{2.3}$$

As before, the indices of $\chi^{(3)}_{ijkl}$ refer to the cartesian polarization components x, y, z of the CARS signal (i), the pump (j), the Stokes (k) and the probe (l). For solids with low symmetry, $\chi^{(3)}$ can contain up to 81 independent non-zero elements. For isotropic media (e.g. gases and liquids) many elements are zero and all other components can be derived from only three independent ones [51, 52]. Also, the polarization of the beams in the z-direction usually is zero, so that all elements with a z-component for j, k or l are not contributing to the signal. However, non-zero off-diagonal elements enable the coupling of polarizations to give signal at a different polarization. For example, if $\chi^{(3)}_{xyyy} \neq 0$, a x-polarized signal is generated although the excitation fields are all polarized along the the y-axis.

As has been discussed in chapter 1, the difference frequency of the pump and Stokes fields drives the motion of the electron cloud. By coupling with the vibrational motion, the CARS-signal is resonantly enhanced when the difference matches a Raman frequency. Nonetheless, the electronic motion itself also generates a frequency-independent signal without interacting with a resonant level. This electronic signal is the origin of the frequently discussed instantaneous nonresonant background inherent to the CARS signal. The complete 3rd-order susceptibility is therefore described by a frequency-independent nonresonant part and the sum of resonant contributions of all Raman modes in eq. (2.4). Due to a different dependence on the incoming polarizations, linearly polarized resonant and nonresonant signals are generated under a

different angle, allowing to suppress the nonresonant part under certain experimental conditions [52–56]. However, if one is not interested in polarization background suppression or the individual contribution of susceptibility components to the signal, the polarization dependence can be (and usually is) neglected. If not carefully choosing the input polarizations and not resolving the signal polarization, the rather complicated descriptions can be simplified. The expression then solely considers the spectral dependence of the susceptibility, i.e., the resonance enhancement at the Raman frequencies $\Omega = \omega_p - \omega_{St}$. The susceptibility is described by the expression

$$\chi^{(3)}(\Omega) = \chi^{(3)}_{nr} + \sum_i \chi^{(3)}_{i,res}. \tag{2.4}$$

Note that the resonant part actually consists of the contributions from all Raman modes. The complete susceptibility is described by [30, 57] (see also fig. 2.3)

$$\chi^{(3)}(\Omega) = \chi^{(3)}_{nr} + \sum_k \frac{A_k}{\Omega_k - \Omega - i\,\frac{\Gamma_k}{2}}. \tag{2.5}$$

A_k are the amplitudes of the Raman frequencies Ω_k. Ω is the difference frequency of the pump and Stokes fields and Γ_k the full-width at half maximum (FWHM) of the corresponding Raman line. As in spontaneous Raman spectroscopy, the macroscopic susceptibility is proportional to the number of scattering molecules on the microscopic level [b]. But on the contrary, in CARS spectroscopy the signal is coherently added up to yield a signal $S = |\sum E_{CARS}|^2$ (also see explanation in *coherent signal generation*, section 1.2). The signal thus is quadratically dependent on the concentration of scattering molecules. The coherent nature of the CARS signal furthermore leads to the fact that, the nonresonant background does not just pose an offset but actually leads to a distortion of the lineshape by interference with the resonant contributions, shown in fig. 2.1c and described by eq. (2.6). This often limits image contrast and spectral resolution.

$$S_{CARS} \propto |\chi^{(3)}_{nr}|^2 + |\chi^{(3)}_{res}|^2 + 2\chi^{(3)}_{nr} Re\{\chi_{res}\} \tag{2.6}$$

Several methods have been developed to minimize these effects by sophisticated exci-

[b] Sometimes this fact is expressed by a molecular susceptibility $\beta^{(3)}_{ijkl}$: $\chi^{(3)}_{ijkl} = N \cdot \beta^{(3)}_{ijkl}$

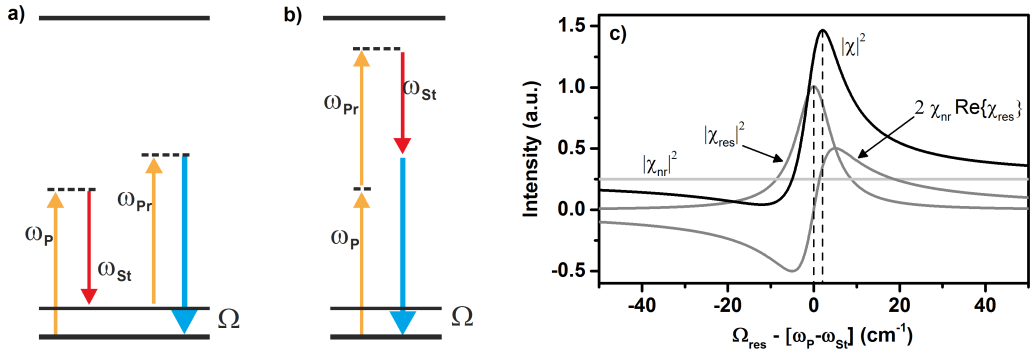

Figure 2.1: Influence of the third-order susceptibility on the CARS signal. a) Resonant CARS process where the pump/Stokes difference frequency coincides with a vibrational resonance at $\Omega = \omega_p - \omega_{St}$. b) One way to illustrate the nonresonant contribution to the CARS signal as described by $\chi^{(3)}_{nr}$. Signal at the same frequency as in a) is generated without interacting with a resonant level. If the interactions are close to a electronic resonant level (solid top line), the vibrationally nonresonant signal can be enhanced by an electronic resonance (not shown). c) Representation of the components of the squared modulus of the third-order susceptibility contributing to the CARS signal. While the resonant part follows the typical Raman lineshape, interference with the nonresonant offset signal leads to the interference term $2\chi_{nr}Re\{\chi_{res}\}$. This leads to the typical dispersive lineshape and thus also to a frequency-shifted CARS signal.

tation and detection schemes. As already discussed, different polarization dependence of resonant and nonresonant responses [55, 56], but also epi-detection [58] or time-delayed probing [59–61] allow to get rid of nonresonant contributions. The latter makes use of the fact that the electronic nonresonant signal vanishes almost instantaneously while the coherence of a vibrational level lasts much longer. Additionally, in heterodyne detection the phase difference between a local oscillator and the excitation spectrum is utilized to control the signal [62]. It allows to perform quantitative measurements because the signal becomes linearly dependent on the concentration of scatterers. By exploiting the flexibility of a pulse shaper, all of the mentioned methods and even combinations thereof can be implemented in single-beam CARS (SB-CARS), making it a versatile approach for spectroscopy and imaging [63–67] as shown in the following.

2.1.2 From Picosecond to Femtosecond CARS

CARS measurements are usually performed using two synchronized ps lasers, which deliver the pump/probe and the Stokes frequencies. As can be seen in fig. 2.2a, their difference frequency is tuned to a Raman level to induce a coherence and to generate the blue-shifted CARS-signal by interaction with the probe. The high peak intensity of 2-8 ps lasers at bandwidths in the range of typical Raman linewidths ($\sim$ 2-10 cm^{-1}) assures high signal intensities and high spectral resolution. On the downside, only one resonance can be measured at a time. In order to record a whole spectrum or to obtain contrast from two different Raman levels, tuning of at least one of the laser frequencies is necessary (fig. 2.2a bottom).

Besides the ps-CARS approach, other sophisticated methods have been developed. In multiplex CARS (M-CARS) entire vibrational spectra are obtained without the need for tuning the laser frequencies [68]. The combination of a narrowband pump/probe (ps-range) and a broadband Stokes pulse (fs-range) allows to excite all modes within the width of the laser spectrum (i.e., the width of pump/Stokes difference frequencies), shown as gray part in fig. 2.2b. In principle, either pump or Stokes or even both can be broadband - although the latter would lead to an increase in the nonresonant signal. As long as the probing is narrowband, all excited frequencies are definitely mapped and visible as a CARS spectrum. Data analysis methods like the maximum entropy method (MEM) [69] then allow to obtain a Raman-like spectrum.

This concept can be taken even further by using only one broadband 10-fs laser source. In this single-beam approach, all frequencies taking part in the CARS process are already contained within the broadband laser spectrum. The vast number of possible pump-Stokes combinations leads to a simultaneous excitation of all vibrations that lie within the range of the spectrum [40, 70]. On the downside, the broadband probing results in overlapping signals from different Raman lines. This is indicated by the red arrows in fig. 2.2c. Additionally, the number of interactions that do not coincide with a Raman level is drastically increased, which leads to a huge nonresonant background. In the end, a very strong but unspecific and washed-out signal is obtained if no measures are taken. However, by controlling the spectral phase with a pulse shaper, it is possible to minimize or even suppress the nonresonant background and retrieve the molecular information [40, 63, 64, 71, 72].

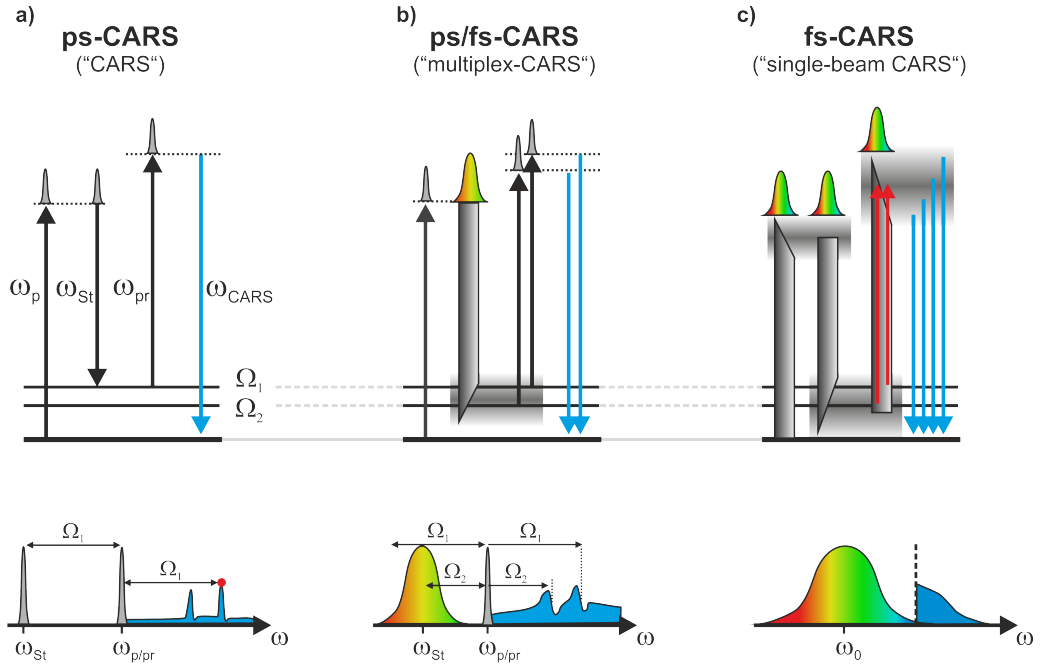

Figure 2.2: Comparison of different CARS schemes. a) depicts typical narrowband CARS measurements performed with picosecond lasers. The laser frequencies are tuned to match a certain Raman level Ω_1. Signal only from this level (red spot in the spectrum below) is generated with little nonresonant background. To measure several levels or a whole CARS spectrum, subsequent frequency tuning is necessary. In b) the multiplex-CARS approach is shown, where a broadband Stokes pulse leads to the simultaneous excitation of all levels within the width of the pump/Stokes interaction. The influence of nonresonant contributions is increased but on the other hand, a whole CARS spectrum can be recorded in one shot. The single-beam CARS approach is depicted in c). All pump, Stokes and probe frequencies are already contained within the width of a broadband 10 fs laser. Although all levels within the pump/Stoles interaction width are excited, a huge nonresonant background is generated due to the vast number of possible nonresonant interactions. Also as highlighted by the red arrows, the many possible probe frequencies lead to spectrally overlapping signal from different Raman levels. In the end, a strong but nonspecific signal is generated, making phase shaping strategies necessary to regain vibrationally resonant information (see chapter 3). Note that the actual CARS signal is in all cases many orders of magnitude weaker than the laser intensity.

2.2 Single-Beam CARS

2.2.1 Description of Femtosecond Pulses

Femtosecond pulses are bursts of light, usually generated by titanium-sapphire lasers with durations down to 5 fs and repetition rates from kHz up to hundreds of MHz. The pulses can be equally well described in the time or the frequency domain, which are connected by the Fourier relations (eq. (2.8) & (2.11)). This implies that an ultrashort pulse requires an ultrabroad spectrum, or in other words, temporal and spectral width cannot be infinitely narrow at the same time. The time-bandwidth product of the full-width at half maximum (FWHM) of the temporal τ and spectral $\Delta\omega$ width fulfills the equation

$$\tau \cdot \Delta\omega \geq 2\pi \cdot c_B. \tag{2.7}$$

The value of the constant c_B depends on the pulse profile and is, e.g. $c_B = 0.44$ for Gaussian pulses. In any case, the shortest possible pulse duration is obtained when the relative phases of all frequencies equals zero, referred to as Fourier transform-limit (TL or FTL).

In the field of femtosecond pulse shaping with a liquid crystal mask (sec. 2.3), effects are commonly explained in the frequency domain because one has direct access to the phase of the spatially dispersed frequencies. Nonetheless, the time domain picture can be of great value too and allows a deeper understanding of certain effects. Especially for the spectral focusing method developed throughout this thesis, a combination of both domains provides an intuitive picture and is of utmost importance for understanding the technique. In the frequency domain, the electric field can be described by a slowly varying field envelope $|E(\omega)|$ and a frequency dependent phase term $\phi(\omega)$

$$E(\omega) = |E(\omega)| \ \exp\left(i\phi(\omega)\right) = \mathcal{F}^{-1}\{E(t)\}. \tag{2.8}$$

In order to understand the effect of the spectral phase on the temporal profile, it is common and most comprehensible to expand the spectral phase in a Taylor series

around the center frequency ω_0 of the laser [73].

$$\phi(\omega) = \phi(\omega_0) + \frac{\partial\phi(\omega)}{\partial\omega}\bigg|_{\omega_0} \cdot (\omega - \omega_0) + \frac{1}{2}\frac{\partial^2\phi(\omega)}{\partial\omega^2}\bigg|_{\omega_0} \cdot (\omega - \omega_0)^2 + \dots \tag{2.9}$$

$$= \phi_0 + \phi_1 \cdot (\omega - \omega_0) + \tfrac{1}{2}\phi_2 \cdot (\omega - \omega_0)^2 + \dots \tag{2.10}$$

As a phase offset, the first term has no effect on the temporal shape of the pulse while the second (linear) expansion coefficient ϕ_1 only leads to a shift of the pulse envelope in time, also called group delay. The third (quadratic) term ϕ_2 results in a linear sweep of the frequencies in time and is referred to as linear chirp. As the second derivative it describes the dispersion of the group delay (often termed group delay dispersion, GDD) and can be understood as the arrival time of the different instantaneous frequencies with the constant offset of the group delay ϕ_1.

In the time-domain, the complex electric field of ultrashort pulses can be similarly described by a temporal field envelope $|E(t)|$ and a phase term φ_{inst}. Expressing the instantaneous phase in the form of a carrier frequency ω_0 and a time dependent phase $\varphi(t)$ yields

$$E(t) = |E(t)| \ \exp^{i\overbrace{(\omega_0 t - \varphi(t))}^{\varphi_{inst}(t)}} = \mathcal{F}\{E(\omega)\}. \tag{2.11}$$

By analogy with eq. (2.10), the temporal phase $\varphi(t)$ is expanded around the arrival time of a laser pulse.

$$\varphi(t) = \varphi_0 + \varphi_1 \cdot (t - t_0) + \tfrac{1}{2}\varphi_2 \cdot (t - t_0)^2 + \dots \tag{2.12}$$

The term φ_2 again describes the linear chirp, which corresponds to a linear distribution of the instantaneous frequencies in time. Increasing (decreasing) frequencies with time are referred to as positive or up-chirp (negative or down-chirp). The instantaneous frequency, i.e. the frequency component at one moment in time, is given by the derivative of the instantaneous temporal phase (eq. (2.11)) as

$$\omega_{inst}(t) = \omega_0 - \frac{\partial\varphi(t)}{\partial t}. \tag{2.13}$$

2.2.2 Theory & Simulation

To gain a deeper understanding of the single-beam CARS process, understanding the interaction of the frequencies of the broadband spectrum with the molecule is required. As reflected also by the formulations describing the CARS process in the following, it is best to separate the equations into the excitation probability A(Ω) (eq. (2.15)), the molecular properties and the probing process. The Raman excitation probability A(Ω) describes the ability of the laser field to excite a certain Raman level and is given by the integral over all possible pump-Stokes frequency pairs at the difference frequency Ω. It is maximized when the phase difference of pump and Stokes frequencies $\Delta\phi$ is zero, as it is fulfilled throughout the whole spectrum in the case of a transform-limited pulse. By controlling this phase difference $\Delta\phi = \phi_P(\omega') - \phi_{St}(\omega' - \Omega)$, the excitation probability and therefore the subsequently generated CARS signal can be controlled [40, 63, 64, 70–72]. The total signal field can be calculated with eq. (2.14), where $E(\omega)$ (eq. (2.8)) is the spectral complex amplitude [41].

$$E_{CARS}(\omega) = \int_0^\infty \mathrm{d}\Omega\, E_{Pr}(\omega - \Omega)\, \underbrace{\chi^{(3)}(\Omega)\, A(\Omega)}_{R(\Omega)} \tag{2.14}$$

$$A(\Omega) = \int_0^\infty \mathrm{d}\omega'\, |E_P(\omega')\, E^*_{St}(\omega' - \Omega)|\, e^{i\Delta\phi} \tag{2.15}$$

$$\chi^{(3)}(\Omega) = \chi_{nr} + \sum \frac{A_{Raman}}{\Omega - \Omega_{res} - i\Gamma} \tag{2.16}$$

$$E_{CARS}(\omega) = 4\pi^2 \mathcal{F}\left(\mathcal{F}^{-1}\{\chi^{(3)}(\Omega)\}\ \ \mathcal{F}[\,|\mathcal{F}^{-1}\{E(\omega)\}|^2]\ \ \mathcal{F}^{-1}\{E(\omega)\}\right) \tag{2.17}$$

As shown in section 2.1.1, the third-order susceptibility $\chi^{(3)}(\Omega)$ contains the molecular information, consisting of a frequency independent nonresonant part and the actual molecular vibrations. The response R(Ω) of the molecule to the excitational field depends on its resonances and is obtained by weighting the excitation probability with the susceptibility (eq. (2.16)). Formulation of eq. (2.14) in terms of Fourier transformations (eq. (2.17)) speeds up the calculation of the CARS signal field by orders of magnitude because the time-consuming evaluation of integrals is circumvented and replaced by simple multiplications of Fourier transformations [74, 75]. For exact simulations of SB-CARS data, the experimental parameters must be

used for the calculations. To do so, the amplitude of the excitation field $E(\omega)$ is obtained by a measurement of the laser spectrum and its phase is defined by the phase parameters applied with the pulse shaper. Thus, in order to be able to apply correct phase functions in the experiment, it is crucial to correct for phase distortions from the setup and start with a flat phase (i.e. a transform-limited pulse at the sample position). The molecular susceptibility $\chi^{(3)}(\Omega)$ can be obtained by measurement or fitting CARS data [76–78].

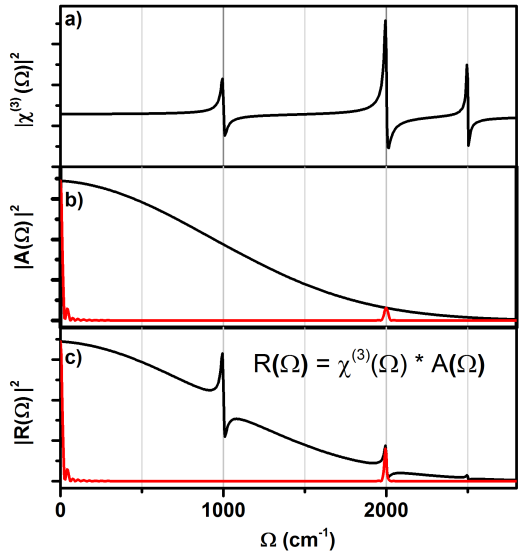

Figure 2.3: a) The third-order susceptibility contains a nonresonant electronic contribution (offset) and the vibrational resonances of the molecule. It is calculated from eq. (2.16) with linewidths Γ of 15 cm^{-1} at 1000 cm^{-1}, 2000 cm^{-1} and 2500 cm^{-1}. b) The excitation probability can be influenced by special phase shaping techniques (red) to be nonzero only at the chosen resonance Ω, while the transform-limited pulse (black) is nonspecific throughout the spectrum. The molecular response in c) shows that this only leads to the excitation of one specific molecular resonance. In the case of a transform-limited pulse, not only are all resonances excited simultaneously but so are all virtual levels within the width of the spectrum. This leads to an overwhelming nonresonant background.

Simulations based on the expressions discussed above are illustrated in fig. 2.3. In fig. 2.3a, an exemplary susceptibility with three resonances Ω_{res}, linewidths Γ and amplitudes A_{Raman} is shown as calculated from eq. (2.16). The black curves in fig. 2.3b & c illustrate the excitation probability and the molecular response when working with transform-limited pulses. To excite high-energy levels, pump and Stokes

frequencies from the blue and red wing of the spectrum are interacting. Because the number of possible pairs and the overall intensity of the spectrum is decreasing when approaching the wings, the excitation probability is continuously decreasing, too. The effect of the unspecific excitation with TL-pulses is also imparted on the molecular response R(Ω). Not only all vibrations within the spectral width get excited but the nonresonant contributions of the molecule (offset of the susceptibility in fig. 2.3a) will lead to strong nonresonant signal throughout the spectrum. The red curves in fig. 2.3b & c give a first example of how phase shaping of a broadband pulse can be used to control the excitation probability. The phases of pump and Stokes frequencies are chosen in a way that constructive interference only takes place at a resonance around $2000\,\mathrm{cm}^{-1}$. As a result, the excitation probability is minimized everywhere except at the chosen point, which is also reflected in the molecular response (red curve in fig. 2.3c). Contributions from outside the narrow specified area, regardless if of resonant or nonresonant nature, are suppressed. After interaction with the probe frequencies, only the selected signal will be generated. A more detailed discussion of how phase shaping can be used to retrieve molecular information with broadband pulses will be given in chapter 3.

2.3 Pulse Shaping

2.3.1 Experimental Setup

A detailed scheme of the optical setup is presented in fig. 2.4. The light source is a high-power Ti:Sa oscillator (Femtolasers Fusion Pro 800, mean power: 800 mW, repetition rate 76 MHz) delivering pulses with durations <10 fs centered around 800 nm. A set of chirped mirrors pre-compensates a large part of the second-order dispersion mainly introduced by the microscope objective (details in appedix B). The light is diffracted by a gold-coated blazed grating with 600 lines/mm. Littrow configuration (i.e. incoming and outgoing angles are identical) assures the highest efficiency for the reflected first-order. The grating is slightly tilted downwards to hit a cylindrical mirror placed exactly at the focal length $f = 35$ cm to collimate the diffracted light. The cylindrical mirror is slightly tilted upwards, so that the rays are in parallel to the table when they hit the folding mirror and go through the spatial light modulator

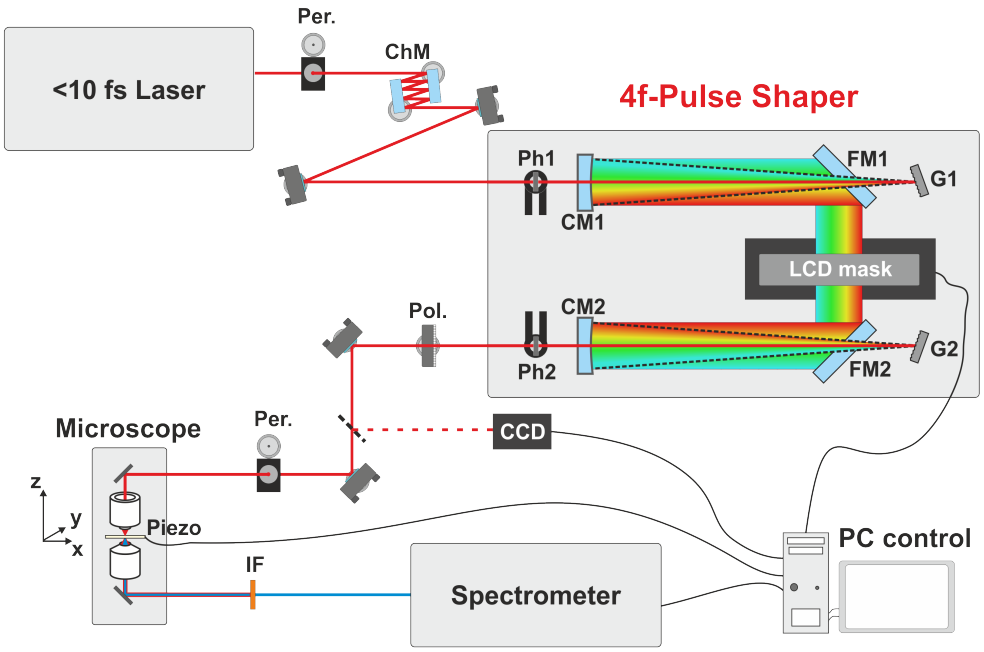

Figure 2.4: Detailed experimental setup for single-beam nonlinear microscopy. Per, periscope; ChM, negatively chirped mirrors; Ph, pinholes; CM, cylindrical mirror with $f = 35$ cm; FM, planar folding mirrors; G, gold-coated reflective gratings with 600 lines/mm; Pol., broadband polarizer; IF, interference short-pass filter $\lambda < 650$ nm.

(Jenoptik SLM 640d), which consists of two liquid crystal masks. The SLM is placed at the Fourier plane, i.e., at a distance of $2f$ from the grating. The mirrored setup of the second half of the shaper recombines all frequencies so that the total length of the beam path is 4f. With the help of a small CCD camera and two pinholes in front of and after the shaper, the laser can be perfectly coupled into the shaper on an every day basis. The whole 4f-setup performs an optical Fourier transformation from the time to the frequency domain (and back) and thereby enables shaping ultrashort femtosecond pulses. A polarizer transmits only components along its axis and thereby transforms the polarization shaping of the LCD mask into an amplitude pattern (amplitude shaping, i.e. changing the light intensity at each pixel) before it is coupled into the microscope (Olympus BX 51) equipped with a 0.7 NA, 60x microscope objective and a 0.6 NA, 40x collimation objective (both Olympus LUCPlan FL N). Samples are fixed on a XYZ piezo stage (PINano, range 200 µm in x, y and z). In

this setup, not only CARS but also nonlinearly generated signals can be detected simultaneously in a broad spectral region from 350 nm to 700 nm. Signal detection can be done either with an intensified CCD camera (Andor ICCD) or a combination of photomultipliers and several optical filters (not shown). In both cases the excitation laser light is blocked using an interference filter (Semrock, shortpass λ<650 nm or λ<700 nm). The CCD camera is combined with a monochromator (Acton Research, 300i) for spectrally resolved acquisition with typical pixel dwell times of 10 ms. It is well suited for comparing signal intensities and identifying overlapping spectral regions. For fast imaging the single-channel detection is used. The signals are separated with long-, short- and band-pass filters, depending on the measured sample. Data acquisition 100 times faster than in the spectrally resolved case is achieved and is therefore better suited for imaging due to the increased speed and reduced photo damage [79]. Typical images (200 µm×200 µm)are obtained in 60 s to 120 s.

2.3.2 Working Principle of the Liquid Crystal Mask

Once the spectrum is horizontally dispersed over the LCD-mask, the polarization and relative phase of the individual frequencies can be controlled with every of the 640 pixels separately. The operation of the whole mask can be understood as modulating an input electric field $E_{in}(\omega)$ with a mask function $M(\omega)$ composed of an amplitude A= $|M(\omega)|$ and phase part ϕ, as imprinted on the spectrum with the shaper.

$$E_{out}(\omega) = M(\omega) \cdot E_{in}(\omega) = |M(\omega)|\, e^{i\phi(\omega)} \cdot E_{in}(\omega) \tag{2.18}$$

As eq. (2.18) suggests, by choosing the right mask functions, amplitude (or polarization if no polarizer is introduced after the shaper) and phase of the spectrum can be controlled (see also eq. (2.19)).

The actual working principle is illustrated in fig. 2.5. The SLM consists of two masks, each having 640 pixels containing birefringent liquid crystals. The optical axis of the crystals in the first cells is oriented at +45° and the second at -45° with respect to the linearly polarized incoming light. Light incident on the first cell therefore is equally split along the ordinary (o) and extraordinary (eo, parallel to the optical axis of the crystals) axes. In the second pixel, the extraordinary (ordinary) wave from the first one travels along the ordinary (extraordinary) axis. It is thereby possible

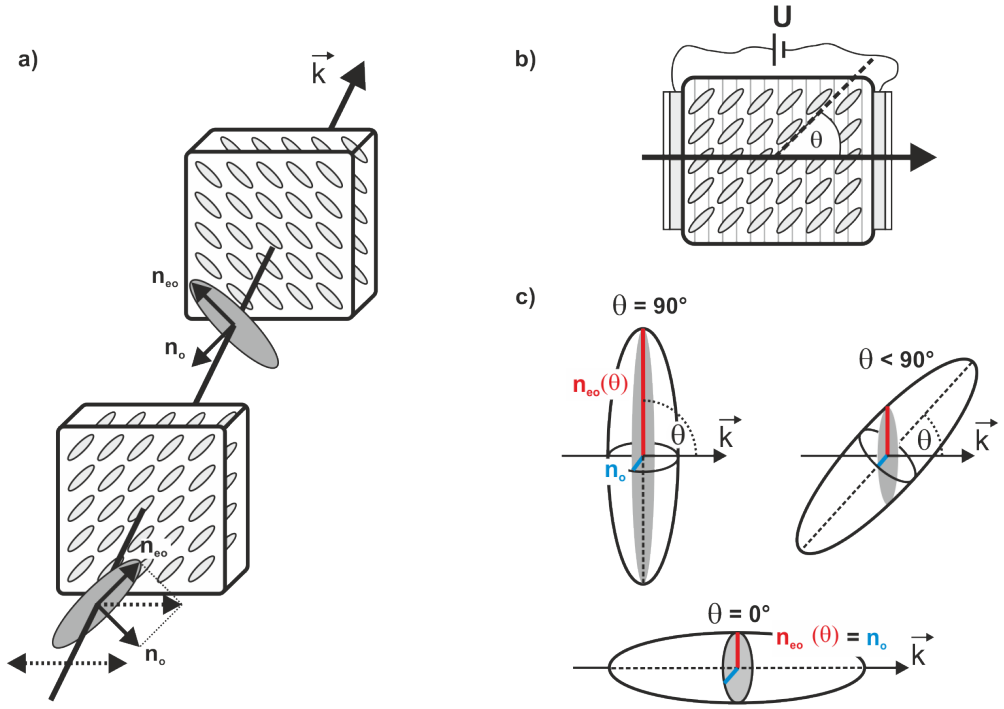

Figure 2.5: Working principle of the double liquid (LC) crystal mask. a) The crystals are oriented at ±45 deg with respect to the horizontal input polarization. Light is split 50:50 along the ordinary (o) and extraordinary (eo) axes. Light traveling along the o-axis in the first cell, will travel along the eo-axis in the second cell and vice versa. The phase difference of the o & eo waves can be controlled by a voltage as shown in a side-view of a cell in b). While n_o is constant, the eo-refractive index depends on the angle θ between the incoming light and the crystals' optical axis. c) shows the angle dependence of n_{eo}, which is exploited to control the phase and polarization at each LC-cell separately.

to independently control the phase and polarization. Because the ordinary refractive index n_o is constant while the eo-refractive index $n_{eo}(\theta)$ depends on the angle between propagation of the light and the optical axis of the crystal (fig. 2.5b & c), controlling this angle means controlling the phase difference between the two axes. As illustrated in a side view of one cell in fig. 2.5b, this angle can be controlled independently for each pixel by applying a voltage. Fig. 2.5c shows three different orientations of the crystals with respect to the incoming light. Note that n_o is constant while the highest phase difference is achieved for $\theta = 90°$.

The phase change of the first and the second liquid crystal cell ($\Delta\phi_1$ & $\Delta\phi_2$)

combined determine the effect on the spectral phase and amplitude (or polarization) modulation. In the experiment, first an amplitude A and spectral phase function ϕ that describe the desired output are defined by the user. These functions are then recalculated to be applied with the two masks to achieve the desired control. The calculation can be done following eqs. (2.19) & (2.20) [80].

$$E_{out} = \underbrace{\begin{bmatrix} 1 \\ 0 \end{bmatrix}}_{Pol.} \underbrace{\cos\Big(\frac{\Delta\phi_1 - \Delta\phi_2}{2}\Big)}_{A} \exp\Big[i\Big(\underbrace{\frac{\Delta\phi_1 + \Delta\phi_2}{2}}_{\phi}\Big)\Big] \cdot E_{in} \tag{2.19}$$

$$\text{with} \quad \Delta\phi_1 = \phi + \arccos(A) \qquad \Delta\phi_2 = \phi - \arccos(A) \tag{2.20}$$

2.3.3 Implementing Complex Phase Functions

While understanding the amplitude functions is straightforward, defining the right spectral phase functions requires a more detailed look. For simple amplitude shaping, it follows from eq. (2.19) that the light is blocked by the polarizer for $A = 0$ (rotation to vertical linearly polarized light) and transmitted for $A = 1$ (polarization state unchanged, i.e. linear horizontal polarization). Values in between therefore lead to elliptically polarized light, which results in attenuated intensity after passing the polarizer.

Constructing complex phase functions is based on the Taylor expansion of the spectral phase $\phi(\omega)$ from eq. (2.10). Therein, the temporal distribution of each frequency component is described by a set of expansion coefficients. Different effects for separated frequency regions of the broadband spectrum can thus be described individually, as shown in fig. 2.6. In fig. 2.6, the spectrum is divided into three independent regions. A phase function, e.g. a delay or chirp, can be chosen and is calculated by following eq. (2.10). The effect of a positive chirp of $4000\,\mathrm{fs}^2$ in the blue wing around its center frequency ω_0^a is shown in the time-frequency map. For the central region, a delay of 200 fs and and for the red part of the spectrum, a negative chirp of $-3000\,\mathrm{fs}^2$ is defined with respect to their central frequencies ω_0^b and ω_0^c. Piecing together several simple functions from the frequency regions in relation to a common t_0 thereby allows to implement complex temporal distributions in a very intuitive way. Hence, by using the pulse shaper in the single-beam CARS approach

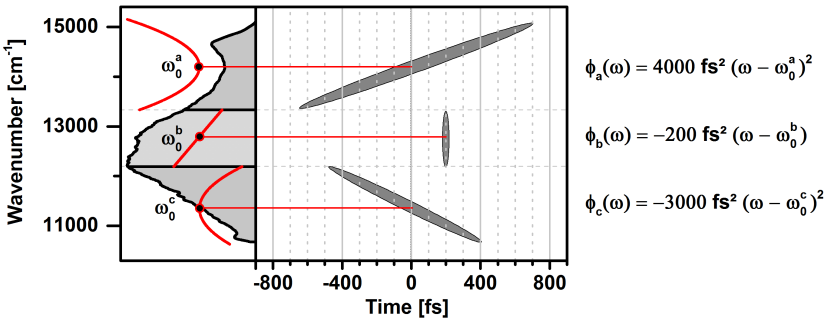

Figure 2.6: Definition of complex phase functions. The spectrum is divided into several frequency regions. Simple functions can be calculated individually for each region and then pieced together in relation to a common t_0 in order to achieve a rather complicated scheme shown in the time-frequency map. The applied phase functions of each region calculated from eq. (2.10) is shown on the right side.

it is straightforward to construct phase functions that lead to different chirp, delay or combinations of both, e.g., for pump, Stokes and probe if they are spectrally separated. This approach was used throughout this thesis and is evident from all time-frequency maps in the following chapters (e.g. in fig. 3.10).

2.3.4 Limitations

So far the descriptions assumed a perfect reproduction of the calculated phase with the pulse shaper. In the experiment, however, several factors limit the performance. While some limitations can be minimized by careful optimization, others are intrinsic to phase shaping and cannot be influenced.

The most obvious limitation arises from the fact that the liquid crystal mask consists of several hundred pixels, each of which can be addressed individually. For the shaper used throughout this thesis, between each pixel of 97 µm there is a gap of 3 µm. Light passing through the gaps cannot be influenced and leads to pulse replicas. Pixilation also implies that every smooth phase function will be represented in the experiment by a limited number of pixels. The Nyquist sampling theorem states that the phase difference between two adjacent pixels must not exceed π in order to be perfectly reproduced without loss of information. The slope of phases imprinted on the shaper is therefore limited, which in turn limits the maximum applicable time delay or chirp, as derived in detail in appendix A.

Another intrinsic effect when shaping pulses with an SLM in the symmetry plane of a 4f-setup is space-time coupling [35, 81, 82]. Space-time coupling results in a modulation of both the temporal shape of an ultrashort pulse and its transverse spatial energy distribution upon applying a phase function. In the simplest case of a time delay (linear phase function), the laser beam is linearly displaced in space, too (see appendix C). In microscopy applications, an increasing part of the collimated laser beam will be blocked by the aperture of the focusing objective at high time delays. Consequently, the intensity transmitted to the focus is decreasing, which poses serious problems when comparing measurements at different time delays. In section 3.4.4 it will be shown how shaping itself can be used to measure and correct for the decreasing laser intensity in the focus - and thereby account for the decreasing signals.

3 Spectral Focusing CARS

3.1 Introduction

Spectral Focusing is a versatile technique for CARS microspectroscopy, which overcomes the poor spectral resolution of femtosecond pulses and enables spectroscopy as well as imaging with high spectral resolution. The basic idea is to stretch the pump and Stokes frequencies of the corresponding broadband pulses in time to generate a constant frequency difference. Strong signal will only be generated due to resonant enhancement when this difference coincides with a vibrational level. The possibility to easily change the frequency difference enables to collect vibrational CARS spectra. By focusing on a single resonance, an elegant and flexible approach for microscopy applications is readily available. In this chapter it will not only be shown how spectral focusing can be adapted for the single-beam setup, but how pulse shaping enables a considerable signal increase and even the development of new modalities and contrast mechanisms. Furthermore, it is the basis for the controlled generation of a tunable light source in the mid-IR region presented in chapter 4.

The contrast in CARS imaging is often limited by an inherent nonresonant contribution, which interferes with the resonant signal (see eqs. (2.4)). It arises from instantaneous electronic four-wave mixing responses generating signal even far away from resonant vibrational levels. As explained in fig. 2.2, the nonresonant contributions become more dominant with increasing spectral width. Hence, especially in the case of ultrabroadband femtosecond pulses special methods are required to extract the resonant vibrational information.

In order to get the optimal ratio of image contrast and signal, it is beneficial to use laser bandwidths that lie in the range of typical Raman linewidths (5 - 100 cm^{-1}) [30, 31]. While excitation with picosecond pulses matches linewidths in the fingerprint

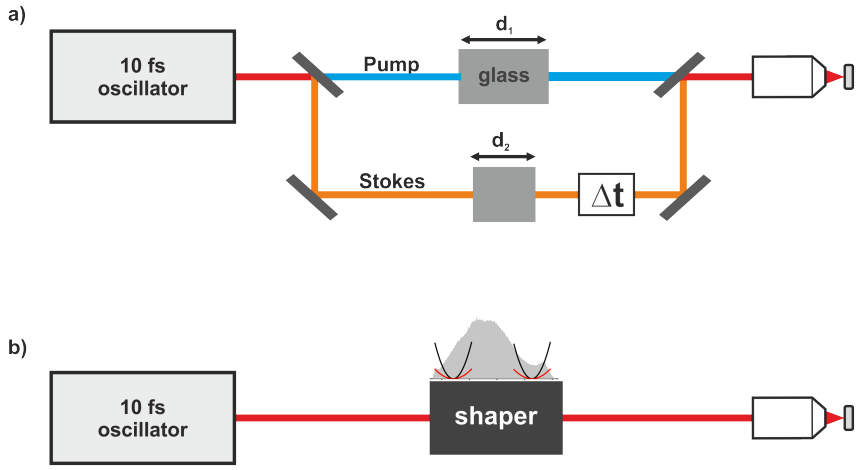

Figure 3.1: Comparison of a traditional and a shaper based spectral focusing approach. a) In the traditional approach, spatially separated pump and Stokes beams are stretched in time by glass blocks of different length and the difference frequency is adjusted by a delay stage. b) In the shaper-based approach, the experiment is highly simplified. Beam splitting, static dispersive elements or delay stages are replaced by the shaper, where all important parameters of the beam are controlled by applying tailored spectral phase functions with high speed and flexibility.

region (5 - 20 cm^{-1}), the optimal excitation of C–H-stretching vibrations requires shorter pulses (linewidth for lipids $\sim 100\,\mathrm{cm}^{-1}$). The advantages of narrowband (picosecond lasers) and broadband (femtosecond lasers) excitation can be exploited by combining broadband pulses with flexible shaping strategies. The quick adjustment of the instantaneous bandwidth to varying Raman linewidths allows for the suppression of the otherwise overwhelming nonresonant background and results in optimized image contrast.

One of the simplest phase control techniques can be realized by placing passive optical elements with high group velocity dispersion (GVD) into the beam path (fig. 3.1a). By equally chirping pump and Stokes beams, it is possible to adjust the instantaneous bandwidth to certain Raman linewidths and in the limiting case even mimic the picosecond CARS scheme. In this approach, referred to as spectral focusing [83–86], usually glass rods are used to equally stretch the pump/Stokes frequencies in time and generate a constant instantaneous frequency difference (IFD) that drives a single Raman coherence [31, 87]. The temporal delay between the pump and Stokes pulses selects the Raman level to be probed, while the amount of chirp can be adjusted to

match the Raman linewidth and therefore leads to higher spectral resolution. Spectral focusing is particularly useful for the identification of structures based on the vibrational information of a certain Raman level in microscopy because the whole spectral energy can be focused into one level for optimal excitation. It has been combined with several CARS variations. In a multiplex-CARS approach, the temporal overlap of a transform-limited Stokes and a highly chirped pump/probe introduces a temporal gate defining the spectral resolution [88–90]. In the following years both theoretical analysis [91] and more advanced experimental investigations have been carried out. By using glass blocks of different lengths (introducing positive linear chirp) instead of the experimentally more demanding grating compressors, experimental setups have been highly simplified [31, 87, 92]. Besides, both single-beam setups with subsequent splitting into pump and Stokes beams [92] (fig. 3.1a) as well as a Ti:Sa laser system (Stokes beam) pumping an optical parametric oscillator (pump beam) [87] have been applied. Even the suppression of the nonresonant background is possible by measuring the difference signal generated by two pump/Stokes pairs with IFDs lying nearby [93–95]. In a very complex setup simultaneous measurement of up to four Raman lines was shown [96].

A further simplification can be achieved by exploiting the flexibility and high degree of control over the spectral phase and amplitude offered by a pulse shaper in a single-beam setup [40, 63–65, 70–72, 97]. In this approach, the experimental setup is simplified tremendously. Splitting the beam in two parts, delay stages and especially the inflexible passive elements are all replaced by the pulse shaper (fig. 3.1b). Changing the linear chirp and the relative delay of pump and Stokes by imprinting a tailored phase function onto a broadband pulse are just two examples of what is possible [22, 94]. In addition, amplitude shaping allows to minimize the incident power on a sample while optimizing the excitation. The phase can be remotely changed to optimize the signal intensity and spectral resolution for different bands and linewidths throughout the spectrum within a fraction of a second. Recently, a combination of spectral focusing and time-resolved CARS was demonstrated by the use of a pulse shaper in a multi-beam setup [98].

3.2 Theoretical Background

In traditional spectral focusing the pump and Stokes pulses are equally stretched in time using dispersive elements like glass or grating compressors to achieve a constant instantaneous frequency difference (IFD) [83, 84]. Changing the beating frequency of the pump and Stokes electric fields that matches the Raman frequency is done by delaying one of the pulses. Thus, the excitation process is usually also explained in the time domain. Since pulse shaping is easiest understood in the frequency domain, it is instructive to look at the signal generation process in this domain when performing spectral focusing with a pulse shaper. Altogether, the build-up of the coherence, the role of the frequencies, as well as the effect of the phase functions are most intuitively understood by combining the time and frequency pictures in a time-frequency map. It will also be the basis for the developments presented in the following sections.

3.2.1 Time Picture

An expression of ultrashort pulses in the time domain has already been given in sec. 2.2.1 (eq. (2.11)). Therein, a linear chirp is expressed by the second term $\varphi_2 = \beta$ of a Taylor expansion of the temporal phase, $\varphi(t) = \frac{1}{2}\beta t^2$. If equal chirp is applied to the pump/Stokes pulses and the Stokes beam is additionally delayed by Δt, the electric fields are

$$E_p(t,\beta) = |E_p(t,\beta)| \exp\left(i\left[\omega_p t + \tfrac{1}{2}\beta t^2\right]\right) \tag{3.1}$$

$$E_{St}(t+\Delta t,\beta) = |E_{St}(t+\Delta t,\beta)| \exp\left(i\left[\omega_{St}(t+\Delta t) + \tfrac{1}{2}\beta(t+\Delta t)^2\right]\right). \tag{3.2}$$

The coherence of a molecule in the CARS process is then driven by the interaction of the pump and Stokes pulses $A(t) = E_p(t)\cdot E^*_{St}(t)$. When omitting constant amplitude and phase factors, the excitational field calculated from the convolution of pump and Stokes fields becomes (see appendix D)

$$A(t,\beta) \propto \exp(i[\underbrace{\omega_p - \omega_{St} - \beta\Delta t}_{\Omega_{\mathrm{IFD}}}]t). \tag{3.3}$$

If the same laser field is used fur pump and Stokes (e.g. if instead of a filter, a 50:50 beam splitter is used in the experiment in fig. 3.1), the effect of spectral focusing in the time domain becomes even clearer. The equation simplifies further to give a frequency $\Omega_{\mathrm{IFD}} = \beta\Delta t$. The instantaneous frequency difference Ω_{IFD} is constant and only depends on the relative time-delay and the amount of chirp. Because matching the chirp rate β of pump/Stokes requires a tedious and lengthy adjustment, it is usually kept constant when using static dispersive elements. The IFD can thus be controlled by changing the relative time-delay Δt of the center frequencies of pump and Stokes pulses.

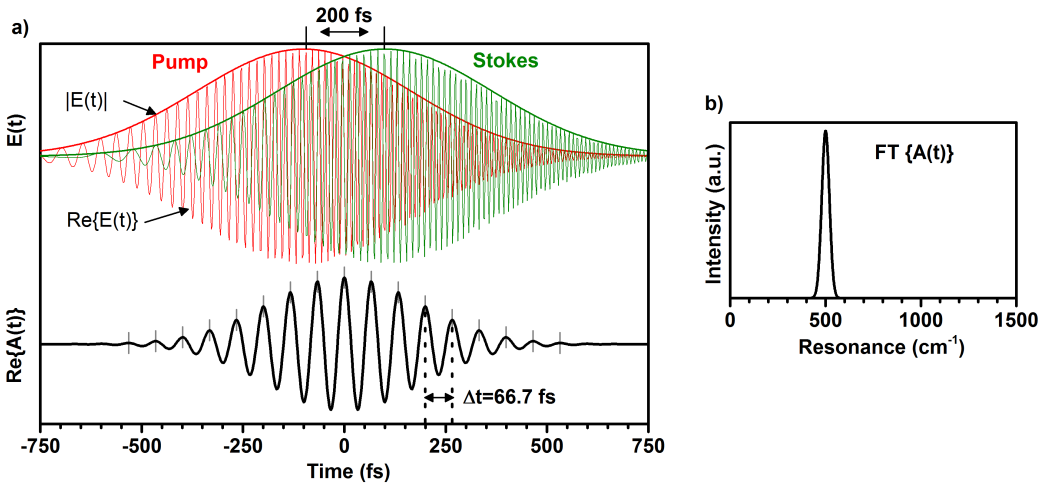

Figure 3.2: a) Equally positively chirped pump and Stokes pulses. The relative time delay of the electric fields (top) leads to a constant beating pattern (bottom). The convolution of the fields gives the excitational field A(t) with a period of 66.7 fs. b) Fourier-transformation of the excitational field reveals the addressed frequency. In the case shown, only a Raman mode at 500 cm^{-1} will be coherently driven, while other molecular vibrations do not take part in the signal generation.

Fig. 3.2a shows the interaction of the chirped pump and Stokes electric fields with a relative time delay of 200 fs. The equal linear chirp of [a] of 2121 fs^2 is reflected in the changing frequency (Re{E(t)}). The simulated excitational field A(t) shows a distinct pattern with a constant spacing of about 66.7 fs. Fourier-transforming A(t) reveals the excitational frequency driving the molecular coherence of a Raman level at 500 cm^{-1} (fig. 3.2b). As discussed above, the addressed Raman level can also be

calculated by $\Omega = \beta\Delta t$ (eq. 3.3) when the chirp and delay are known. In this case [a] $\Omega = 2.5\frac{cm^{-1}}{fs} \cdot 200\,\mathrm{fs} = 500\,\mathrm{cm}^{-1}$ (for $\omega_p = \omega_{St}$), confirming the results of the Fourier transformation.

3.2.2 Frequency Picture

With the pulse shaper in place, the application of phases and even the signal generation process are usually discussed in the frequency domain. Since the laser spectrum is spatially dispersed over the liquid crystal mask, explanations in this domain are usually more intuitive and straightforward.
From the discussion in sec. 2.2.1 it is known that spectral phase functions can be expressed as a Taylor expansion around the center frequency ω_0. A linear shift in time is achieved by a linear phase and a chirp by applying a quadratic phase function $\phi(\omega) = \frac{1}{2}\phi_2(\omega - \omega_0)^2$. In the case of single-beam spectral focusing CARS, equal chirp is applied to the pump and Stokes frequencies and the excitation probability $A(\Omega)$ of a Raman level is given by the convolution of pump and Stokes (for simplicity, eq. (2.15) is repeated here in eq. (3.4)). It can be thought of as the sum of *all* possible pathways leading to the target state Ω, i.e., all pump/Stokes frequency pairs with an energy difference matching the level Ω. The coherent interaction of the different pathways depends on their relative phase difference and hence also on the phase difference of each frequency pair. In this way, controlling the signal is achieved by controlling the excitation probability.

$$A(\Omega) = \int_0^\infty |E_p(\omega')|\,|E^*_{St}(\omega' - \Omega)| \exp(i\,\Delta\phi)\; d\omega' \qquad (3.4)$$
$$\text{with} \qquad \Delta\phi = \phi(\omega') - \phi(\omega' - \Omega)$$

The phase difference is zero for flat phases, i.e. transform-limited pulses, and the excitation probability is thus maximized throughout the spectrum (black curve in fig. 3.3b). The arrows in fig. 3.3a show that only frequency pairs of pump and Stokes with an energy separation of Ω are in phase. The Raman excitation probability A(Ω) (eq.

[a] A commonly used unit for the applied chirp is fs^2. It describes the time shift per frequency. It can be converted to give the wavenumber shift per femtosecond using the relation $\omega = 2\pi c\tilde{\nu}$. In this case $2121\,\mathrm{fs}^2 = 2.5\,\mathrm{cm}^{-1}/\mathrm{fs}$.

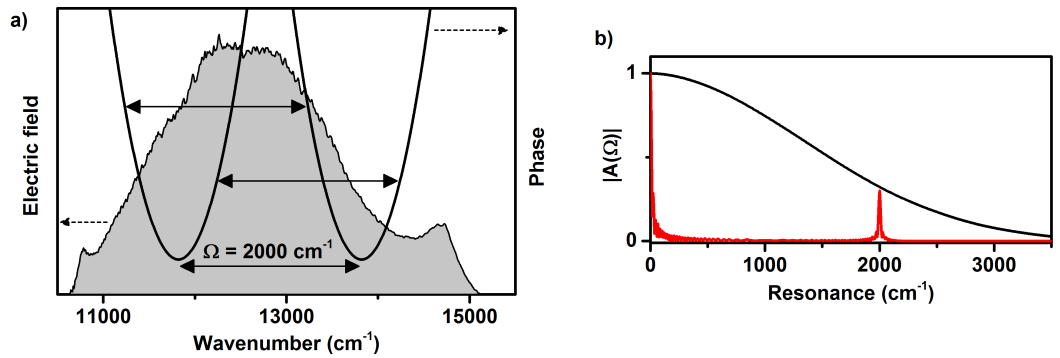

Figure 3.3: a) Electric laser field and applied spectral focusing phase function. Only the frequency pairs with a distance Ω are in phase, as indicated by the arrows, and therefore interfere positively to excite a molecule. b) Excitation probability for a transform limited pulse (black) and spectral focusing (red) as shown in a). For the simulation a chirp of 5000 fs^2 was applied to pump & Stokes, focusing on a resonance at 2000 cm^{-1}. A selected excitation is only achieved with spectral focusing.

(3.4)) is therefore maximized only for this level. This is confirmed by the simulations depicted in fig. 3.3b, red curve. The excitation is restricted to a region around the resonance, resulting in an efficient suppression of nonresonant contributions due to other frequency pairs that are out of phase.

The instantaneous frequency difference can be easily adjusted with the shaper by spectrally shifting one of the parabolas, which is equivalent to adding a linear term (ϕ_1). Again, a shift of the parabola in the frequency picture corresponds to a delay in the time-picture and thus connects the usual explanations with the one presented: the energy difference can be controlled by the time-delay of pump and Stokes. Furthermore, the instantaneous bandwidth can be independently tailored to match the Raman linewidth by varying the steepness of the parabolas (the amount of chirp).

3.2.3 Time-Frequency Picture

As we have seen, the excitation process of spectral focusing can be explained reasonably well in the time and in the frequency domain. Nonetheless, especially when taking the role of the probe into account, explanations become rather complicated in each of the domains alone. Combining them into a time-frequency map [31] provides an intuitive picture that allows for a much better understanding of the interaction of

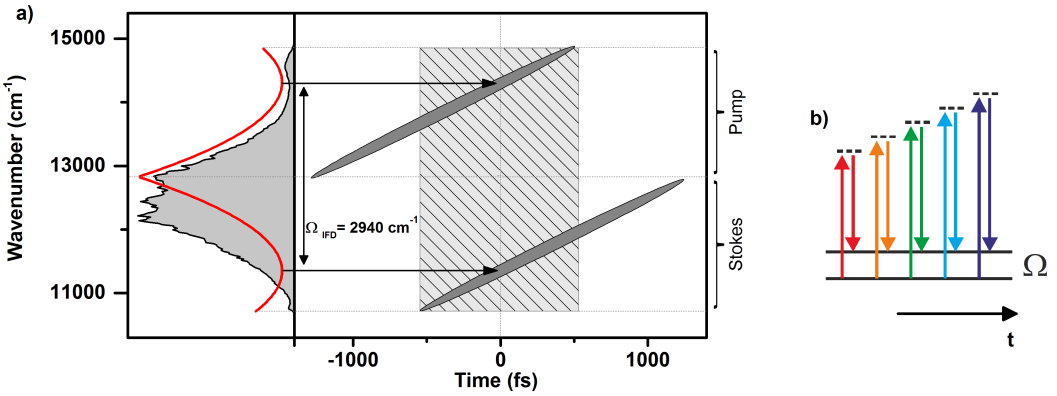

Figure 3.4: a) Spectrum and applied phase function (left panel) and time-frequency plot (right panel) showing the evolution of the instantaneous frequencies for spectral focusing at $2940\,\mathrm{cm}^{-1}$ with a positive chirp of $5000\,\mathrm{fs}^2$. Both parabolic phase functions are defined with the same distance from the center frequency of the spectrum. The overlapping pump and Stokes frequencies from the spectral wings that drive the vibrational coherence at $\Omega_{\mathrm{IFD}} = 2940\,\mathrm{cm}^{-1}$ are marked by the dashed gray box. The non-overlapping frequencies do not take part in the excitation process but can, in principle, act as probe. b) Energy schemes corresponding to the frequency pairs of the pump/Stokes overlap region in a). The constant IFD assures that the different pathways, distributed over time, lead to the same target state to coherently drive the resonance.

the different frequency regions. It also provides the basis for further developments presented in the following chapters.

Fig. 3.4a shows the time-frequency map for spectral focusing around $2940\,\mathrm{cm}^{-1}$ (region of CH-vibrations). For a better understanding of the effect of the applied phase functions, the laser spectrum and the phase (as introduced in fig. 3.3) have been added to the left side of the figure. The illustrated regions acting as the pump and Stokes can be directly transferred to the time-frequency map. The linear sweep of the instantaneous frequencies resulting from the applied chirp is shown in the right panel of the figure. In addition, the energy schemes of the corresponding time-distributed pump/Stokes frequency pairs are shown in fig. 3.4b. The spacing of the center of the parabolas determines time zero in the time domain for the two ellipses with an equal, constant slope. It therefore defines the constant instantaneous frequency difference (IFD) that focuses the excitation to a single resonance of, in this case, $\Omega_{\mathrm{IFD}} = 2940\,\mathrm{cm}^{-1}$. The shaded box marks the overlapping region of pump and Stokes frequencies that take part in the excitation process. Frequencies arriving

before or after the pump/Stokes overlap will not contribute to the excitation. Once the coherence is being built up, a second interaction with the pump (now acting as probe) generates CARS signal. When using a pulse shaper, components not taking part in the signal generation process can be blocked by amplitude shaping to reduce the incident power on the sample. It should be noted that these parts can become tremendously important for the probing process and provide the basis for the flexibility and wide potential of *tailored spectral focusing*. This and other important features like the possibility of adjusting the resolution or carrying out spectral scans will be discussed in detail in section 3.4.

3.3 Spectral Focusing and Multimodal Imaging on Human Skin Tissue [b, c]

Nonlinear optical microscopy (NLOM) combines the micrometric spatial resolution common to optical methods with 3D sectioning capabilities which gives insight into the complex organization of biological structures [10]. It has been successfully applied to imaging of biological systems in recent years [9, 11, 15]. As introduced in section 1.2, the most prominent examples of nonlinear phenomena in microscopy are two-photon excited fluorescence (TPEF), second harmonic generation (SHG) and coherent anti-Stokes Raman scattering (CARS). Often, information gained by application of different, simultaneously measured nonlinear optical methods is combined in one single image, helping to increase image contrast and thus deepening our understanding of biological structures and functions. The signals are usually spectrally separated and can therefore be simultaneously recorded with a spectrometer or with photomultipliers. This so called multimodal nonlinear microscopy (MNM) scheme has been extensively applied in several fields, like lipid imaging [99–101], the investigation of tissue development [102, 103] and label free characterization of diseases [24, 104, 105].

[b] In this section, the CARS signal is generated by the pump acting also as probe. Further development termed "tailored spectral focusing", where the probe is shaped individually will be developed in section 3.4

[c] Parts of this section have been published together with co-first author J. Rehbinder in reference [22]: “Multimodal nonlinear optical microscopy with shaped 10 fs pulses” by J. Rehbinder, L. Brückner, A. Wipfler, T. Buckup and M. Motzkus in Opt. Express 22 (2014), 28790-28797.

A common feature of all these nonlinear effects in MNM is the need for pulsed lasers for an efficient generation. High peak powers are an advantage in the generation of nonlinear signals and allow for keeping the total energy sent through the sample low. While decreasing the pulse duration to below 10 fs benefits signal intensities, excitation with tailored pulse shapes has been shown to be advantageous in NLOM. For example, in the context of nonlinear Raman microspectroscopy, tailored excitation has been used to improve the spectral resolution [70, 106, 107], to increase sensitivity [65, 108, 109] or to achieve selective excitation [77, 110, 111]. More recently, shaped pulses have been exploited to disentangle the spectrally overlapping signals of CARS and TPEF [97]. Fourier transform-limited (FTL) pulses maximize instantaneously generated signals like SHG, TPEF and *nonresonant* CARS that arise due to electronic responses of the sample. For the vibrationally resonant CARS signal on the other hand, the shortest pulses are not always the best choice [30]. The optimal ratio of image contrast and signal intensity is obtained for pulses with durations of the order of the lifetime of vibrational levels (ps range). Thus, ultrashort pulses give rise to strong but rather unspecific signal overwhelming the resonant contributions. CARS imaging with FTL pulses can be useful nonetheless because it provides a map of the density of scatterers. It can thereby help to distinguish, e.g. different cell compartments.

Within a single-beam setup containing a 10 fs oscillator and a pulse shaper, it is possible to switch between optimal conditions for multimodal imaging and resonant CARS imaging with spectral focusing by changing the phase function. Thereby, the missing specificity of the CARS signal can be restored and combined to a multimodal image now containing actual vibrational information. Furthermore, although drastically decreasing the intensities of SHG and TPEF, *simultaneous* measurements of resonant CARS, SHG and TPEF are possible when applying spectral focusing phase functions.

Due to the high cross section together with the wide distribution of molecules containing CH-groups in many fields, the CH-resonances at approximately 2850-3000 cm^{-1} are the most prominent and widely used Raman bands in CARS microscopy. Especially for biomedical applications, lipid imaging is of utmost importance. To create an image with vibrational CARS contrast, the excitation energy is focused onto a fixed resonance while raster-scanning the sample. Here, multimodal

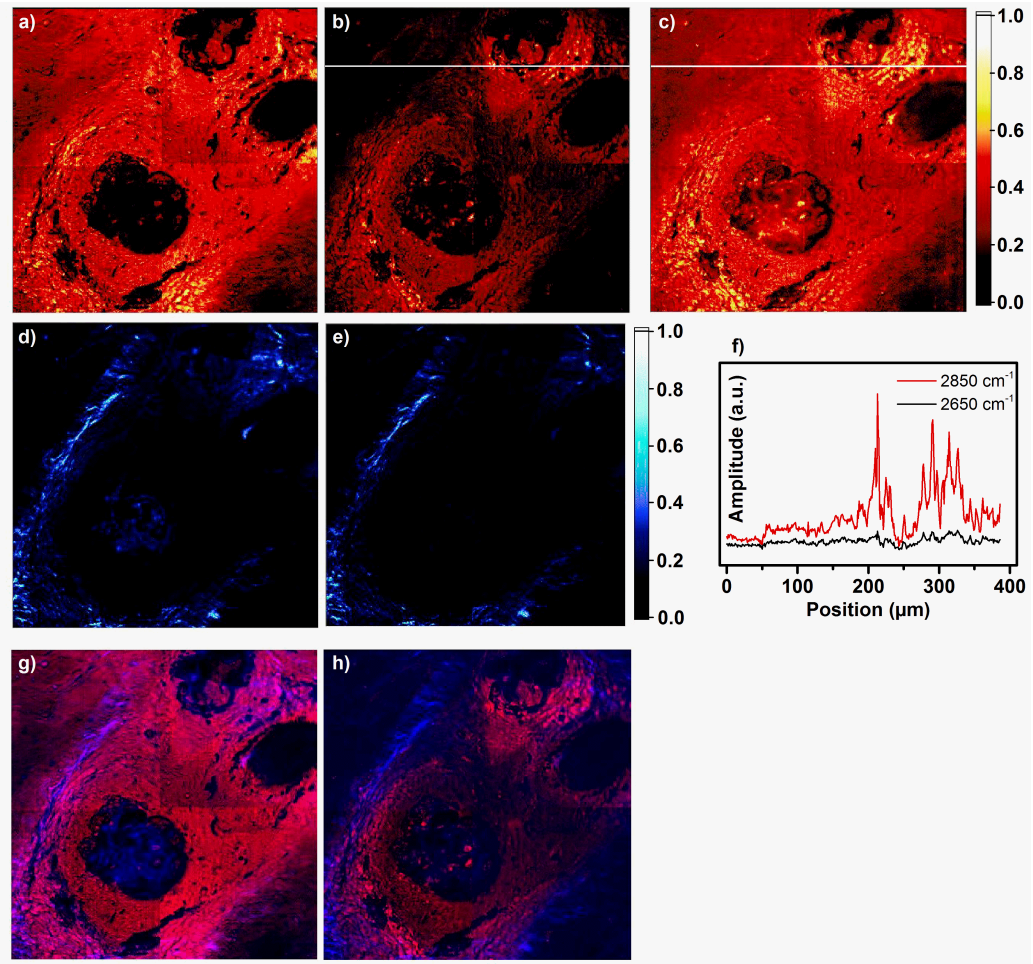

Figure 3.5: 400 µm x 400 µm images of human skin biopsies showing CARS (red) and SHG signal (blue) as well as a combined image of the two. The first column (a, d, g) was obtained with FTL excitation, the second (b, e, h) with spectral focusing at 2850 cm^{-1} (resonant with CH-vibration) and image c) with off-resonant excitation at 2650 cm^{-1}. CARS signal taken with FTL excitation (a) mainly shows nonresonant background whereas spectral focusing at the CH-vibrations (b) leads to high contrast and selective imaging of the lipid distribution. Off-resonant excitation (c) gives only very small signal with no distinct contrast as highlighted in f). f) shows the difference in signal intensity and contrast between on-resonant (red line) and off-resonant (black line) phase shaping along the white lines in b) and c). While the SHG signal intensity obtained with FTL excitation is much higher than with the spectral focusing phase function, the normalized images (d & e) show the same features and contrast. g) and h) show the resulting multimodal RGB images containing CARS (red) and SHG (blue) of the TL and on-resonance shaped pulses. For the RGB images, a background of 15% has been subtracted and the signal was then rescaled with a factor of 2 for better visibility. In all cases, spectral focusing was achieved with a chirp of 7000 fs^2.

imaging has been carried out on human skin biopsies as shown in fig. 3.5. The samples were kindly provided by Prof. Schäkel from the department of dermatology from the Heidelberg University hospital. Thin cuts from the dermis, parallel to the surface of the skin were used as received, without staining or further preparation. The imaged 400 µm x 400 µm section goes through a hair shaft with a sebaceous gland. Several measurements have been performed with FTL pulses (fig. 3.5a, d and g) and spectral focusing on-resonant (fig. 3.5b, e and h) and off-resonant (fig. 3.5c). The combined multimodal image obtained with FTL excitation is presented in fig. 3.5g. The extracellular matrix is a complex network of fibers of different kinds, where the ubiquitous collagen is the main source of the SHG signal. The poor but visible CARS-contrast in this case is only due to a change in the density of scatterers and carries no chemical information. To achieve CARS contrast without modifying the structural information depicted by the SHG channel, shaping is applied. A spectral focusing phase (GDD = 7000 fs^2, $\Omega = 2850\,\mathrm{cm}^{-1}$) is used to obtain lipid contrast, while suppressing the nonresonant background contribution (fig. 3.5b). The multimodal image obtained is shown in fig. 3.5h. As expected, a higher lipid concentration can be found around the sebaceous gland. Note that while the SHG intensity in total decreased because of the chirped excitation, the mapping of the SHG contribution did not change (compare fig. 3.5d to e). Only some details are lost due to the small signal intensities.

To illustrate the improvement in contrast obtained with shaping, a profile comparing CARS signals from focusing at $2650\,\mathrm{cm}^{-1}$ and $2850\,\mathrm{cm}^{-1}$ is shown in fig. 3.5f. The figure represents the CARS signal measured along the white lines depicted in fig. 3.5b and c. The profile in red is obtained using the on-resonance spectral focusing phase ($\Omega = 2850\,\mathrm{cm}^{-1}$) and compared to the black profile obtained when the parabolas are tuned out of resonance ($\Omega = 2650\,\mathrm{cm}^{-1}$).

3.4 Tailored Spectral Focusing [d]

3.4.1 The Potential of Tailored Spectral Focusing: An Overview

In the previous section a new approach for spectral focusing using a broadband oscillator in combination with a pulse shaper controlling the phase and amplitude was presented. However, the flexibility of the single-beam setup offers several additional advantages over other established spectral focusing implementations [22, 63, 112]. The high degree of control allows to shape the pump, Stokes *and* probe frequencies independently - what will be referred to as Tailored Spectral Focusing. While maintaining the optimal excitation of the vibrational coherence, separation and individual shaping of the probe paves the way for new improvements and developments:

- Increased CARS signal intensity with minimized nonresonant background are obtained while variably tuning the spectral resolution.
- Time-dependent measurements become possible and create contrast based on different decoherence times, allowing to distinguish overlapping modes.
- The concept becomes applicable throughout the spectrum, from CH-stretching vibrations to the fingerprint region.
- Considerably increased intensities of SHG and TPEF signals enable simultaneous multimodal imaging without even changing the phase function or the setup.

Fig. 3.6 gives a general overview of tailored spectral focusing in the time-frequency picture. It contains the basic principles developed in the previous section as well as the main modalities derived in the following.

3.4.2 The Concept of Tailored Probing

Spectral focusing has been shown to provide contrast based on molecular properties even for very complex biological samples [112]. However, signal levels are relatively

[d] Parts of this section have been published in reference [112]: “Enhancement of coherent anti-Stokes Raman signal via tailored probing in spectral focusing” by L. Brückner, T. Buckup and M. Motzkus in Opt. Lett. 40 (2015), 5204-5207 and in reference [113]: "Exploring the potential of tailored spectral focusing" by L. Brückner, T. Buckup and M. Motzkus in J. Opt. Soc. B 33 (2016), 1482-1491.

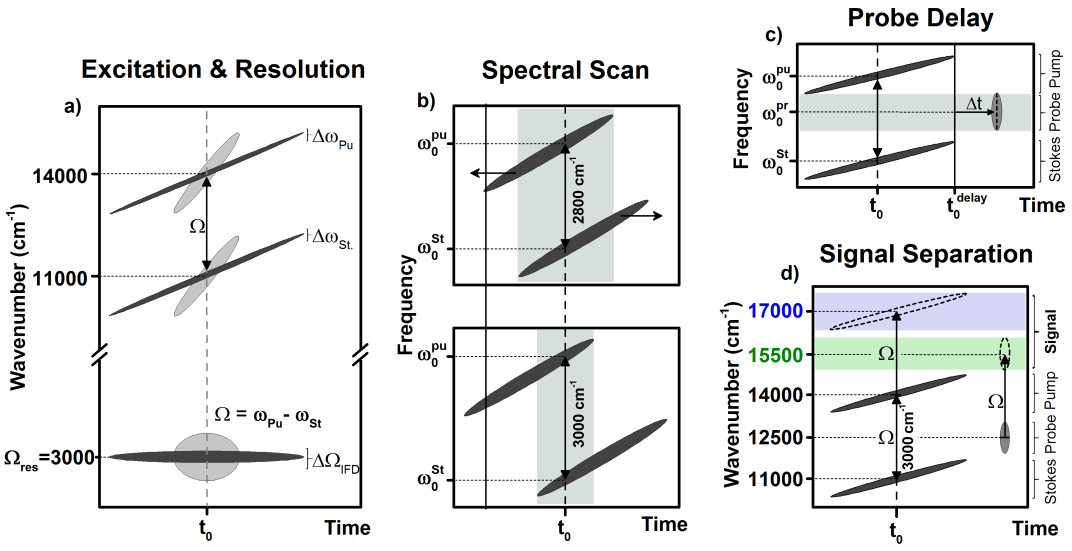

Figure 3.6: General overview of the flexibility and the main modalities of tailored spectral focusing. a) Equally chirped pump and Stokes frequencies lead to a constant instantaneous frequency difference (IFD) that drives a certain Raman mode at a frequency Ω_{res}. The spectral resolution can be controlled by the chirp of pump and Stokes and is represented by the bandwidth of the excitation $\Delta\Omega_{\mathrm{IFD}}$. b) The IFD and therefore the addressed Raman mode can be chosen by changing the time-delay of pump and Stokes. Pump/Stokes frequencies outside the overlapping region do not take part in the excitation process (gray box) and can be cut off with the pulse shaper by amplitude shaping. Continually scanning the time-delay allows to record CARS spectra. c) By identifying frequencies acting solely as probe, independent control thereof enables line scans with temporal resolution as well as increased signal levels. d) Due to the narrow excitation, signal generated by the probe (green), which lies in the region between pump and Stokes, or by the pump acting as probe (blue) can be spectrally separated. Thereby, a large part of the background is suppressed. Merging the information of a-d into a single picture provides a compact and comprehensive description of tailored spectral focusing (e.g. fig. 3.10).

low, especially when applying high chirp. Measuring samples with low concentrations of scatterers or focusing on bands besides the CH-vibrations can therefore become challenging. Further increasing the incident laser power in order to generate more signal, on the other hand, can then lead to unwanted photo damage of the sample and is usually not an option. By exploiting the flexibility and high degree of control over the spectral phase and amplitude offered by a pulse shaper, the true potential of spectral focusing can be explored.

One major drawback of all traditional spectral focusing approaches is the simul-

taneous shaping of the partly overlapping pump and probe frequencies. Although the non-overlapping frequencies of the probe pulse are strongly affected by the high amount of chirp, no effort has been put into understanding or optimizing the effect of the phase on the latter. The influence on the probe has actually not been considered at all. In any case, the only solution to this problem would be to introduce a third beam that can then be shaped independently, thereby complicating the setup even more. By using a single-beam setup, these drawbacks can be overcome. Precisely tailoring the spectral phase function not only allows to independently optimize the pump and Stokes but also the probe frequencies for maximal contrast and intensity. The development of sophisticated shaping strategies further demonstrates the potential of *tailored spectral focusing*.

The first step in developing tailored probing for spectral focusing is to identify the spectral regions acting as pump, Stokes and probe. A coherence with a vibrational level Ω is driven by the pump and Stokes frequencies. In the case of spectral focusing, equal chirp assures a constant IFD that matches the energy of the Raman level. Only frequency pairs of ω_{St} and the associated frequencies at $\omega_p = \omega_{St} + \Omega$ can therefore contribute to the excitation (fig. 3.4). In the time-frequency map in fig. 3.7 this simply corresponds to the pump/Stokes overlapping region marked by the dashed gray box (right panel of fig. 3.7a & b) or the gray areas in the spectrum (left panel of fig. 3.7a & b). Possible probing frequencies depend on both the addressed Raman level and the cut-off frequency of the filter that blocks the laser light to prevent damaging the camera. From the energy scheme of the CARS process (fig. 2.1) follows that $\omega_{pr} > \omega_{cut} - \Omega$. In other words, the probe frequency must be high enough to also generate a high-frequency signal in the spectral detection window, which is not cut-off by the filter. In the case of focusing on the CH-line of acetonitrile at $2940\,\mathrm{cm}^{-1}$ and a cut-off filter at $15\,385\,\mathrm{cm}^{-1}$ (650 nm; laser spectrum 670-930 nm), all frequencies higher than $\sim 12\,445\,\mathrm{cm}^{-1}$ (804 nm) will thus act as probe and contribute to the signal. In fig. 3.7a & b this corresponds to the regions called 'pump' *and* the ones called 'probe', while the green box marks only the part of the probe that is not overlapping with the pump frequencies. Frequencies in the green region can therefore be independently shaped to optimize the CARS signal without affecting the excitation.

It is evident that probe frequencies preceding the build-up of a vibrational coher-

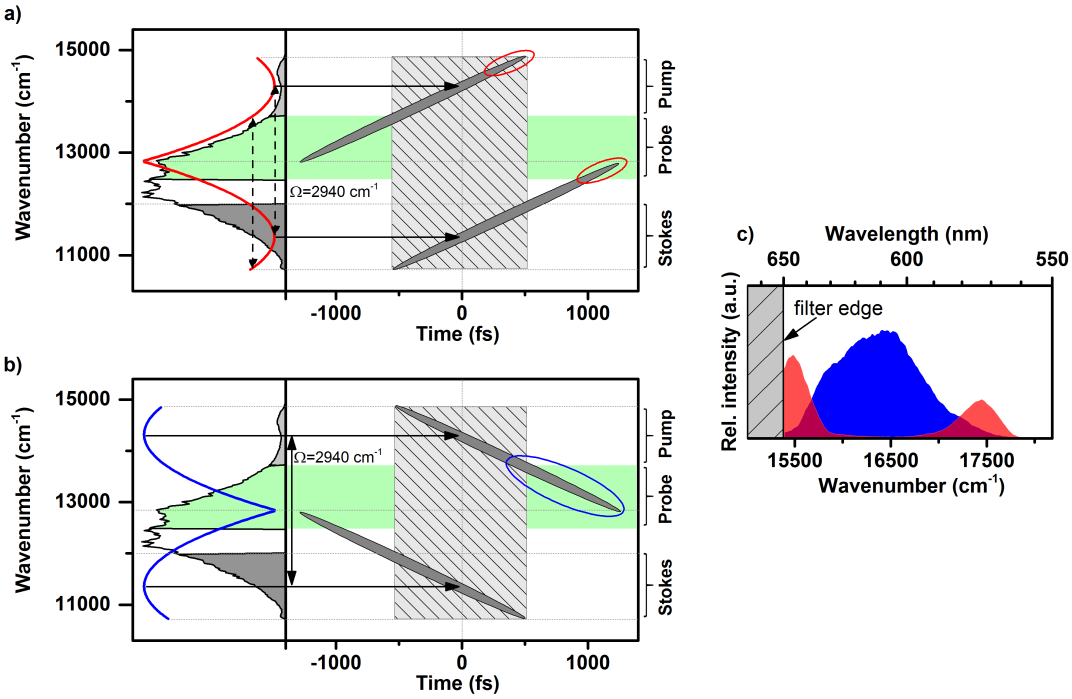

Figure 3.7: Time-frequency plots showing the evolution of the instantaneous frequencies for spectral focusing with a) positive and b) negative chirp. The pump and Stokes frequencies from the spectral wings able to reach the resonance at $\Omega = 2940\,\mathrm{cm}^{-1}$ are marked in the left panel as light and dark gray areas, respectively. Possible probe frequencies are determined by the Raman level Ω and the filter edge at 650 nm, cutting off the excitation laser light ($\omega_{Pr} > \omega_{cut} - \Omega$). The non-overlapping probe regions are marked in green. In a) a positive chirp of $5000\,\mathrm{fs}^2$ and in b) the negative analog of $-5000\,\mathrm{fs}^2$ is applied. Both parabolas have the same distance from the center frequency of the spectrum and the pump/Stokes frequency pairs with an IFD of $\Omega = 2940\,\mathrm{cm}^{-1}$ driving the vibrational coherence are marked by dashed gray boxes. c) Measured spectral focusing signals of the C–H-stretching vibration of acetonitrile for the cases shown in a) & b). The total signal is increased by a factor of ~ 2 when applying negative chirp.

ence cannot take part in the signal generation process. Thus, most of the energy of the green probing region is wasted with positively chirped pulses (fig. 3.7a). In that case, it is always advantageous to cut out frequencies that do not take part in the signal generation process by amplitude shaping to minimize photo damage [110]. As expected from fig. 3.7a, the signal from acetonitrile is only generated around $15\,500\,\mathrm{cm}^{-1}$ and $17\,450\,\mathrm{cm}^{-1}$ ($\omega_{CARS} = \Omega + \omega_{Pr}$) originating from the red-marked probe frequencies arriving at the end or after the excitation (red circles in fig. 3.7a

at 12 550 cm^{-1} and 14 500 cm^{-1}). The corresponding signal is shown as red curve in fig. 3.7c. It is important to note that the two red peaks must not be understood as a CARS spectrum: for imaging with spectral focusing, only the total integrated signal is relevant because all collected signal originates from the same resonance.

In order to enhance the CARS signal, the crossing point of the parabolas can be shifted or the phase can be replaced by its negative analog (negative chirp of equal magnitude), as shown in fig. 3.7b. Most of the probing energy is then available for signal generation, while only a small part precedes the excitation. Since a single resonance is addressed, the recorded signal frequencies can again be easily traced back to their generating probe frequencies. Hence, it can be shown that the frequencies that preceded the excitation in fig. 3.7a are now generating the signal around 16 200 cm^{-1}, as the blue curve in fig. 3.7c clearly shows. As expected, the CARS signal generated with a negative chirp is enhanced and spectrally shifted to give the opposite signal compared to when an equivalent positive chirp is applied (enhancement factor ≈ 2). The drawback of this approach is, however, that the probing frequencies are still linearly distributed in time. Some parts arrive long after the excitation, when most of the coherence has already decayed. In this case, especially the frequency components with the highest energy close to the central frequency are delayed the most. This is reflected in the fact that the integrated signal is only increased by a factor of 2, although now a lot more of the probe energy is available. For acetonitrile in the liquid phase, the induced vibrational coherence lasts long enough to still generate some signal with the highly delayed frequency components. For the imaging of biological tissue, the coherence times are expected to be considerably shorter and the probing thereby less efficient for frequencies arriving long after the excitation.

By exploiting the advantages of the pulse shaper even more, it is possible to specifically and independently tailor the non-overlapping probe region (green area in fig. 3.7 and 3.8). The parabolic spectral focusing phase functions for the pump and Stokes can be kept as before while independently optimizing the probe for the maximum signal. In this case, the coherence is driven with *all* possible frequency pairs of the pump and Stokes (gray shaded area in fig. 3.8). A linear phase function is used to cause a time shift solely in the green-marked region of the probe, allowing to probe with all possible frequencies *after the build-up* of the coherence and therefore to obtain the best signal and contrast.

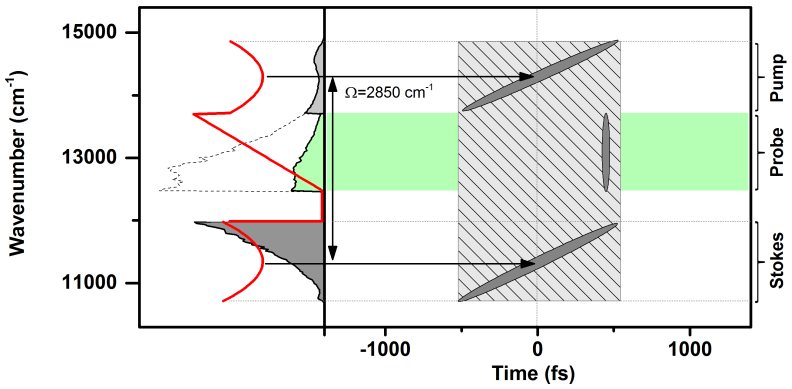

Figure 3.8: Spectrum and time-frequency plot for tailored spectral focusing. The IFD is set to the C–H-resonance of lipids at 2850 cm^{-1} with a chirp of 5000 fs^2. The frequencies acting solely as probe are uniformly reduced to only 9% of their maximum intensity by amplitude shaping and delayed in time by a linear phase function in order to maximize the signal by probing after the build-up of the coherence.

Tailoring the probe for spectral focusing is demonstrated on 40 µm cryosections of human skin tissue from the cheek in fig. 3.9. The sections were used as received, without staining or further preparation. Three measurements were done in the region between the dermis and subcutis using a TL pulse and spectral focusing with and without tailored probing. The IFD was set to the CH-vibration of lipids expected at 2850 cm^{-1} as shown in fig. 3.8. Any frequencies not taking part in the CARS process were cut out by amplitude shaping. A chirp of 5000 fs^2 was applied, which has been shown to give a good combination of signal and contrast in our setup. Applying more chirp results in a decreased signal, while only a slight enhancement of the contrast is observed. For TL measurements, the spectral intensity was reduced to 9% by amplitude shaping, resulting in 10 mW of total laser power incident on the sample. For spectral focusing, the green probe region was reduced to 9% of the maximum intensity, while the full energy was used in the wings (as indicated in fig. 3.8). This corresponds to intensities of 2 (pump), 30 (Stokes) and 3 mW (probe), or 35 mW in total. Due to the large chirp and the resulting distribution over several hundred femtoseconds, the high Stokes power did not pose problems concerning photo damage. Because of the high signal levels, the Stokes power could also have been reduced further. The TL images taken before and after more than 20 spectral focusing measurements show equal contrast, i.e., no signs of photo damage

were observed.

The implementation of spectral focusing using a time-delayed TL probe leads to a high improvement in the contrast when compared to measurements where the whole pulse was transform-limited. The poor contrast obtained with TL pulses is due to the intense but nonresonant background exceeding the generated resonant signal by several orders of magnitude. An image showing the density of scatterers with no vibrational contrast was obtained (fig. 3.9a). Tuning the phase to the C–H-stretching vibration via spectral focusing with tailored probing reveals the distribution of lipids (fig. 3.9b). In the lower right corner of fig. 3.9b, a fat cell showing high signal intensity can now be clearly distinguished from the surrounding tissue. A horizontal cut through the image (blue line) clearly shows the enhanced contrast compared to the TL case (fig. 3.9d). For a TL pulse, the contrast is not only very poor, but it is also misleading (gray curve), while for the tailored (red) and usual (black, image not shown; phase corresponding to fig. 3.7a but with $\Omega = 2850\,\mathrm{cm}^{-1}$) spectral focusing schemes, a high and practically identical contrast is achieved. This shows that the tailored probe pulse (fig. 3.8), which is actually transform limited in the case presented here, does not lead to a noticeable amount of background via interaction with the small part of the simultaneously arriving frequencies of the pump or Stokes.

Tailored probing does not only provide a much better contrast than the TL excitation, but more importantly, it also greatly increases the signal intensity compared to traditional spectral focusing (sec. 3.3 & fig. 3.9c, red and black signal, respectively). An enhancement factor of six is readily achieved. Due to the low signal intensity of the traditional method compared with the intense signal in tailored spectral focusing, a black image without visible contrast is obtained and therefore not shown here. It should be noted that the available probe intensity was attenuated by one order of magnitude to be far away from the photo-damage threshold and to prevent saturation processes or other nonlinear effects from taking place. Increasing the probe intensity will even result in further enhancement of the signal. Also, adjusting the relative Stokes and probe intensities could lead to improved signal intensity. Altogether, a signal enhancement of one order of magnitude and higher can be readily achieved. Furthermore, the technique can be easily applied to other Raman lines just by reprogramming the pulse shaper. Another very useful advantage of the presented approach is the immense increase of other nonlinear signals, like SHG and TPEF, due to the

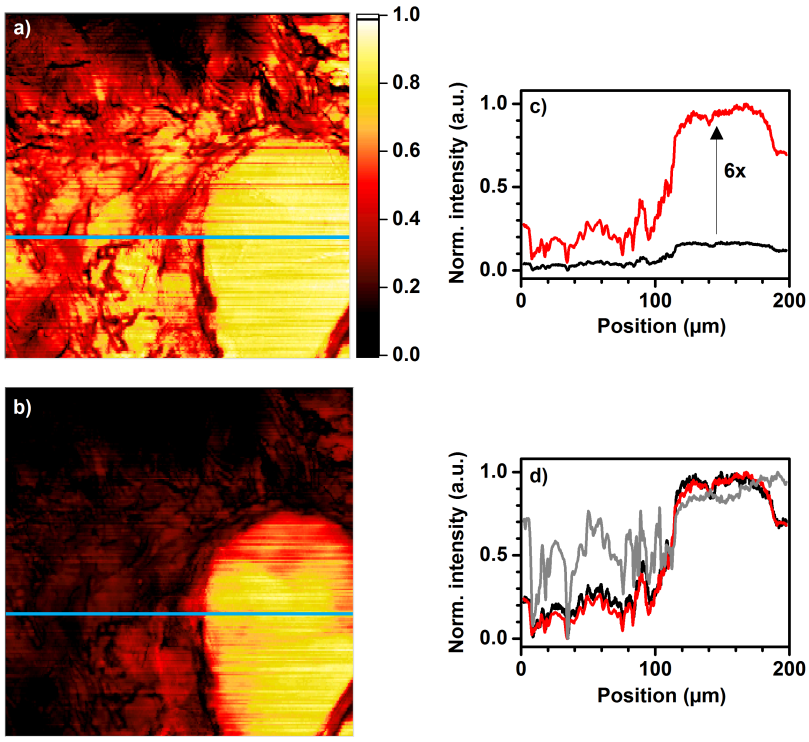

Figure 3.9: a) Image of human skin tissue containing a fat cell with a transform-limited pulse and b) the specifically tailored spectral focusing phase function as shown in fig. 3.8. The images show regions of 200 µm × 200 µm. c) illustrates the achieved signal enhancement of a factor of ∼ 6 along the blue line in b) (red) compared to usual spectral focusing without tailored probing (black). In d), the obtained contrast with (red) and without (black) tailored probing is compared to the TL measurement (gray) along the blue lines in the images. The signal outside the cell can be contributed from C–H-stretching vibrations and therefore should not just be considered to be noise.

transform-limited nature of the probing region (green area in fig. 3.8) compared to usually very long pulse durations. The experimental realization of the simultaneous measurement of CARS vibrational information and SHG or TPEF in a multimodal microscope as shown before in section 3.3 [22] is therefore highly simplified due to maximized signal intensities [112] and will be explored in even more detail in section 3.4.8.

3.4.3 A Comprehensive Time-Frequency Description

The position and range of pump and Stokes are chosen in a way to assure optimal excitation (section 3.4.2). The probe, on the other hand, can be chosen relatively freely from the remaining frequencies. In order to get a deeper understanding of how and at which spectral positions to define the probe, an extended version of the time-frequency picture (fig. 3.4) will be introduced. It forms the basis for background-free detection, time-delay scans and for the application of the concept to the fingerprint spectral region. The detection window, where the blue-shifted signals are expected to appear, is added to the time-frequency map (this is also depicted with less details and without explanations in the overview figure 3.6d). In this way it is straightforward to understand and to determine the spectral position of the probe necessary to spectrally separate signal generated by the probe and signal that is generated due to a second interaction with frequencies from the 'pump'. Fig. 3.10c shows the laser spectrum and the applied phase function. As before, the illustrated regions acting as pump, Stokes and probe can be directly transferred to the time-frequency map showing the resulting instantaneous frequencies in fig. 3.10d due to the applied positive chirp [31, 112]. The spacing of the centers of the parabolas determines time zero for the two ellipses. It defines the IFD that matches the Raman resonance Ω_{res} in the depicted case. The frequencies indicated as probe are delayed in time and arrive after the build-up of the coherence. Thereby, the signal is maximized, interactions of the probe with the pump or Stokes frequencies are prevented (see also section 3.4.4) and signal from fast decaying nonresonant contributions is suppressed. Due to the constant IFD, a coherence is continually built up and probed to generate signal in the detection window as depicted in fig. 3.10a & b. It has to be noted that the role of the different frequencies is naturally not predefined. They all can act as pump, Stokes or probe. However, if the amount of chirp is appropriately chosen, the excitation is limited to a narrow window $\Delta\Omega_{\mathrm{IFD}}$ around the Raman mode Ω_{res} (fig. 3.6a). This allows for identifying the probing frequencies that generate signal at different spectral positions ($\omega_{Pr} = \omega_{CARS} - \Omega$). Besides the region indicated as probe, the pump frequencies can act as probe, too (fig. 3.10a & b, blue part). Because of the specific excitation, the signal generated by the time-delayed probe (fig. 3.10a & b, red part) can be spectrally separated (see also fig. 3.6d). This brings a major advantage: the signal

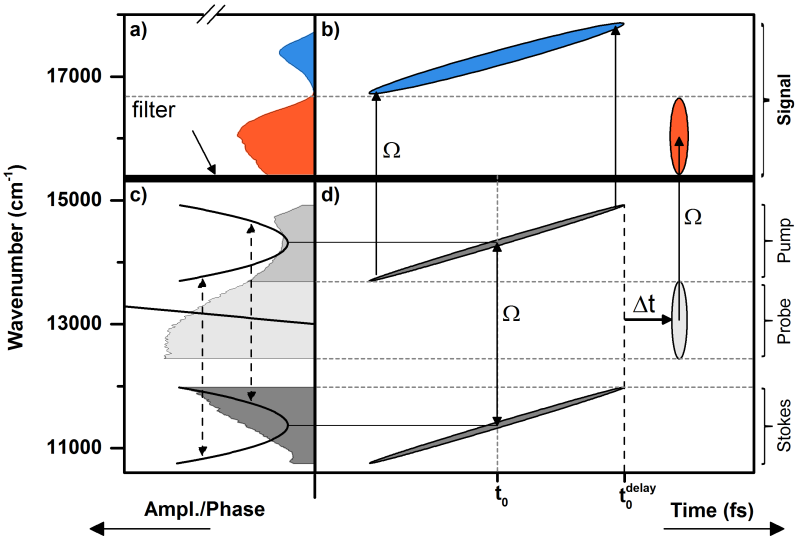

Figure 3.10: a) & b) show the blue-shifted spectral focusing CH-stretching signal of acetonitrile as measured in the experiment. c) depicts the laser spectrum with the applied phase functions for pump, Stokes and probe regions as indicated at the right side of the figure. The distance of the parabolas determines the IFD, indicated as Ω. The time-distribution of the frequencies is presented in d). From the induced coherence, the shifted signal in b) is constantly generated by the pump acting as probe (blue) and the time-delayed probe-frequencies (red). t_0^{delay} depicts the zero-point for the definition of the time delay. The integrated detector signal measured is shown by the corresponding signals in a). The steep linear probe phase is cut off to better show the parabolic phase of pump and Stokes needed for spectral focusing.

is free from background from pump and Stokes interactions. This clear separation becomes important when performing time-delay scans of the probe. On the contrary, if the applied chirp is too low, the generated signals will be smeared out, overlap and cannot be distinguished clearly. Also, note the definition of the zero-point of the probe-delay t_0^{delay} at the end of the excitation since it is of great importance for signal normalization and time-delay measurements.

3.4.4 Independent Control over Excitation and Probing

The extended time-frequency map (fig. 3.10) shows that the individual shaping of the spectrally separated probe frequencies should allow to distinguish its signal from signal due to interactions with the pump. This would open up a whole lot of new possibilities for the experiment but still needs to be proven.

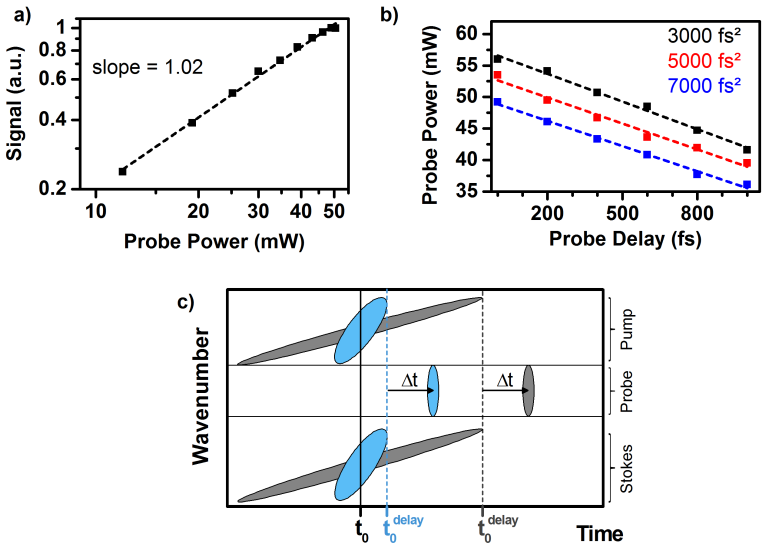

Figure 3.11: a) The spectral focusing signal generated by the time-delayed probe is linearly dependent on the probe intensity measured in the focus and confirms that it is detached from the excitation process. b) Due to space-time coupling, the probe intensity in the focus depends on the time-delay (i.e. the slope of the applied linear phase). c) The probe delay is defined as the relative delay in relation to the end of the excitation t_0^{delay}. It is therefore highly dependent on the chirp applied. Although the probe delay is identical, the phases to be applied to the probe are considerably higher for high chirp (gray) compared to low chirp (blue).

As a third-order process, the CARS signal shows a cubic dependence on the total laser intensity, which can be put in a simplified manner as $I_{CARS} \propto I_P\, I_{St}\, I_{Pr}$ (eq. (2.14)). By time-delaying the probe frequencies, the excitation process is decoupled from the probing. The signal is therefore expected to change linearly with the intensity of the probe. In the experiment this can be verified by changing the probe intensity in the focus via amplitude shaping while only measuring the resulting signal originating from the time-delayed probe (red part in fig. 3.10a & b). To measure the probe intensity in the focus, a power meter is placed at the focal position within the microscope while blocking pump and Stokes frequencies. As shown in fig. 3.11, the signal is linearly dependent on the intensity of the probe. Overlap with other signals can therefore be ruled out.

Besides, space-time coupling (sec. 2.3.4) has to be carefully considered because it has great influence on the probe power upon an applied delay. Space-time coupling

is an intrinsic effect when shaping pulses using an SLM in the symmetry plane of a 4f-setup [35, 81, 82]. It results in a modulation of both the temporal shape of an ultrashort pulse and its transverse spatial energy distribution. The effect becomes apparent when imprinting a time-delay (linear phase change) because it leads to a linear shift in space that can be easily measured by following the moving laser beam after the shaper on a CCD camera. Consequently, with increasing delay an increasing amount of the time-delayed frequencies will be blocked by the edges of the microscope objective and result in reduced intensity in the focus. This might be insignificant when applying only small delays but becomes more important with steeper linear phases.

The effect of space-time coupling is presented in fig. 3.11b. A linear relation of the probe delay and the probe power in the focus is obtained for different chirp rates. The vertical shift of the lines for different chirp is due to the definition of the probe delay. The absolute phases imprinted on the shaper are calculated in relation to a common zero-point t_0 as indicated in all time-frequency plots. The delay of the probe t_0^{delay}, however, is defined as the *relative* delay starting at the end of the excitation. It is therefore highly dependent on the amount of chirp applied to pump/Stokes. A small probe delay of, e.g. 100 fs, can thus require a very steep linear phase (i.e. high absolute delay from t_0) as indicated by the blue and gray examples in fig. 3.11c. Consequently, steeper phases have to be applied in order to achieve the same relative delay for high chirp rates. This results in increased space-time coupling that leads to the vertical shift of the measured lines in fig. 3.11b. When plotting the probe power vs. the absolute delay, all lines are perfectly coinciding and can be described by the same equation (not shown).

Due to the linear relation of CARS signal and probe intensity in the presented scheme, signal normalization becomes straightforward. The actual probe power in the focus and therefore the normalized signal can be easily calculated for every delay and every chirp applied, if necessary. This becomes particularly important when comparing absolute signal intensities in time-delay scans (section 3.4.5).

3.4.5 Contrast Based on Vibrational Coherence Times

Another advantage that comes with the implementation of spectral focusing exploiting the flexibility offered by pulse shaping is the possibility of scanning the time-delay

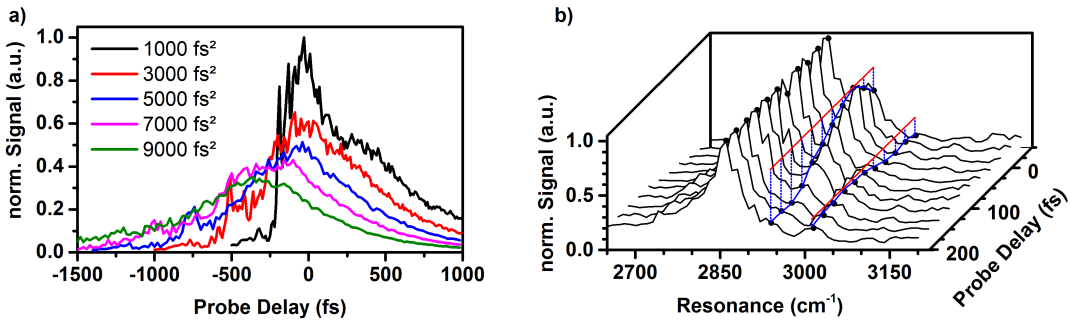

Figure 3.12: a) Probe delay scans for different amounts of chirp measuring the CH-stretching vibration of acetonitrile at 2942 cm^{-1}. The data is corrected for space-time coupling and normalized to the data at 1000 fs^2. b) Spectra for different probe delays of sunflower oil. For better comparison, the spectra are normalized to the CH-stretching vibration at 2850 cm^{-1}. At later time-delays, the asymmetric olefinic =CH-signal at 3015 cm^{-1} can be easily differentiated from the neighboring modes.

of the independently controlled probe frequencies. By detecting the spectrally separated signal generated by the delayed probe, it is possible to follow the build-up and decoherence of a Raman mode. This allows for the minimization of the nonresonant background even at the resonance position. Furthermore, monitoring the decoherence of different vibrational states can be used for spectroscopy and imaging purposes.

Fig. 3.12a shows time-delay scans when focusing on the resonance of acetonitrile at 2942 cm^{-1} for different chirp rates. The probe delay denotes the time after the end of the excitation as calculated from the group delay of pump and Stokes (fig. 3.11c & 3.10). With increasing chirp, the frequencies are dispersed over a longer period of time, which is reflected in the longer build-up of the coherence. While for low chirp (<500 fs^2, not shown) nonresonant contributions are still present around time zero, higher chirp already reduces its generation to a very high extent even without additional delay of the probe. It has to be noted that care must be taken when interpreting the data at negative time delays. There, due to the simultaneous arrival, the probe can in principle also act as pump or Stokes, generating signal in the detection window. However, at high chirp rates, the influence of generated signal due to the probe acting as pump or Stokes becomes insignificant. For time-delay scans the signal is expected to decrease starting at the end of the excitation, i.e. at zero probe delay. At a chirp of 1000 fs^2, the data agrees well with the expectations while

for increasing chirp rates the reversal point is shifted to negative delays. Because the delay is calculated based on the extent of the dispersion of pump/Stokes, it highly depends on the definition of the pump/Stokes spectral regions. At higher chirp, the end of the excitation occurs earlier than in the calculated case because the low-intensity frequencies from the wings only have little contribution to the CARS signal but still define the zero-point of the axis. This axis, however, can be easily adjusted relative to the reversal point without losing information (not shown).

In fig. 3.12b the concept is extended to follow the evolution of the CH-vibrations of sunflower oil [114]. Measuring the spectra as a function of the probe delay reveals differences in the decoherence times, which can be exploited for imaging and spectroscopy. While the asymmetric olefinic =CH-signal at $3015\,\mathrm{cm}^{-1}$ increases with the probe delay, the signal at $2940\,\mathrm{cm}^{-1}$ decreases in relation to the symmetric CH-stretch at $2850\,\mathrm{cm}^{-1}$. Only two peaks are distinguishable at early probe delay and are partly overlapping the weak signal at $3015\,\mathrm{cm}^{-1}$. Delaying the probe, however, allows to distinguish the Raman modes even at low chirp rates solely based on the faster decay of the signal at $2940\,\mathrm{cm}^{-1}$. In fig. 3.12b the olefinic CH-vibration is clearly resolved at a delay of 200 fs.

3.4.6 Spectral Resolution

Influence of the Phase Function

The influence of the applied phase functions on the spectral resolution and on background suppression is presented in fig. 3.13. For clarity and simplification, the interference with nonresonant contributions is initially omitted and only purely resonant signals are considered. This is justified because it closely resembles the experiment: In tailored spectral focusing, nonresonant parts are drastically reduced when detecting only the spectrally separated signal generated by the time-delayed probe (red signal in fig. 3.10a & b). As explained previously, the steepness (ϕ_2: quadratic phase function) of the parabolas controls the amount of chirp and therefore the instantaneous bandwidth $\Delta\omega$ of pump and Stokes. Its influence on the pulse is displayed in the time-frequency map of fig. 3.13. The higher the chirp, the narrower the instantaneous bandwidth becomes and the longer the frequencies are stretched in time. The equal amount of chirp applied ensures a constant IFD and also leads to equal

bandwidths $\Delta\omega$ of pump and Stokes. Hence, the range of the IFD, as determined by the convolution of pump and Stokes, is controlled by the chirp ($\Delta\Omega_{\mathrm{IFD}}$ in fig. 3.13a). Besides, the linear phase function of the probe solely leads to a delay in time, which is used here to suppress the generation of nonresonant background. Fig. 3.13b and c show how the amount of chirp affects the measured linewidth of a Raman level Ω_{res} (green rectangle) when the IFD is detuned by $\Delta\Omega$. At a given point in time, the pump frequencies create virtual levels within a range of approximately $\Delta\omega$ and interact with the simultaneously arriving Stokes frequencies, that itself cover a range of $\Delta\omega$ (compare to fig. 3.13a). The possible pump/Stokes frequency pairs at each point in time will therefore cover a range $\Delta\Omega_{\mathrm{IFD}}$ as defined by the convolution of pump and Stokes frequencies (eq. (2.15), fig. 3.13a bottom panel). In this simplified picture, it is obvious that the measured linewidth, as shown in fig. 3.13c, is highly dependent on the range of pump/Stokes frequency pairs at one point in time, even when only considering resonant contributions.

The maximum signal is generated when the instantaneous frequency difference coincides with the Raman line, i.e., $\Omega_{res} = \Omega_{\mathrm{IFD}}$ (case No. 2, fig. 3.13). If the applied chirp is too small, as depicted by the red phase in fig. 3.13a and left scheme in fig. 3.13b, the bandwidth of the excitation $\Delta\Omega_{\mathrm{IFD}}$ is broader. When detuning the IFD, the Raman level is still covered to some extent. Thus, resonant signal is created although the center of excitation is already outside the linewidth. This results in a broadened measured linewidth as depicted in fig. 3.13c (cases Nos. 1 & 3). By applying steeper parabolas and thus higher chirp, as shown in the right scheme of fig. 3.13b, the improved accuracy of the IFD ($\approx 2\Delta\omega$) leads to a more focused excitation when detuned by the same frequency $\Delta\Omega$. The frequency pairs do not coincide with the Raman level anymore and lead to a narrower measured linewidth. The limiting width is given by the natural linewidth of the Raman resonance and cannot be improved by increasing the chirp. Additional chirp only stretches the pulses in time and leads to decreased signal levels while maintaining the linewidth.

Furthermore, the flexible adjustment of the instantaneous bandwidth to varying Raman linewidths allows for the suppression of the otherwise overwhelming nonresonant background of broadband pulses. The excitation is focused to a small region around the resonance and the excitation of any virtual levels nearby (dashed lines in fig. 3.13b) is minimized. Also, since a higher chirp results in stretched pulses, the

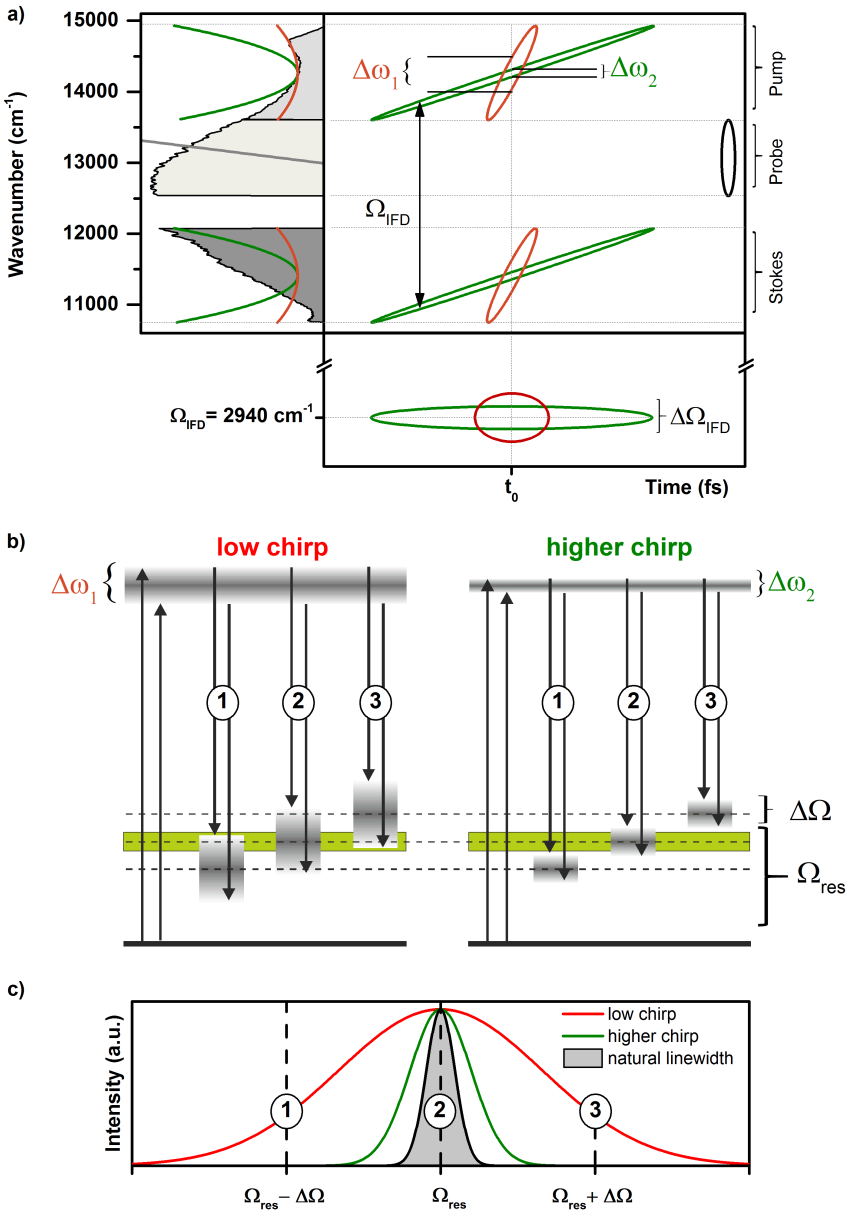

Figure 3.13: Influence of the chirp rate on the measured linewidth. a) Phase, time-frequency plot and the resulting instantaneous bandwidth for low ($\Delta\omega_1$, red) and significantly higher chirp ($\Delta\omega_2$, green). The convolution of pump and Stokes determines the instantaneous frequency difference (IFD). b) Excitation process following from the phases in a). The combination of the instantaneous bandwidths of pump and Stokes leads to excitation within a range $\Delta\Omega_{\mathrm{IFD}}$ around a selectable center frequency Ω_{IFD}. In case No. 2 the IFD coincides with the resonance while in Nos. 1 & 3 it is detuned away from the resonance by $\Delta\Omega$ c) The spectral resolution increases with the chirp rate and approaches the natural linewidth (gray area).

nonresonant contributions are decreasing, while resonant coherence is continuously built up until the interaction with the probe frequencies generates signal in the detection window. The possibility to flexibly adjust the chirp to match the bandwidth $\Delta\Omega_{\mathrm{IFD}}$ with the linewidth of a Raman level demonstrates one of the main advantages of implementing spectral focusing with a pulse shaper.

Linewidth: Measurement vs. Simulation

Fig. 3.14 shows spectral focusing measurements and simulations of the CH-resonance of acetonitrile at $2942\,\mathrm{cm}^{-1}$ for different amounts of chirp. The inset displays the extracted full width at half maximum (FWHM) value and therefore the dependence of the obtained spectral resolution on the applied chirp. The simulation was carried out using the definitions and equations presented in section 3.2 (eqs. (2.14) to (2.17)). The generation of nonresonant background was minimized by delaying the probe to arrive 300 fs after the end of the excitation. A very good agreement of simulation and experiment confirms the justification of the employed simulation as well as correctly applied phase functions in the experiment. As expected from the explanations above, the linewidth strongly depends on the applied chirp and can be used to control the spectral resolution within the limits of applicable phase functions. The implementation of spectral focusing in a single-beam CARS experiment containing a pulse shaper therefore allows for fast and flexible adjustment and optimization of resonant signal levels as well as good spectral resolution while suppressing most of the nonresonant background.

3.4.7 Spectral Focusing in the Fingerprint Region

Exploiting the flexibility of the pulse shaper allows to extend the spectral range of the presented scheme to the fingerprint region. By appropriately choosing the frequency regions from the broadband laser spectrum, CH-stretching vibrations of functional groups as well as the low-wavenumber region can be reached. The fingerprint region as a whole carries most of the molecule's specific structural chemical information, making it the key part of a spectrum to even distinguish molecules with small differences. While the pump and Stokes regions can be chosen arbitrarily from all over the spectrum to drive the coherence of a chosen resonance, the probe frequencies, however, are

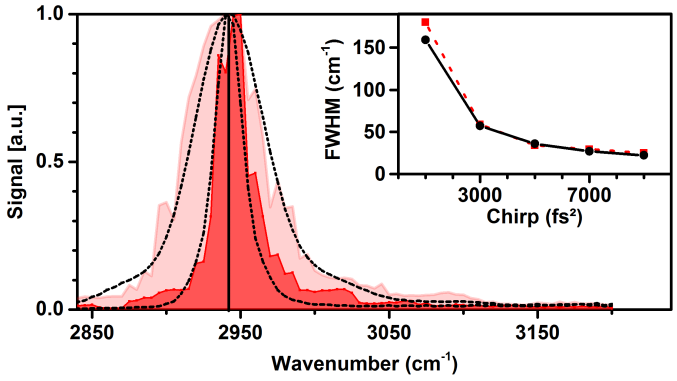

Figure 3.14: Comparison of the measured (red) and simulated (black) linewidths obtained for the CH-stretching vibration of acetonitrile at 2942 cm^{-1} in dependence of the amount of chirp applied. The measured spectra for 3000 fs^2 and 9000 fs^2 are depicted in light and deep red, respectively. The inset shows the obtained FWHM of the lines in dependence of the chirp. The probe was delayed in all cases to 300 fs after the end of the excitation.

also determined by the position of the detection window $\omega_{CARS} = \omega_{Pr} + \Omega > \omega_{\mathrm{cutoff}}$, as discussed earlier in section 3.4.2. When applying spectral focusing in the fingerprint region, the order of the pump and probe regions has to be swapped to still shift the signal to the detection window and bypass the cutoff filter. Fig. 3.15a shows the excitation and the signal generation along with the applied phase function for the measurement of the resonance of toluene at 1004 cm^{-1}. In order to prevent destruction of the sample due to high laser power, the intensity of the laser was reduced to 30 % and unwanted frequencies as well as the ones not taking part in the signal generation process cut out by amplitude shaping. Thereby, the intensity remains constant when performing a spectral scan. A low-pass filter at 700 nm was chosen and the blue wing of the spectrum (i.e. all wavelengths below 700 nm) blocked in the Fourier plane of the shaper. The scheme also allows to choose the probe frequencies in a way that the generated signal overlaps with the blue wing of the spectrum. Because the blue wing is coherent in space and time with the generated spectral focusing signal, heterodyne measurements in the fingerprint region are feasible when omitting the filter (not shown) [65, 109]. In fig. 3.15a, pump and Stokes drive the coherence at Ω and are probed by the time-delayed frequencies indicated to generate resonant signal (red part). Due to the changed order of pump and probe, signal generated by the

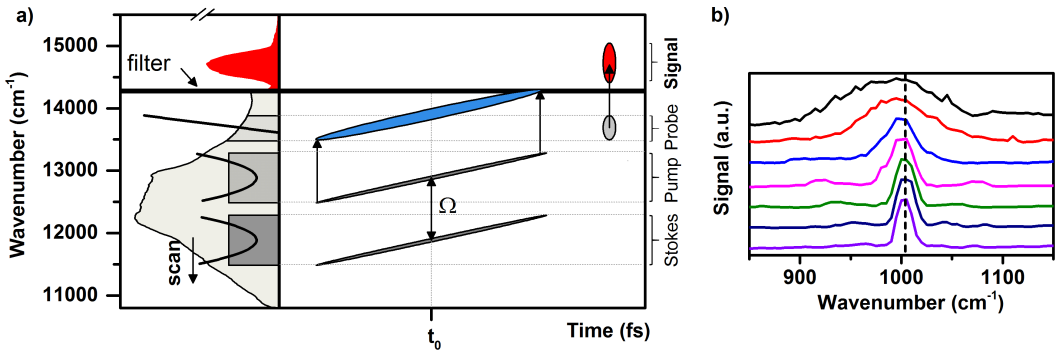

Figure 3.15: a) shows the blue-shifted spectral focusing signal in the fingerprint region of toluene as measured in the experiment. The incident spectrum and the applied phase functions for pump, Stokes and probe regions (dark gray) are depicted in the left part of a). Note that their order has changed compared to fig. 3.10. Unwanted frequencies have been cut out from the laser spectrum (light gray, background) by amplitude shaping. The time distribution of the frequencies is depicted in the right panel. The signal generated by the pump acting as probe (blue) cannot pass the filter at 700 nm (14 285 cm^{-1})so that the detector records only signal generated by the time-delayed probe frequencies (red). b) Influence of the amount of chirp on the measured linewidth of toluene of the band at 1004 cm^{-1}. Applied chirps from top to bottom are: 2000 fs^2, 3000 fs^2, 5000 fs^2, 7000 fs^2, 9000 fs^2, 12 000 fs^2 and 15 000 fs^2. In the case of 15 000 fs^2 a linewidth of 17 cm^{-1} is achieved. The delay of the probe was set to 200 fs after the end of the excitation.

pump acting as probe (blue part) will in this case not pass the filter. By scanning the steepness and the spacing of the parabolas, spectra of toluene in dependence of the chirp are obtained. Fig. 3.15b shows the measured Raman lines at 1004 cm^{-1} with increasing spectral resolution, corresponding to increased chirp. The slight shift to lower wavenumbers when applying low chirp can be explained by interference with nonresonant signal, resulting in the well-known dispersive lineshapes of the CARS signal. In this case, the bandwidth of the excitation ($\Delta\Omega_{\mathrm{IFD}}$, fig. 3.6a & 3.13a) is too broad so that the pump acting as probe is generating a broad nonresonant signal that leaks into the detection window and interferes with the resonant one originating from the actual time-delayed probe. Again, this shows the importance of choosing the right amount of chirp.

3.4.8 Simultaneous Multimodal Imaging

Signals like second-harmonic generation (SHG) or two-photon excited fluorescence (TPEF) [8], which are often used in multimodal microscopy, benefit from short femtosecond pulses. The signal intensity of the nonlinear process of order n scales with the duration τ of the pulse $S \propto 1/\tau^{(n-1)}$ [10]. In picosecond CARS experiments, however, two tunable picosecond lasers are used in order to improve contrast and spectral resolution and are therefore not well suited for multimodal imaging. As has already been discussed, spectral focusing is essentially able to achieve similar resolution by stretching initially very short fs-pulses in time. Unfortunately, this also leads to significantly reduced SHG and TPEF signal levels. Although multimodal imaging with spectral focusing was achieved in section 3.3, signal levels were very low. The application is therefore restricted to certain samples or structures with high concentrations of scatterers (like the ubiquitous collagen in the dermis of the skin). Also, high incident laser power has to be used in order to generate enough signal, which further restricts the application to samples with a high damage threshold.

Optimal multimodal imaging with the best contrast and signal intensity can thus, at least in conventional setups, only be achieved by switching between fs-pulses and spectral focusing, performing two measurements. One exception is the use of ultrabroadband 5 fs lasers in a specialized and complex setup [115]. However, in the framework of tailored spectral focusing, simultaneous measurements of spectrally separated SHG and TPEF as well as resonant spectral focusing CARS signal is readily possible. Due to the transform-limited nature of the delayed probe, the signal levels of SHG and TPEF are significantly increased compared to usual spectral focusing with a highly chirped probe. In addition, it is possible to distinguish overlapping signals based on their different dependence on the phase of the incoming laser beam [97]. Fig. 3.16 shows the obtained multimodal images of human skin tissue. When transform-limited pulses are applied, the CARS signal gives the structure (fig. 3.16a) while spectral focusing at $2850\,\mathrm{cm}^{-1}$ allows for selectively imaging lipid cells due to their strong CH-resonance (fig. 3.16b). Fig. 3.16c highlights the achieved contrast along the blue lines in fig. 3.16a (gray background) & b (black line). The simultaneously recorded SHG image in fig. 3.16d illustrates the distribution of collagen and shows signal between lipid cells. The TPEF signal in fig. 3.16e is also simultaneously

recorded with the same spectral focusing phase function. The data is combined in an RGB image in fig. 3.16f that shows the complementary information of the multimodal signals as well as distinct discrimination between cells and neighboring tissue.

3.5 Conclusions

In conclusion, a novel scheme for spectral focusing CARS microspectroscopy based on flexible control of the spectral phase and amplitude by elaborated shaping of sub 10 fs pulses has been developed. Exploiting the flexibility of a pulse shaper allows for independent control over the pump, Stokes and probe frequencies in the focus of a microscope. Raman modes of complex samples from the fingerprint to the CH-region around 3000 cm^{-1} are accessible just by switching the applied phase function. The instantaneous bandwidth of pump and Stokes can be variably adjusted to the linewidths of different Raman modes throughout the spectrum, optimizing spectral resolution and signal intensity. By identifying frequencies taking part in the signal generation process, the potential of independently shaping the probe can be explored. Detailed simulations of the single-beam CARS signal for different phase functions confirm the experimental results. Delaying the probe allows for a full build-up of the coherence while signal due to other parts of the spectrum acting as probe can be spectrally separated. Therefore, increased signal levels with minimized nonresonant background are obtained. Due to the transform-limited nature of the time-delayed probe, nonlinear signals like SHG or TPEF are significantly enhanced. Contrast obtained with spectral focusing and simultaneous multimodal imaging is demonstrated by measurements of human skin tissue. Furthermore, the possibility of creating contrast based on differences of the decoherence times of molecular vibrations is exemplarily shown on the CH-modes of sunflower oil. Implementing spectral focusing into a SB-CARS setup by imprinting arbitrary phase functions on fs-pulses with a pulse shaper therefore offers advantages over alternative implementations and a wide range of possibilities for further development.

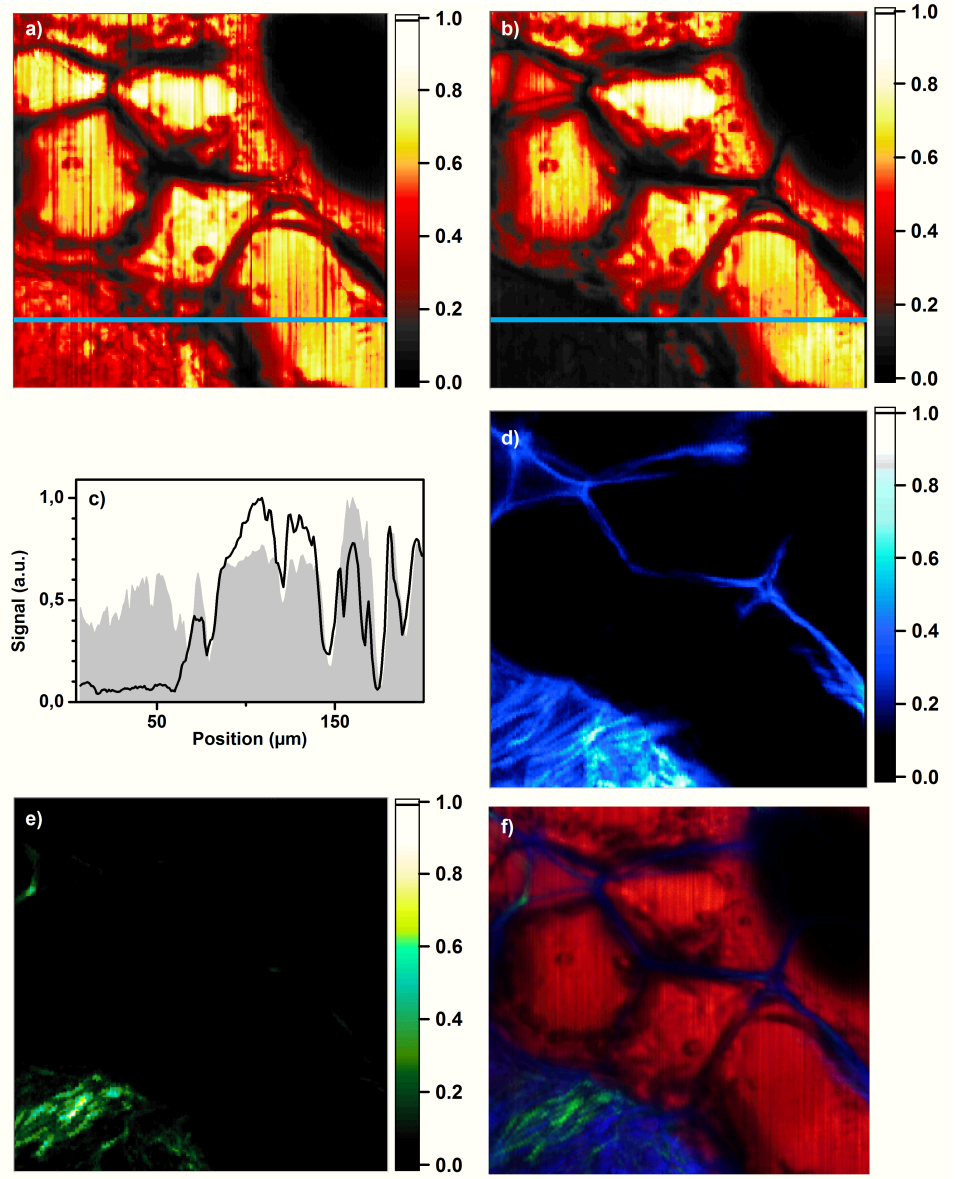

Figure 3.16: Multimodal imaging of 200 µm × 200 µm human skin tissue with a transform-limited pulse (a) and spectral focusing (b, d-f). c) illustrates the high contrast achieved with spectral focusing (black line) compared to TL-pulses (gray background) along the blue lines in a & b. The images show CARS (a, b), SHG (d) and TPEF-signal (e). A multimodal RGB image (f) is constructed by combining the simultaneously collected CARS (red), SHG (blue) and TPEF (green) data obtained with a spectral focusing phase function. The chirp was set to 3000 fs^2 and the probe was delayed 100 fs after the end of the excitation. Signals were collected using photomultipliers and bandpass filters (CARS: 640±10 nm, SHG: 400±10 nm, TPEF 500 ± 20 nm).

4 Towards a Tunable IR Light Source

This chapter deals with the prerequisites, challenges and arising possibilities of developing a tunable mid-IR (MIR) light source as exciting new modality for single-beam nonlinear microscopy. While the frequencies delivered by a Ti:Sa laser allow to directly address electronic transitions, the lower lying vibrational levels can only be accessed through Raman-type processes like CARS. The enhanced coupling between the field and molecular motions provided by direct excitation with IR light, however, offers many advantages for molecular spectroscopy. By interaction of the frequencies with molecular states, resonant molecular information can be probed for, e.g., ultrafast spectroscopy [116–118] or selective bioimaging [13, 16, 46]. Hence, unlocking the IR spectral region for the single-beam approach would pave the way for exciting developments to complement the existing toolbox of modalities. For example, implementing IR microscopy and combining it with the complementary contrast obtained from nonlinear Raman measurements would provide unprecedented spectroscopic flexibility.

The high amount of control over the spectral phase presents a unique possibility to not only generate infrared frequencies but to develop a *tunable* broadband IR source based on the coherent control of the difference-frequency generation (DFG) process. Typical vibrational spectra are ranging from 500 to 3500 cm^{-1} corresponding to wavelengths of 2.5 to 20 µm. While the broadband spectrum of the Ti:Sa laser used within this thesis provides the spectral range, the actual frequency conversion efficiency is determined by the chosen nonlinear crystal, its phase-matching requirements as well as its transmission properties. Besides discussing different detection schemes and the actual results obtained, these important points will be addressed in this chapter.

4.1 Generation of Infrared Pulses

Ultrashort MIR pulses are usually obtained by phase-matched difference frequency generation (DFG) in nonlinear crystals like $AgGaS_2$, $AgGaSe_2$ or GaSe. Complicated setups have been developed to provide two input pulses of different frequencies to cover the MIR spectral range. For example, the generation and subsequent mixing of signal and idler frequencies from an optical parametric oscillator (OPO) [119–122] or from two synchronized Ti:Sa lasers has been shown [123]. However, one way to significantly simplify the experimental setup is to directly mix the frequencies from within an ultrabroadband spectrum of a femtosecond Ti:Sa laser [124–127] (of course, frequencies generated by other sources like Er-doped fiber lasers can be mixed in a DFG approach as well). In common nonlinear crystals, the phase-matching condition is only fulfilled for a narrow range of IR frequencies at a time. By adjusting the phase-matching angle, i.e. rotating the crystal, it is possible to select the frequencies to be generated. In a different approach, an ultrabroadband MIR spectrum ranging from 3 to 7 µm was obtained without the need for angle-tuning by collinear phase-matched interaction of a single 7 fs Ti:Sa laser in a thin $LiIO_3$-crystal [128].

4.1.1 Difference Frequency Generation

When focusing a short laser beam on materials without inversion symmetry, a nonzero $\chi^{(2)}$-tensor can lead to different frequency mixing processes [51, 73] (see also sections 1.2 & 2.1.1). Besides sum-frequency interactions, the opposite process of difference-frequency generation (DFG) can occur as well and makes MIR radiation accessible for time-resolved spectroscopy. However, because of dispersive properties of the crystal, different frequencies will travel with a different velocity. Especially the resulting dephasing of the incident and the generated frequencies prevents an efficient signal build-up. Hence, in order to generate intense signal phase-matching has to be fulfilled. A common way to achieve the phase-matching condition is to exploit the birefringent properties of certain nonlinear crystals (see also explanations in section 2.3.2 about the birefringent liquid crystals of the shaper).

Uniaxial crystals show two different refractive indexes. The extraordinary refractive index $n_e(\theta, \omega)$ is parallel to the optical axis and changes depending on the angle with respect to the propagation of light (eq. (4.7)). The ordinary refractive index $n_o(\omega)$ is

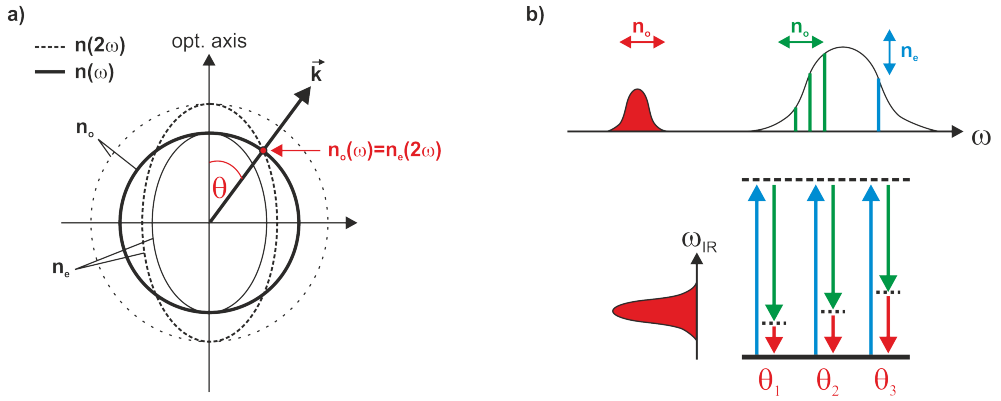

Figure 4.1: a) For an SHG process phase matching can be achieved by adjusting the angle θ between the optical axis and the propagation of light. An incoming wave polarized parallel to the ordinary axis of the crystal will result in a perpendicular polarization of the doubled frequency (parallel to the extraordinary axis). b) Energy diagram and required polarizations for type I difference frequency generation (DFG). Interaction of the frequencies within the broadband laser spectrum can lead to IR signal. Each frequency pair requires a different phase-matching angle for optimal dispersion compensation. Usually this is achieved by rotating the crystal to tune the angle θ.

perpendicular to the optical axis and independent of the angle. By choosing the right polarizations and angles θ between the optical axis and the direction of the incoming frequencies, phase matching can be achieved. The angle and frequency dependences are generally expressed in the form of energy and momentum conservation [129]. In the case of an SHG process energy ($\omega_2 = 2\omega_1$) and momentum conservation ($k_2 = 2k_1$) determine the required phase-matching angle as well as the polarizations. With the relation $k = \frac{\omega \cdot n}{c_0}$ and the usual behavior that refractive indexes increase with the frequency, the solution for a negative uniaxial crystal ($n_e(\theta) \leq n_o$) can be easily obtained. In the relatively simple case of an SHG signal, this can be illustrated as shown in fig. 4.1.

$$n(\omega_2) = \frac{2\omega_1}{\omega_2} \cdot n(\omega_1) = n(\omega_1) \quad \Rightarrow \quad n_e(2\omega, \theta) = n_o(\omega) \tag{4.1}$$

In the case of a general three wave interaction, the dependences are similarly expressed in the form of energy and momentum conservation [129]. However, the depen-

dencies cannot be simplified as much as in the case of SHG and need to be calculated from the derived equations.

$$\omega_1 = \omega_3 - \omega_2 \qquad \text{where} \quad \omega_3 > \omega_2 > \omega_1 \tag{4.2}$$

$$k_1 = k_3 - k_2 + \Delta k \qquad \text{with} \quad k = \tfrac{\omega \cdot n}{c_0} \tag{4.3}$$

$$\omega_1 n(\omega_1) = \omega_3 \cdot n(\omega_3) - \omega_2 \cdot n(\omega_2) \tag{4.4}$$

For negative uniaxial crystals there exist only two solutions to achieve phase-matching, which are referred to as type-I and type-II

$$n_e(\theta, \omega_3) = \underbrace{\tfrac{\omega_1}{\omega_3} \cdot n_o(\omega_1) + \tfrac{\omega_2}{\omega_3} \cdot n_o(\omega_2)}_{\substack{\text{SFG type I: } o{+}o{\to}e \\ \text{DFG type I: } e{-}o{\to}o}} \tag{4.5}$$

$$n_e(\theta, \omega_3) = \underbrace{\tfrac{\omega_1}{\omega_3} \cdot n_e(\theta, \omega_1) + \tfrac{\omega_2}{\omega_3} \cdot n_o(\omega_2)}_{\substack{\text{SFG type II: } e{+}o{\to}e \\ \text{DFG type II: } e{-}e{\to}o}} \tag{4.6}$$

$$\frac{1}{n_e(\theta, \omega)} = \frac{\cos^2(\theta)}{n_o^2(\omega)} + \frac{\sin^2(\theta)}{n_e^2(\omega)} \tag{4.7}$$

The equations are rearranged to express the unknown extraordinary index. They thereby actually have the same form as if formulated for the SFG process. These equations determine the polarizations of the incoming waves with respect to the optical axis and predict the polarization of the generated signal, also shown in fig. 4.1b. By plugging in the values for the polarization dependent refractive indexes, the necessary $n_e(\theta, \omega_3)$ is obtained. The required phase-matching angle can then be calculated using the index ellipsoid relation (4.7). Frequencies that can be used for the DFG process are not only limited by the transmission range of a crystal but also by the values of the ordinary and extraordinary refractive indexes.

4.1.2 Lithium-Iodate for Broadband IR Generation

The prerequisite for developing a mid-IR light source is to achieve phase-matching over a broad range of frequencies. Usually, phase-matching cannot be achieved over

broad spectral regions simultaneously. By rotating the crystal it is however possible to subsequently achieve phase-matching for different frequency pairs and thereby generate different IR-frequencies one after the other. For the generation of a broad IR-spectrum, simultaneous phase-matching for many different frequencies is required. As discussed in the previous chapter, whether phase-matching is possible depends on the interacting frequencies and on the properties of the crystal. To enable the generation of an IR spectrum as broad as possible, a lithium-iodate ($LiIO_3$) nonlinear crystal was chosen. In this special case, many of the frequencies of a ultrabroadband Ti:Sa laser around a central wavelength of 800 nm can be simultaneously and collinearly phase-matched by a type I DFG process in a thin $LiIO_3$ crystal [128]. The required polarizations known from eq. 4.5 are depicted in fig. 4.2. To achieve the maximum generation efficiency, the spectrum is divided at the central frequency. Polarization shaping is used to align the 'red' frequencies perpendicular and the 'blue' frequencies parallel to the extraordinary axis (4.2a & b). At normal incidence, the chosen crystals were cut to have a phase-matching angle of $\theta = 20.1°$ (fig. 4.2c) as calculated from

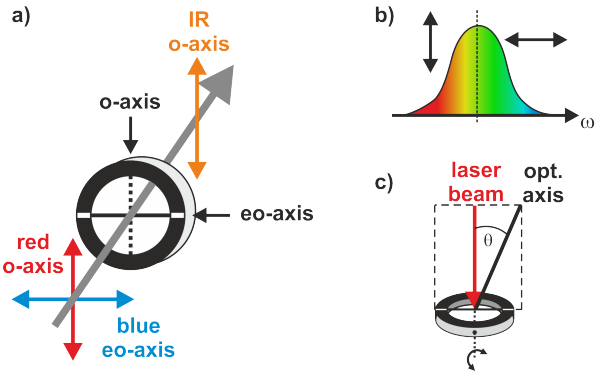

blue $[nm]$	red $[nm]$	IR $[\mu m]$	θ $LiIO_3$
700	900	3.2	20.9°
725	875	4.2	20.1°
740	855	5.5	20.1°

Figure 4.2: a) Polarization of the interacting frequencies with respect to the $LiIO_3$ crystal axis as derived from eq. (4.5). The generated IR light will be polarized parallel to the red frequencies of the spectrum as shown in b). b) The excitation spectrum is divided at its center frequency in a red and blue part with perpendicular polarizations as indicated. c) The crystal is cut at a phase-matching angle of $\theta = 20.1°$. Small adjustments are possible by rotation of the crystal. The table depicts three examples of DFG interactions, the generated IR wavelengths as well as the required angle for phase-matching. Usually the angle is highly dependent on the frequencies but in the special case of lithium-iodate, phase-matching can be achieved for a broad frequency region.

eq. (4.7) and shown in the table within fig. 4.2. Adjustments are possible by slightly rotating the crystal as indicated. The combination of the chosen crystal, the laser source and the right polarizations should allow to generate a broad IR-spectrum from about 3 to 8 µm. With the pulse shaper in place, it should be possible to control the generation of specific frequencies by changing the phases of the excitation frequencies.

4.2 Experimental Setup for Broadband IR Generation

The experimental setup for IR generation is shown in fig. 4.3. As before, the main parts are a 10 fs oscillator and a pulse shaper. Instead of a microscope, the beam is focused by $f = 10\,\text{cm}$ parabolic mirrors into the crystal and the laser frequencies are blocked by a germanium window (see fig. 4.3). Pre-compensation of the spectral phase by chirped mirrors is not required since there are no refractive objectives present. However, there still are some phase distortions due to other optical components like the polarizer or the shaper itself, that have to be corrected.

First experiments implementing an available MCT detector (mercury cadmium telluride, also HgCdTe) did not show any response to incident laser light or possibly generated IR frequencies. The problems could be identified to arise due to the high 80 MHz repetition rate of the applied femtosecond laser. To solve this, a small but very important modification of the setup was required. The detector and the associated amplifier are built for kHz systems and cannot follow a signal with MHz repetition rates. As a result, signal will be automatically averaged and appear as a DC output from the detector. Unfortunately, DC components are filtered out by the connected amplifier, leading to no measured signal at all. By introducing an optical chopper, however, a slower repetition rate is simulated. The amplifier detects a changing AC signal, which can then be directly measured.

In order to efficiently generate DFG signal, the participating excitational frequencies must overlap in space and time. While parabolic mirrors assure spatial overlap the temporal overlap is controlled with the shaper, which can be challenging if the correction phase is unknown. The usual approach to correct for phase distortions and assure a flat phase at the focus is based on the optimization of a feedback signal with an evolutionary algorithm [130, 131]. Both the SHG and the *nonresonant*

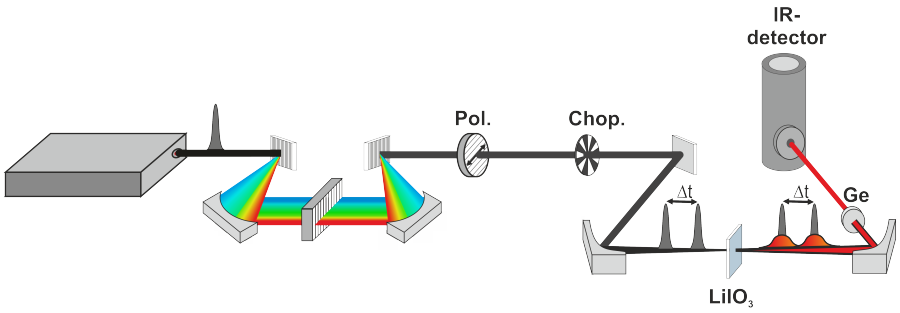

Figure 4.3: Single-beam setup for the generation of infrared light by focusing in a nonlinear DFG crystal. A polarizer (Pol.) enables amplitude shaping used for the generation of identical double-pulses but can be removed for other experiments. An optical chopper (Chop.) simulates a kHz repetition rate and thereby allows to use an MCT-detector and an associated amplifier, which is not suited for the measurement of MHz pulses. The broadband laser is focused in the crystal with an off-axis parabolic mirror ($f = 10\,\mathrm{cm}$) and then recollimated. Visible excitation light is blocked by a germanium window before detection. The case shown depicts the special case of an interferometric detection scheme (subsection 4.3.1). The polarizer enables amplitude shaping needed for the generation of identical double-pulses and should be removed for other experiments.

CARS signal scale with the pulse duration and are maximized for the shortest pulses. Because both signals are also generated in the nonlinear crystal, they can be used as feedback signal. By slowly rotating the crystal the SHG signal can even be seen by eye, which makes its detection comparatively easy (usually applying some negative chirp of about -200 to $-500\,\mathrm{fs}^2$ helps increasing the signal a lot already). If this does not work out a more complicated approach using the nonresonant CARS signal can be applied. By focusing the laser with a high-NA reflective objective onto the crystal, CARS signal will even be generated at comparatively high phase distortions and can be used for subsequent phase compression. Because the reflective objectives do not introduce additional phase distortions, the obtained correction phase can directly be used with the parabolic mirrors to generate IR signal afterwards. Once IR signal has been detected, phase compression becomes very simple since the IR itself can be used as feedback for the optimization algorithm.

4.3 Characterization of the Infrared Spectrum

The direct measurement of an IR spectrum requires an IR-spectrometer or a suitable monochromator and a single-channel detector sensitive in a broad spectral range in the IR region. Both components are expensive and have a limited spectral resolution. Another often applied method is the implementation of Fourier-transform detection, requiring only a single-channel detector. An frequently used alternative completely circumventing the need of IR detection is frequency upconversion [132]. By overlapping the generated IR pulse in a second nonlinear stage with the initial visible Ti:Sa laser in a SFG-crystal, the generated pulse is shifted to the visible region and can be analyzed with standard spectrometers. Because this approach is very complex and the intensities are not always sufficient for the generation of a second nonlinear signal, alternative methods for measuring IR spectra are highly needed. Besides the implementation of FT-IR measurements with a pulsed laser and a pulse shaper, a new method based on the spectral focusing approach as known from chapter 3 will be developed in the following.

4.3.1 Single-Beam Infrared Interferometry

Interferometric measurements are based on the analysis of an interference pattern generated by overlapping frequencies [133]. After splitting a laser into two identical beams, their relative phase difference can be controlled by changing the optical length of one of the arms with, e.g., a delay stage. Recombining the beams leads to an interference pattern that depends on the optical path difference. The signal can either be spectrally resolved or directly integrated by a single-channel detector. The optical spectrum of the beam is obtained by Fourier-transforming the interferogram to the frequency domain where the spectral resolution is only limited by the maximum path difference achievable. The implementation of interferometry with a pulse shaper has the advantage of intrinsic interferometric stability due to the collinear beam geometry (fig. 4.3). A double-pulse can be directly generated by the SLM without the need of an interferometer. The shaper allows to precisely control the relative time-delay with impressive accuracy. With this double-pulse common-path interferometer zeptosecond (10^{-21} s) precision pulse shaping measurements have been performed [134]. In the context of pulse characterization, double-pulses were used to implement

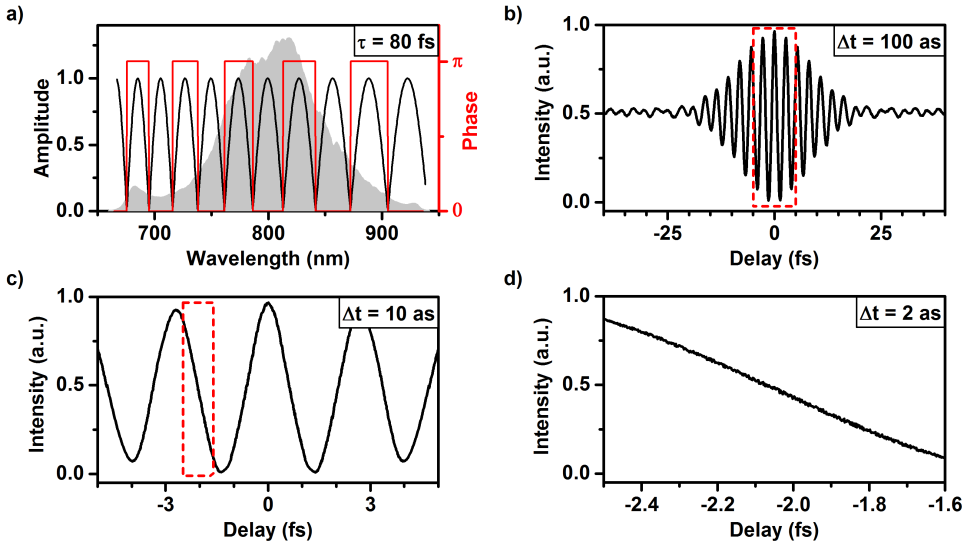

Figure 4.4: Single-beam interferometry. a) Amplitude and phase function for the generation of two identical double-pulses with a relative time-delay of 80 fs according to eq. (4.11). b) Interferogram detected with a photo diode directly after the shaper. Δt indicates the step size used for scanning. c) Interferogram of the region indicated in b). d) Interferogram of the region indicated in c) with a step size of only 2 as. The small variance of the data points highlights the achievable resolution, going down to zeptoseconds [134].

a shaper-assisted collinear version of SPIDER (SAC-SPIDER) [135, 136].

Generation of Identical Double-Pulses

An incoming electric field is directly controlled in the Fourier plane of the shaper by modulating the dispersed spectrum with an applied mask function $M(\omega)$ as discussed in section 2.3.2 and eq. (2.18). In the time domain a split and shifted electric field can be simply written as sum of two delayed fields. The Fourier shift theorem[a] states that a shift in the time domain leads to a linear phase change in the frequency domain,

[a] $E_{out}(\omega) = \mathcal{F}\{E_{out}(t-\tau)\} = e^{-i\omega\tau}\mathcal{F}\{E_{in}(t)\} = e^{-i\omega\tau}E_{in}(\omega)$

giving [134]

$$E_{out}(t) = \tfrac{1}{2}\Big[E_{in}(t-\tfrac{\tau}{2}) + E_{in}(t+\tfrac{\tau}{2})\Big] \tag{4.8}$$

$$E_{out}(\omega) = \tfrac{1}{2}\Big[e^{-i\omega\tau/2} + e^{i\omega\tau/2}\Big]\; E_{in}(\omega) \tag{4.9}$$

$$E_{out}(\omega) = \underbrace{\cos\left(\omega\tfrac{\tau}{2}\right)}_{M(\omega)}\; E_{in}(\omega) \tag{4.10}$$

$$M(\omega) = \underbrace{|\cos\left(\omega\tfrac{\tau}{2}\right)|}_{A}\; \exp\{i\cdot \underbrace{\arg[\cos(...)]}_{\phi=0 \text{ or } \pi}\}. \tag{4.11}$$

The derived mask functions can be directly applied with the shaper (fig. 4.4a) containing a polarizer for amplitude shaping. The frequency ω is given by the laser field whereas the time-delay τ can be chosen by the user. Recording the double-pulse interference directly after the pulse shaper with a photodiode reveals the incredible resolution achieved. The measurements were performed with time steps of only 10 as and confirm the results obtained by Koehler et al. [134].

Infrared Interferometry

The setup for IR generation by difference frequency generation (DFG) is kept as simple as possible, shown in fig. 4.3. By focusing the beam in the crystal, each of the double-pulses will generate an identical IR-signal. The relative time-delay of the generated IR-pulses can then be directly controlled by the delay of the excitation pulses. After blocking the laser light with a germanium window, a delay-scan allows to record an interferogram of the IR light. However, one has to pay attention to an important experimental detail. As has been shown in section 4.1.2, the interacting frequencies need to have perpendicular polarizations, where the blue frequencies are polarized parallel to the crystal axis. Because the generation of identical double-pulses is based on amplitude shaping (by going through a polarizer), all frequencies are linearly polarized after the pulse shaper. In order to still efficiently generate IR-signal, the crystal is rotated by 45° (angle of incidence still 0°). Half of the intensity of both pulses is thereby in parallel and the other half perpendicular to the crystal axis. Although achieving the best possible signal by this configuration, only a quarter of the initial IR intensity can be obtained due to the second-order nature of the DFG

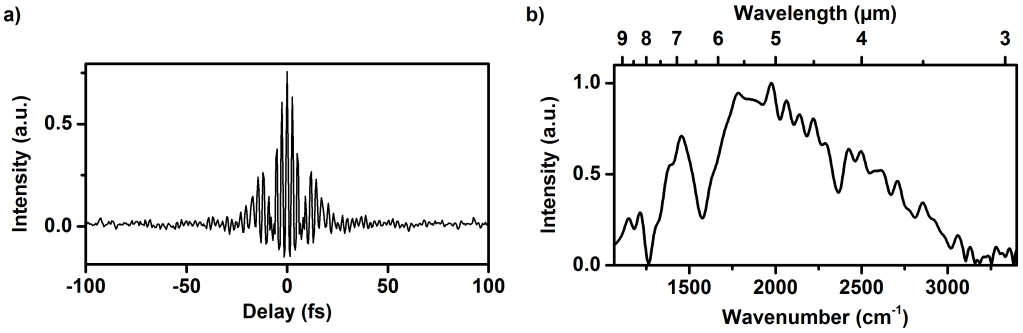

Figure 4.5: Single-beam double-pulse interferometric measurements of infrared light generated in a 0.1 mm $LiIO_3$ crystal. Fourier-transformation of the recorded interferogram in a) gives the IR spectrum shown in b).

process, $I = |\frac{1}{2}E_{max}|^2 = \frac{1}{4}I_{max}$. Fourier-transforming the raw data directly gives the infrared spectrum. An IR interferogram recorded with a MCT detector is depicted in fig. 4.5a. The data was simply corrected for an offset due to small background signal and then directly Fourier-transformed without additional windowing, resulting in the broad spectrum shown in fig. 4.5b, which correlates well with results from similar experiments in the literature [128]. In usual commercial continuous-wave FT-IR spectra the spectral resolution can be increased by increasing the scan range. Because the generated IR light here is pulsed, there exists a limited scan range where the pulses are sufficiently overlapped in time to produce enough signal. This can also be seen in the interferogram in fig. 4.5a. As soon as the temporal overlap of the pulses decreases, signal levels drop and are too small to resolve interferences above ca. 300 fs (not shown). The resolution is thus limited by the small scan range and leads to artifacts in the Fourier-transformed spectrum, that appear as a small wavelike variation of the signal in fig. 4.5b. Also, the small peaks above 8 µm are due to artifacts in the transformation and not due to actual generated light. The dips at around 1600 and 2600 cm^{-1} are due to absorption of the crystal itself.

4.3.2 Infrared Characterization by Spectral Focusing

Based on the recent developments of the single-beam spectral focusing approach, a new method for the characterization of the generated infrared spectrum can be readily implemented. By analogy with the pump-Stokes interaction in the CARS

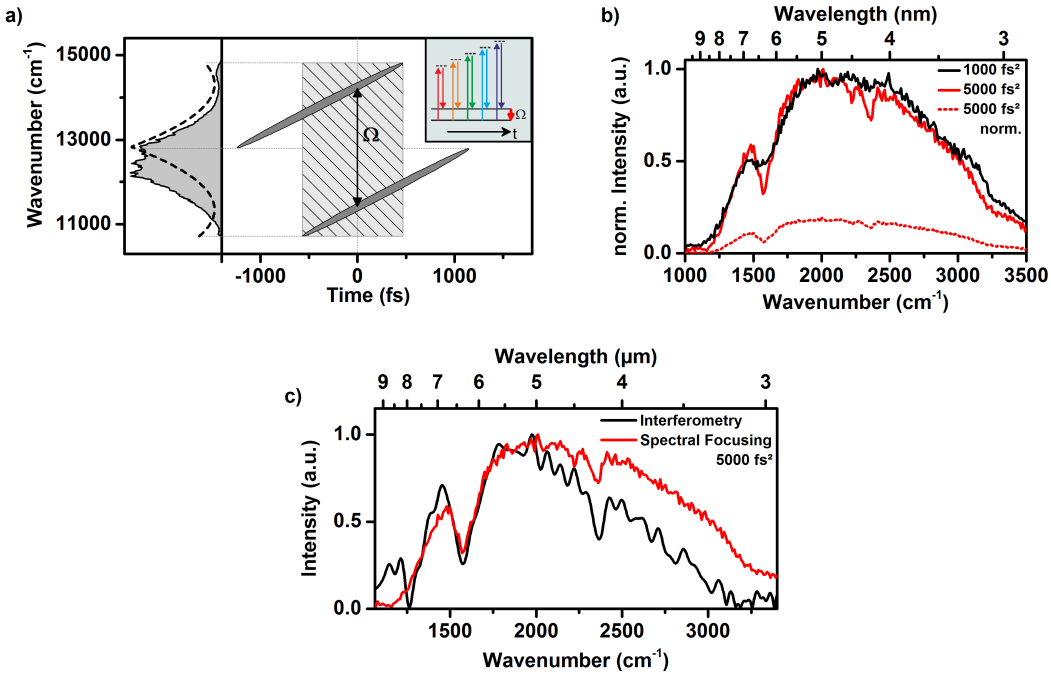

Figure 4.6: Characterization of an infrared spectrum based on the spectral focusing approach. a) Pump and Stokes frequencies are equally chirped, resulting in a constant frequency difference. Scanning this difference allows to collect an IR spectrum by recording the total signal at each Ω as depicted in b). b) Recorded spectra with a chirp of 1000 fs^2 (black) and 5000 fs^2 (red). Comparing the normalized spectra shows the enhanced spectral resolution at higher chirp. The spectrum shows the decrease in intensity in relation to the 1000 fs^2 spectrum. c) Comparison of the normalized spectra obtained with the interferometric and the spectral focusing approach.

process (fig. 3.4 or 4.6) the DFG process can be controlled in just the same way. By applying equal chirp to the interacting frequency regions, a constant instantaneous frequency difference (IFD) is created that selects the level to be probed in the CARS process, as explained in great detail in chapter 3. Application of the concept to DFG similarly allows to select a certain narrow frequency region to be generated. While a broad IR spectrum is generated with FTL pulses, spectral focusing enables tuning of the output frequencies to address specific processes or single vibrations by changing the phase function. By subsequent scanning of the IFD, a whole IR spectrum can be readily recorded.

In contrast to the interferometric approach where half of the laser power is not available for frequency conversion, the polarizations of pump and Stokes can be chosen

in accordance with the crystal axis to achieve the maximum possible signal. Fig. 4.6a again shows how pump and Stokes frequencies are chirped to achieve a constant IFD that leads to a narrow signal around a frequency Ω. Because the difference frequency is controlled directly, the total signal can be integrated and assigned to the applied IFD, which corresponds to the x-axis in fig. 4.6b. By scanning the IFD, an IR spectrum can be recorded. The spectral resolution is controlled in the same way as in spectral focusing, i.e. by the amount of chirp applied (section 3.4.6 and fig. 3.13). As can be seen in fig. 4.6b, a better spectral resolution is obtained for higher chirp (solid black & red lines) while the signal intensity drops (compare solid black to the dotted red line). A comparison of the spectra obtained with the interferometric and the spectral focusing approach (4.6c) shows distinct differences. Signal above 8 µm is due to artifacts from the Fourier-transformation as confirmed by spectra from the literature [128]. The intensity difference in the higher energy part of the spectrum can be due to several reasons. To generate light in this region, frequency components of the red and blue spectral wings are interacting. By the generation of double-pulses, the energy is roughly allocated 50/50 to both pulses. On top of that, only half of the energy of each pulse can be used for signal generation because the polarization must be chosen to lie between the ordinary and extraordinary axes. It is quite possible that the energy in the spectral wings is just not sufficient anymore to induce the DFG process. Thus, IR signal at higher energies is reduced. Another possibility is that the generation of the double pulses by phase and amplitude shaping leads to decreased intensity of the spectral wings (where higher phases are to be expected). This would have the same result as described above.

4.4 Single-Beam IR Absorption Spectroscopy

The in situ generated MIR spectrum can be directly applied for performing single-beam coherently controlled absorption spectroscopy. In accordance with the two presented approaches for spectral characterization, there are two ways to carry out the absorption experiments as well.

The first option is based on the double-pulse interference approach. The whole broadband IR-spectrum is generated and two interferograms are recorded, one with and one without a PET sample. The spectra obtained after the transformation are

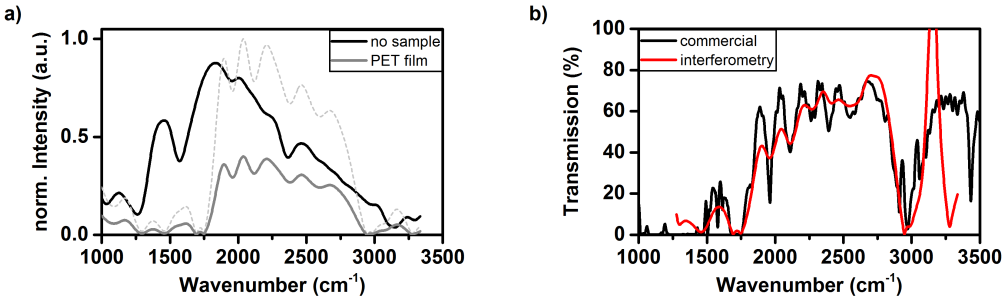

Figure 4.7: IR absorption spectroscopy based on interferometric measurement. a) IR spectrum with (gray) and without (black) PET sample. The spectrum after going through the PET sample (thin gray line) was rescaled by multiplication with a factor of 0.4 to be comparable to a commercial absorption spectrum in b). b) Comparison of the calculated transmission curves from the data in a) and a measurement performed with a commercial FT-IR spectrometer (PerkinElmer Spectrum 400).

depicted in fig. 4.7a. Because the absolute intensity of the two measurements was not correlated (i.e. more IR intensity present with sample as indicated by the thin gray line in fig. 4.7a), the spectrum after going through the PET sample was rescaled by multiplication with a factor of 0.4 (thick gray curve). This factor was chosen to achieve overlap of the obtained transmission curve $T = \frac{I_{PET}}{I_0}$ with a transmission curve recorded with a commercial FT-IR spectrometer (fig. 4.7b). The spectra taken with the single-beam interferometric approach and the commercial spectrometer are overlapping well. While the main characteristics of the sample are captured, the spectral resolution of the developed method is rather poor, as will be discussed in fig. 4.9. Also, distinct dips appearing in the spectrum recorded with the commercial spectrometer are not as pronounced in the generated spectrum. Nonetheless, it has to be emphasized that based on the in situ generation of a broadband MIR spectrum with a fs-laser and a pulse shaper, single-beam IR-absorption spectroscopy in a range from 1500 to 3000 cm^{-1} is enabled for the first time.

The second option for performing IR absorption spectroscopy is based on the spectral focusing approach presented in section 4.3.2. While a broad IR spectrum is generated with FTL pulses, spectral focusing enables to generate narrow frequency regions by applying equal chirp to the interacting spectral regions (fig. 4.6a). Subsequent point by point scanning of the constant frequency difference then covers the

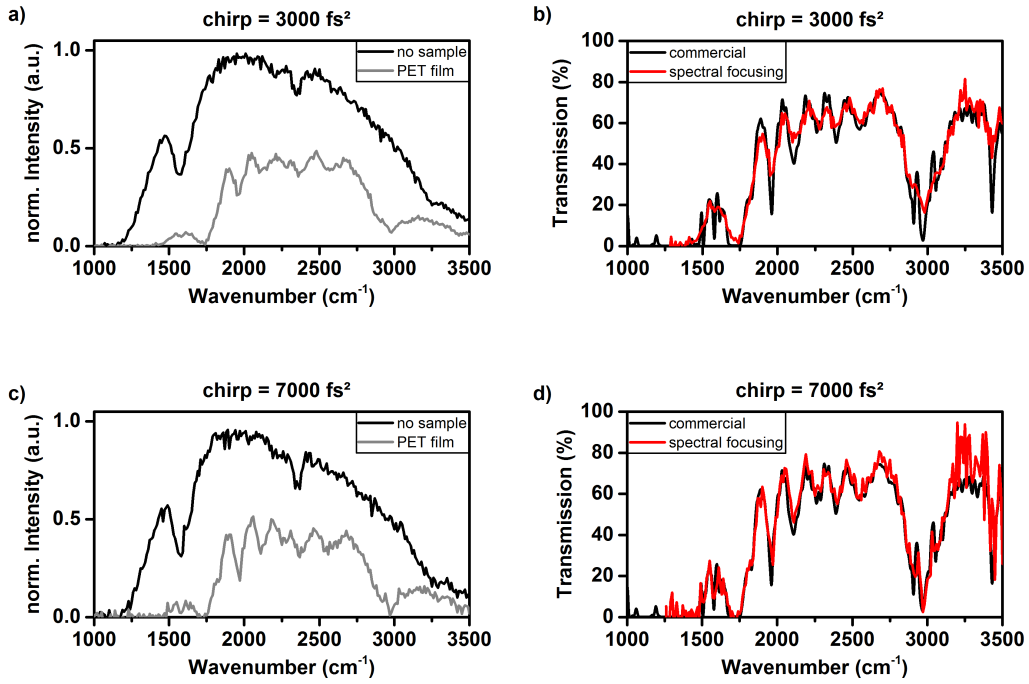

Figure 4.8: IR absorption spectroscopy based on a spectral focusing approach. a) & c) show the MIR spectra generated by the $LiIO_3$ crystal without (black) and with a thin PET film (gray) as sample. The spectra were generated by spectral focusing with 3000 fs^2 and 7000 fs^2, respectively. In b) & d) the calculated transmission spectra are compared to spectra recorded with a commercial FT-IR spectrometer (PerkinElmer Spectrum 400). Data below 1250 cm^{-1} was cut off (no IR light generated, see spectrum in a) or c)). The transmission data was multiplied by 1.3 for better overlap and easier comparison with the commercial data.

same spectrum as with an FTL pulse. The thereby obtained spectra without and with a thin PET film are depicted in fig. 4.8a & c. The higher chirp applied in fig. 4.8c results in a higher spectral resolution, i.e. the width of generated frequencies at each spectral point is narrower (the detailed explanations from fig. 3.13 can be directly transfered to the DFG process used here). Fig. 4.8b & d show the obtained transmission spectra. Data <1250 cm^{-1} has been cut off because no IR light is generated in this region, leading to artifacts in the transmission spectrum. Also, the transmission spectra were multiplied by 1.3 to be comparable to the ones recorded with the commercial spectrometer. The difference could be caused by the position of the sample. If the incident light is not perfectly perpendicular to the sample film, light

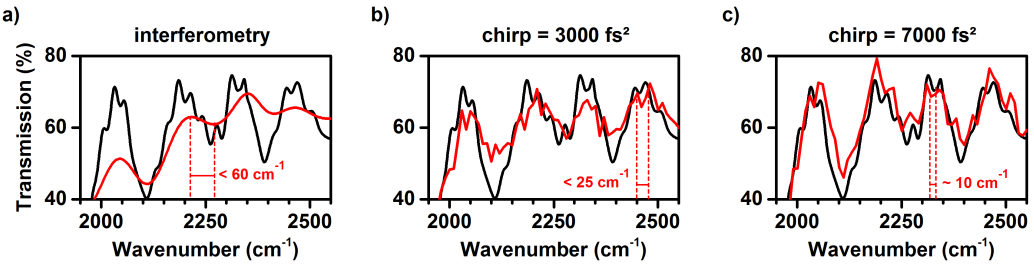

Figure 4.9: Estimation of the spectral resolution of different single-beam IR-absorption techniques. The pictures show enlarged areas of figs. 4.7b (a), 4.8b (b) and 4.8d (c). The measured (red) spectra are compared to a spectrum obtained with a commercially available spectrometer (PerkinElmer Spectrum 400) of the same PET sample. By comparing the characteristic structure it is possible to give an estimate of the achieved spectral resolution.

will be reflected directly from the surface, which leads to an offset in the transmission spectrum (I_0 becomes stronger compared to I_{PET} in $T = \frac{I_{PET}}{I_0}$). In the case of a chirp of 3000 fs^2 (fig. 4.8a) the spectral coverage is already greatly extended ranging from 1250 to about 3500 cm^{-1} when compared to the interferometric measurement in fig. 4.7. The characteristics of the sample are captured but, as in the case of the interferometric approach, the dips are not as pronounced. Increasing the spectral resolution by applying a chirp of 7000 fs^2 (fig. 4.8b) results in an almost perfect overlap of the obtained transmission spectrum with the one measured on a commercial spectrometer (fig. 4.8d). Not only the peaks and dips are pronounced very well, even small changes are resolved throughout the spectrum. The improvement in spectral resolution from the interferometric approach to spectral focusing with low and with higher chirp is highlighted in fig. 4.9. The figure shows a small region from the already discussed absorption spectra. The resolution of the commercial spectrometer was chosen to be 1 cm^{-1} in this measurement, which is higher than the width of expected absorption bands. It can therefore be used to give a rough estimation of the resolution of the presented techniques. In the interferometric approach small features are not resolved (fig. 4.9a). Only the large peaks and dips can be discriminated from one another, which are at a distance of about 60 cm^{-1}. The absorption spectrum recorded with spectral focusing depicted in fig. 4.9b already shows a drastic improvement in resolution. Even smaller peaks are resolved but seem to be slightly shifted to higher wavenumbers. As indicated, peaks with less than 25 cm^{-1} could be resolved.

As expected, the best spectral resolution is achieved when increasing the applied chirp. The obtained curve is almost identical to the reference spectrum where even the smallest peaks are resolved. Just at some points the peaks seems to be shifted to higher and sometimes to lower wavenumbers. However, this can be explained by the step size of the measurement, which was $10\,\mathrm{cm}^{-1}$. It is expected that a perfect overlap is achieved when smaller step sizes are used. Overall, the resolution can be roughly estimated to be in the order of the step size, i.e. around $10\,\mathrm{cm}^{-1}$

4.5 Summary

A tunable infrared light source based on a single 10 fs laser source and a pulse shaper was developed and successfully applied for IR absorption spectroscopy. Focusing the shaped femtosecond laser beam into a thin $LiIO_3$ nonlinear crystal enables difference-frequency generation (DFG). A broadband coherent infrared spectrum ranging from 2.8 to 8 µm (1250-3500 cm^{-1}) is generated. Pulse shaping does not only allow to compress the pulse in the focus for strong signal generation but to choose the polarization of the spectrum for optimal efficiency of the type-I DFG process. Simultaneous phase and amplitude shaping furthermore allows to generate identical double-pulses, which subsequently leads to the generation of two identical IR pulses. Thereby, scanning the time-delay of the double-pulses makes infrared interferometry readily available to characterize the generated IR spectrum with a single-channel detector. A more accurate and reliable method for the characterization of the generated spectrum was developed based on a spectral focusing approach (chapter 3). Implementation of the technique for the DFG process allows to control the generation of IR light. Narrow frequency regions can be flexibly generated to address a specific resonance or to scan through the IR spectrum. As a first example, infrared absorption spectroscopy was demonstrated on a PET film. While with the interferometric approach it is possible to follow the general characteristics of the sample, the poor spectral resolution prevent accurate measurements. With the spectral focusing technique, however, low noise and the possibility to tune the spectral resolution allows to record accurate transmission spectra. Transmission spectra recorded with a commercial available FT-IR spectrometer could be almost perfectly reproduced, suggesting spectral resolutions in the range of $10\,\mathrm{cm}^{-1}$.

With the tunable light source in the MIR spectral region at hand, many exciting new methods, measurements and approaches can be developed. While the spectral range can be expanded to reach the fingerprint region by using different nonlinear crystals, the direct application of the MIR light for IR and especially SFG microscopy is very promising. Also, the possibility of perform subsequent measurements of IR *and* Raman properties (through CARS) in the same setup just by changing the phase function presents a promising approach.

5 Rapid Multiplexing for Single-Beam CARS

In this chapter, a new technique for rapid phase rotation based on the characteristics of the liquid crystal mask in the pulse shaper is developed and demonstrated for multiplex single-beam CARS.

Within the context of multiplex single-beam CARS, the phase of a narrow frequency region acting as probe is changed to control the heterodyne interaction of a small resonant and a mostly nonresonant broad background signal. By subtracting certain spectra collected at different gate phases, it is possible to retrieve a Raman-like spectrum. Unfortunately, due to the relatively slow reordering of the liquid crystals, retrieving one Raman-like spectrum takes more than one second. After recapitulating the concept and characteristics of multiplex single-beam CARS in section 5.1, it will be shown how the 'slow' reordering of the liquid crystals can actually be turned into an advantage. A very fast phase scan technique is developed and its functionality tested on multiplex SB-CARS. The new approach allows to do a fast and continuous phase scan of more than 2π while spectrally resolving the generated signal. As will be shown in experiment, a Raman-like spectrum can thereby be obtained within a few milliseconds.

5.1 Background: Multiplex Single-Beam CARS

5.1.1 Concept

The general idea of multiplex CARS (M-CARS) is to combine broadband excitation with narrowband probing as already described in section 2.1.2 and fig. 2.2b. All resonances within the spectral width are excited simultaneously while a spectrally narrow probe pulse assures good spectral resolution. With M-CARS it is possible

to record a CARS spectrum in a single-shot measurement, paving the way for fast hyperspectral CARS imaging.

To further simplify the experimental setup and add yet another modality to the single-beam approach, multiplex-CARS has been implemented using one broadband laser and a pulse shaper [63, 67, 76, 108, 137]. The spectrum is subdivided into pump/Stokes regions for broadband excitation and a narrow gate selected to act as probe (as already briefly mentioned in fig. 1.4). The unspecific SB-CARS spectrum is dominated by strong nonresonant contributions due to the vast number of pump/Stokes interactions not coinciding with a vibrational level. While changing amplitude, phase or spectral position of the narrowband probing region has a small effect on this nonresonant background signal, it has an enormous influence on the resonant signal. Because the measured signal is a superposition of both parts, the resonant contributions are amplified by the strong nonresonant part (heterodyne measurement). Only when changing the probe phase, small but changing features on top of the huge nonresonant signal become visible (fig. 5.1b). Exploiting the different phase dependence of resonant and nonresonant contributions finally allows to retrieve a vibrational CARS and even a Raman-like spectrum [63, 66, 67, 76, 108, 137, 138].

5.1.2 Heterodyne Detection

The total optical signal is given by the light intensity on a detector, which corresponds to the squared modulus of the incident electric field, $\mathrm{S} = |\mathrm{E_{Sig}}|^2$. If the signal is superimposed with an external coherent electric field in the same spectral region, referred to as local oscillator (LO), the total intensity on the detector is [a]

$$I = |E_{Sig}(\omega) + E_{LO}(\omega)|^2 \tag{5.1}$$

$$= |E_{Sig}(\omega)|^2 + |E_{LO}(\omega)|^2 + 2|E_{Sig}(\omega)\ E_{LO}(\omega)|\ \ \cos\left(\Delta\phi(\omega)\right). \tag{5.2}$$

In addition to the phase-independent contributions from the signal and the LO, an interference term arises that depends on the relative phase between the signal and the LO electric field. As an external light source, the phase of the LO can easily be changed and allows to get rid of the phase-independent terms by subtracting

[a] complex number: $z = |z|e^{i\phi};\ z_1 z_2^* + z_1^* z_2 = |z_1 z_2|\left(e^{i(\phi_1-\phi_2)} + e^{-i(\phi 1-\phi_2)}\right) = |z_1 z_2| \cdot 2\ cos(\phi_1 - \phi_2)$

subsequent measurements with certain phase differences. The calculated signal will thus be proportional to the interference term only. In this heterodyne detection scheme, the calculated intensity now scales linearly with the signal field $E_{Sig}(\omega)$ which in return corresponds to a linear dependence on the concentration of scatterers in a CARS experiment (see eq. (2.6) and explanations thereof). In addition to enabling quantitative measurements due to the linear concentration dependence, overlapping a strong LO also results in an amplification of the weak signal [62, 139, 140].

A different heterodyne approach can be implemented in a single-beam setup without the need for an external LO [65, 109]. Instead of blocking the whole broadband laser before detection, the blue spectral wing is transmitted and used as *internal* LO overlapping with the generated signal. Because this blue wing is part of the laser spectrum, it is intrinsically phase-stable and its phase and amplitude can be controlled by pulse shaping. The LO phase and therefore the phase difference appearing in eq. (5.2) can be easily scanned. Additionally, if necessary its amplitude can be further reduced by placing a neutral density filter in the Fourier plane of the pulse shaper.

Another way to implement heterodyne detection in a single-beam setup is to use the huge background generated by broadband pulses as LO. While usually only the disadvantages and limiting factors of the nonresonant background are discussed, it can actually be used to the best advantage in this *self-heterodyne* approach [63, 67, 76, 137]. This concept is the basis of the approach described in the following section in more detail.

5.1.3 Phase Gate Interferometry

As already mentioned in the introduction of this chapter, the self-heterodyne approach can be exploited by introducing a phase shift in a narrow spectral window. A small intensity variation of the resonant signal is then amplified by the strong background signal acting as LO. A laser spectrum with an independently shaped narrow gate $E_g(\omega)$ can be described by superposition with the rest of the broad spectrum $E_b(\omega)$ as shown in fig. 5.1a [67, 75].

$$E(\omega) = E_b(\omega) + E_g\delta(\omega - \omega_g) \tag{5.3}$$

The gate has a certain spectral width that depends on the spectral width incident on each pixel and the number of pixels used as gate. Because the gate usually only consists of about 2 out of 640 illuminated pixels of the SLM, using a Dirac delta function to describe the spectral width of the gate is justified and simplifies calculations tremendously. For the generated CARS electric field it follows (eq. (2.14))

$$\begin{aligned} E_{CARS}(\omega) &= \int_0^\infty \mathrm{d}\Omega\; E(\omega-\Omega)\,\chi^{(3)}(\Omega)\,A(\Omega) \\ &= \int_0^\infty \mathrm{d}\Omega\; E_g\;\delta([\omega-\Omega]-\omega_g)\,\chi^{(3)}(\Omega)\,A(\Omega) \\ &\quad + \int_0^\infty \mathrm{d}\Omega\; E_b(\omega-\Omega)\,\chi^{(3)}(\Omega)\,A(\Omega) \\ &= \underbrace{E_g\cdot\chi^{(3)}(\omega-\omega_g)\,A(\omega-\omega_g)}_{E^{Sig}_{gate}(\omega)} + \underbrace{\int_0^\infty \mathrm{d}\Omega\; E_b(\omega-\Omega)\,\chi^{(3)}(\Omega)\,A(\Omega)}_{E_{LO}(\omega)} \end{aligned} \tag{5.4}$$

The generated field is composed of a signal field $E^{Sig}_{gate}(\omega)$ generated by the gate and the intense background $E_{LO}(\omega)$ generated by the rest of the broadband spectrum. Eq. (5.4) also shows that a phase change of the gate $E_g(\omega)$ (this is the part from the excitation laser) is directly transferred to the gate signal $E^{Sig}_{gate}(\omega)$ (this is the electric signal field *generated by* the gate). In the case presented, the background acts as static local oscillator, which does not depend on the phase of the gate. It is therefore possible to apply the knowledge and eqs. from the previous section, especially eq. (5.2) and write the total CARS signal in dependence of the gate phase as

$$S(\omega)_{\phi_g} = |E_{LO}(\omega)|^2 + |E^{Sig}_{gate}(\omega)|^2 + 2|E_{LO}(\omega)\;E^{Sig}_{gate}(\omega)|\;\;\cos\left(C+\phi_g\right). \tag{5.5}$$

Here, the phase difference is expressed by the unknown initial phases $C = \phi_{g,0} - \phi_{b,0}$ and the controllable gate phase ϕ_g. Because the phase of the gate signal is linearly dependent on the gate phase, the relative phase difference can be directly controlled and knowledge of the absolute phases is not needed. The obtained CARS signal of acetonitrile is depicted in fig. 5.1 for applied phase differences of $\phi_g = 0, \frac{1}{2}\pi, \pi, \frac{3}{2}\pi$. From these four measurements, double quadrature spectral interferometry (DQSI) can be applied [76, 141] to extract the phase and the amplitude of the signal field (eqs. (5.6) & (5.7), see appendix E). While the amplitude corresponds to a multiplex-CARS spectrum, taking the imaginary part of the signal (i.e. amplitude *and* phase)

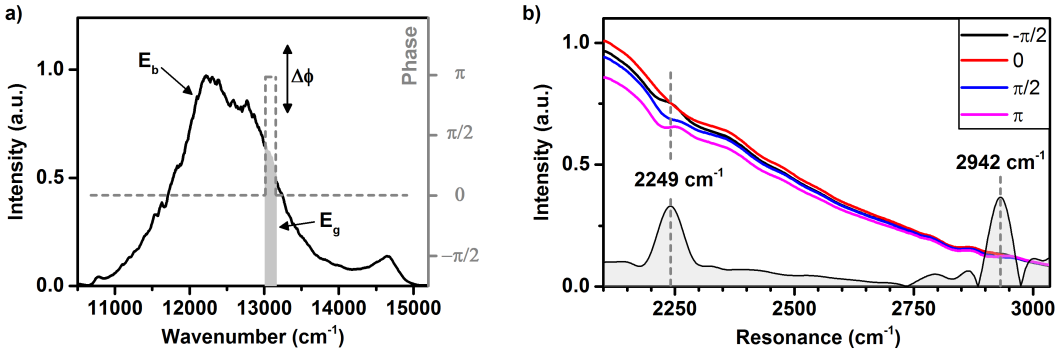

Figure 5.1: Extraction of Raman-like spectra of acetonitrile by multiplex SB-CARS spectroscopy [63, 67]. a) A narrow gate E_g is selected from the rest E_b of the broadband laser spectrum. The gate phase is controlled independently. b) Total signal measured when changing the gate phase by the indicated values. Performing DQSI calculation enables the extraction of phase and amplitude of the measured spectrum. Taking the imaginary part (gray) of the extracted signal finally gives the Raman-like spectrum. The resonances of acetonitrile are clearly visible at 2249 cm^{-1} & 2942 cm^{-1}, without distortions by dispersive lineshapes.

allows to extract a Raman-like spectrum (i.e. $E_{Raman} = \mathrm{Im}\{|E_g(\omega)| \cdot e^{i\phi}\}$). Because the extracted CARS field is still weighted with the Raman excitation probability (which highly depends on the resonance frequency in a single-beam approach, see black curve in fig. 2.3b), normalization is required as described in detail in [75, 76].

$$|E_g(\omega)| = \frac{1}{4|E_{LO}(\omega)|}\left[\left(S(\omega)_{\phi_g=0} - S(\omega)_{\phi_g=\pi}\right)^2 + \left(S(\omega)_{\phi_g=\frac{\pi}{2}} - S(\omega)_{\phi_g=-\frac{\pi}{2}}\right)^2\right]^{\frac{1}{2}} \tag{5.6}$$

$$\phi = \arctan\left[\frac{S(\omega)_{\phi_g=\frac{\pi}{2}} - S(\omega)_{\phi_g=-\frac{\pi}{2}}}{S(\omega)_{\phi_g=0} - S(\omega)_{\phi_g=\pi}}\right] \tag{5.7}$$

5.2 Rapid Multiplexing

In the previous section 5.1 it was explained how a Raman-like spectrum can be extracted from a multiplex CARS implementation in a single-beam setup. With the DQSI mathematical operations (appendix E) it was possible to calculate amplitude and phase of a resonant signal by measuring at different phase offsets of the gate. Unfortunately, the measurement is relatively time consuming because at least four

spectra at different gate phases have to be recorded to collect all necessary data. Even at short signal integration times and a small number of averages, waiting for the pulse shaper to apply the phases already takes about one second. Based on the work by A. Wipfler [67, 75, 76, 97], a new idea for a rapid multiplexing was developed. The goal is to perform all four measurements in a fraction of the time by continually measuring the CARS signal while scanning the phase of the gate (fig. 5.1a).

5.2.1 Concept of Rapid Phase Scan and Phase-Only Pulse Shaping

A phase is imprinted on the pulse by applying a certain voltage to the shaper (explained in detail in section 2.3.2) that is known from calibration measurements [80]. As long as the crystals are moving, the phase is continuously changing and only constant once the crystals have settled in their new orientation (fig. 5.2b). The idea behind the rapid multiplexing approach is to use the time window during the movement of the crystals and simultaneously record the generated time-resolved spectra as indicated in fig. 5.2a. A movement of the crystals and therefore a phase change is initiated as soon as a new voltage is applied to the pixel under consideration. In order to make use of the changing phase values between start and end, the phase has to be precisely determined at every moment in time. The simplest way to implement the idea would be with a phase-only pulse shaper containing only one liquid crystal mask. However, because a double-mask shaper (fig. 2.5a) is used in this work, the phase can only be precisely determined when the cells have settled in their final position. Different phases and polarization states are the result of a simultaneous movement of both cells, which makes precise or temporally resolved determination impossible. Phase-only pulse shaping can be implemented with a double-mask by deactivating one cell (apply maximum voltage, i.e. minimum and constant phase change) while rotating the laser polarization parallel to the extraordinary axis of the other cell (fig. 5.2b). When changing the applied voltage, the moving crystals will change their angle with respect to the incoming light, which solely results in a phase change as shown in fig. 5.2a.

The duration of the reorientation is highly dependent on the value of start and end voltages. Because the phase difference at any moment in time has to be known, a temporal calibration has to be performed once for every start/end voltage pair as

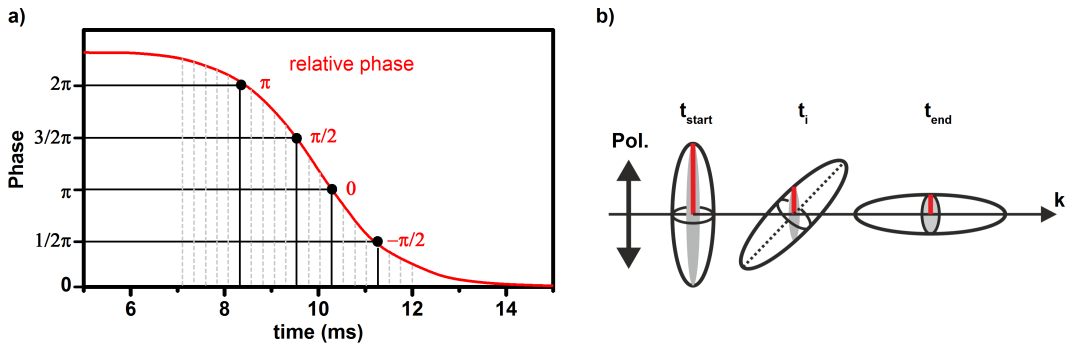

Figure 5.2: Principle of the rapid phase scan approach. a) Starting from a certain voltage, the red curve depicts the phase change of the gate spectral region initiated by applying a different voltage. A CCD camera is triggered to record the generated signals to capture the influence on the signal as indicated by the vertical lines. When the exact temporal change of the phase as well as the timing of the CCD camera are known, spectra with the right relative phase change can be chosen for the DQSI operation. b) This phase-only shaping scheme requires an incoming laser polarization parallel to the extraordinary axis of the liquid crystals. Applying a different voltage leads to reorientation, which is highly dependent on both start and end voltage.

explained in section 5.2.3. To be able to apply the DQSI functions, CARS spectra at four specific phase differences have to be recorded. Since the phase is constantly changing, the generated signal has to be measured simultaneously at short time intervals, indicated as dashed lines in fig. 5.2a. The time calibration allows to select the spectra corresponding to the desired phase changes.

5.2.2 Speeding Up the Detection

The goal of the presented approach is to measure Raman-like spectra in a SB-CARS setup as fast as possible. The shortest possible measurements achievable are limited by the duration of the phase scan, the minimum integration time of the camera as well as the signal intensity. As indicated by the dashed lines in fig. 5.2a, as many spectra as possible have to be measured during the phase scan in order to achieve a sufficient resolution to allow for an accurate assignment of the spectra to the continuously changing phase. A phase scan over more that 2π can be actually achieved within a few milliseconds (fig. 5.3b). The integration and read-out times of the CCD camera thus have to be in the millisecond or even microsecond regime, too. Because a full

read-out of the CCD ship is too slow, a special fast kinetics mode of the CCD camera (Andor Newton EMCCD, 200x1600 active pixels) is used. Within this mode, the chip is divided into a number of sub-areas. Charges generated by illumination of the first area are subsequently shifted to the next area, which can be used as temporary memory of the recorded signal (fig. 5.4a). While only the first area is illuminated, other areas must be protected from direct illumination or even stray light to not generate charges on the rest of the chip. Once the first signal is shifted in the form of charges on the CCD chip, the next signal can be collected again on the first area. After the integration time, charges from each sub-area will be again shifted down by one area. The chip is not read out until each sub-area carries information as depicted in fig. 5.4a. In this way, time consuming read-outs after each measurement are circumvented and the whole phase scan measurement speed increased significantly.

In the experiment, light was focused on the first sub-area (size usually 20x1600 or 10x1600 pixels) and prevented from illuminating other parts of the chip by a movable aluminum cover mounted directly in front of the CCD chip. Because the aluminum plate was not anodized (black) stray light could not completely be prevented from hitting the chip, leading to possible background signal that limits the sensitivity. After choosing the integration times according to the reorientation speed of the liquid crystals as known from the temporal calibration, the acquisition is triggered together with the shaper to achieve the best resolution at the shortest integration times. As will be shown in the following sections, spectra in intervals down to about 80 µs could be measured with sufficient signal intensity and resolution.

5.2.3 Temporal Calibration of the LC-mask

The principle of rapid multiplexing is to achieve a continuous and very fast phase change while simultaneously measuring the spectra. To perform subsequent DQSI calculations, the applied phase of the gate must be known for every measured spectrum, i.e. for every moment in time. To achieve this, a temporal calibration of the phase change has to be performed. Since the speed of the reorientation highly depends on the applied voltages [142], an individual calibration has to be performed for every start/end voltage pair. Fortunately, automation of the calibration is straightforward, which allows to take a full data set at many different voltage pairs in a single

measurement.

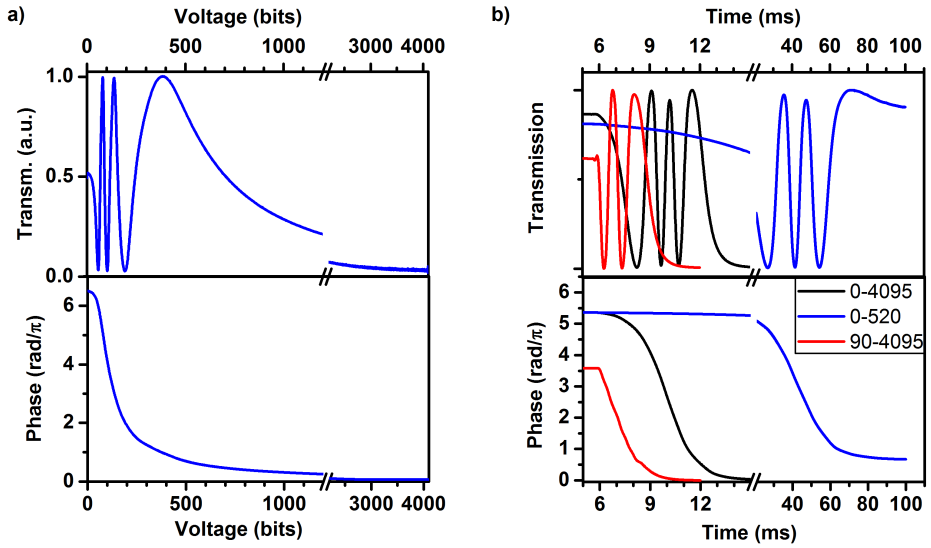

Figure 5.3: Voltage and temporal calibration curves of a liquid crystal mask. While scanning the first mask, the second mask is set at maximum voltage (minimum phase) to reduce its influence on the measurement. a) Voltage calibration: A voltage change leads to a change in polarization that is transformed into an amplitude pattern by a polarizer. A transmission change from one maximum to the next minimum corresponds to a rotation of the polarization by 90° and therefore a phase change of π. The obtained transmission curve can be converted into a phase change to give the final calibration curve of the mask for a specific wavelength (here He-Ne laser at 633 nm). b) Temporal calibration: Beginning with a certain start voltage, a different voltage is applied and the transmission measured in steps of 10 µs. The start-end voltages are indicated in the figure. The transmission curves and the calculated phase change reveal the dependence of the crystal reorientation on the absolute value of the voltages. The reorientation speed and the achievable phase change can thus be controlled by choosing the right voltages. The calibration curves were calculated for a gate wavelength of 758 nm. The maximum phase change (voltages: 0-4095 bits) is therefore smaller than for 633 nm as shown in a).

The temporal calibration is based on the usual phase vs. voltage calibration for liquid crystal masks. A He-Ne laser is sent through crossed polarizers with the SLM in between. Because the light travels in equal parts along the extraordinary and ordinary axis, an applied voltage leads to a phase change between these axes (see section 2.3.2). Overlapping the two waves results in a polarization change that can be measured after transformation into an amplitude change by the second polarizer. This transmission curve (fig. 5.3a) can then be converted into a phase change. While

measuring one mask, the second mask is kept constant to induce minimum and only static changes that do not alter the characteristics of the first mask. Once the phase dependence on the voltage is known for one wavelength it can be easily converted to any other wavelength [80].

This method can be adapted for the temporal calibration. Instead of measuring the transmission at every single voltage, only one final voltage is applied while simultaneously recording the time-resolved transmission curve. The transmission is measured by a fast photodiode in time intervals of 10 µs (fig. 5.3b) and can be transformed to give the phase change vs. time. Fig. 5.3b shows three examples with different start and end voltages. As expected, the reorientation time is highly dependent on the voltages applied and can vary between five and several hundred milliseconds (not shown). The measurements also give a good estimate of how long to wait for the full settlement of the crystals in normal 'static' experiments.

5.2.4 Results

Fig. 5.4 shows the time-resolved signal of acetonitrile as well as the obtained Raman-like spectra. The integration time of the signal appearing in each sub-area was 3 ms. The changes in the spectra due to the phase change of the gate are clearly visible in fig. 5.4b. By choosing spectra corresponding to the right phase differences as known from the temporal phase calibration, the DQSI operation can be performed. The extracted amplitude and phase information is depicted in fig. 5.4c together with the obtained Raman-like spectrum. The resonances of acetonitrile are clearly visible (dashed black lines).

The high signal intensities in fig. 5.4b allow to reduce the integration times even more, which requires an even faster scan of the gate phase. Choosing 90 and 4095 bits as start and end voltages, respectively, leads to an almost linear phase change in a short time window perfectly suited for the chosen integration time of just 76 µs. Fig. 5.5a depicts the phase change of the gate and the points in time where the spectra are taken (red lines). The intensity on the detector is still high enough to clearly see the change in the signal as induced by the gate (fig. 5.5b, dashed boxes). However, because of the overall decreased signal intensity stray light accumulating on the CCD

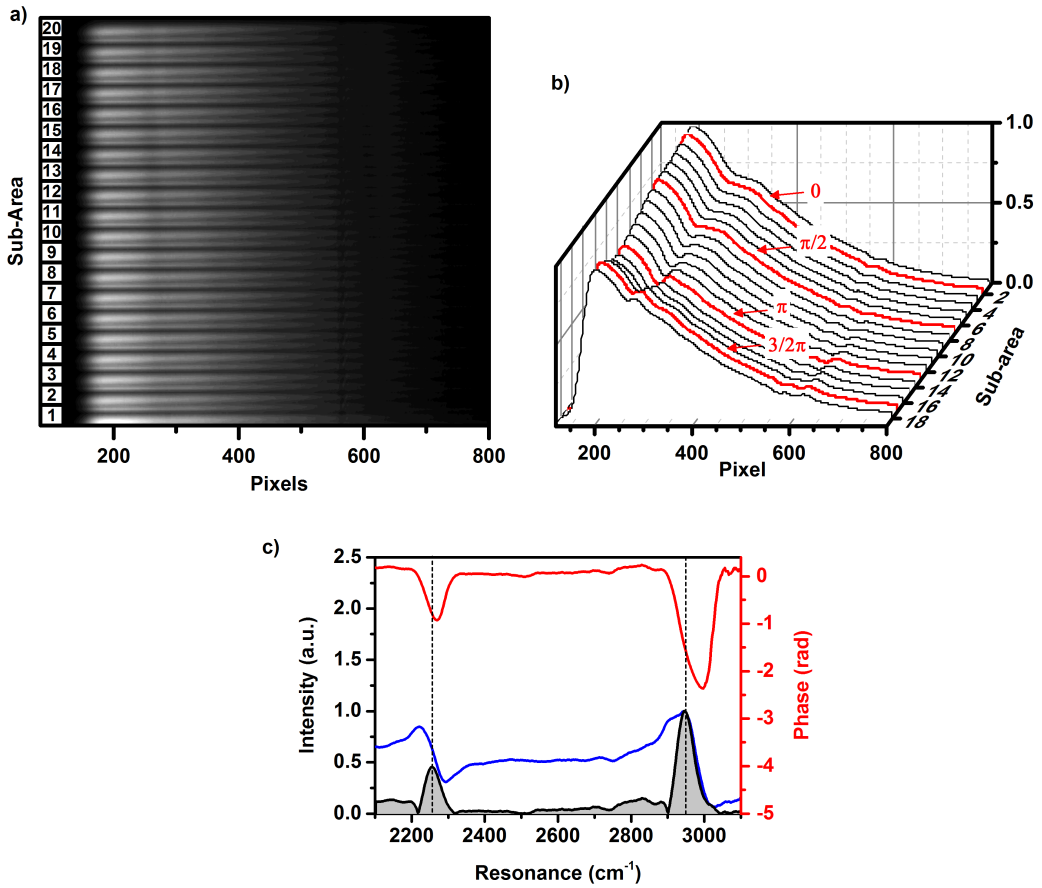

Figure 5.4: Extraction of Raman-like spectra of acetonitrile by the rapid multiplexing approach. The integration time of each spectra was 3 ms at start/end voltages of 120/330 bits. a) Total signal of the CCD chip after the read-out. The chip was divided into 20 sub-areas of 10 pixels height each. Only the top sub-area is illuminated and the signal passed on down to the next area acting as temporal memory. Thereby, reading out the chip in between is circumvented and very fast measurements become possible. b) shows the integrated signal from each sub-area. Overlapping signal from neighboring area as seen in a) was cut off. Because the first and last measurements show a slightly longer/shorter integration time they cannot be used and were deleted. With the known phase change over time, the right spectra can be chosen for the DQSI calculation. c) Extracted phase (red), amplitude (blue, corresponding to usual M-CARS spectrum) and the Raman-like spectrum (gray) showing the resonances of acetonitrile (dashed lines).

chip becomes more important and requires background correction before being able to apply the DQSI operations. THis background signal is also the reason for the offset of the subsequently measured spectra shown in fig. 5.5b. The experimental

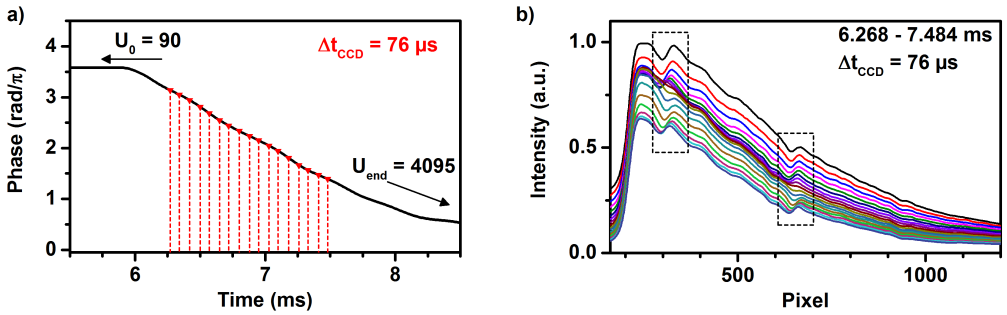

Figure 5.5: a) Temporal phase change for a start/end voltage pair of 90/4095 bits. For the measurement only the reorientation during the measurement period of the CCD camera is important. In order to achieve a good mapping of recorded spectra and the change of the gate phase, a linear phase change is desired. Signal is measured at moments in time as indicated by the red lines, which corresponds to a scanned phase of about 2π. b) CARS signal of acetonitrile measured at the points indicated in a). At the spectral positions in the dashed boxes the changing signal due to the changing gate phase is clearly visible. The offset of the signals is because of accumulation of stray light and has to be corrected for before analysis. The data in b) was slightly smoothed with a Savitzky-Golay filter (order 2, 15 side points).

data proofs the applicability of the concept down to integration times below 100 µs. Using an anodized (black) aluminum plate to cover the rest of the chip will result in drastic reduction of the stray light and will allow (eventually in combination with background subtraction methods) the extraction of Raman-like spectra.

5.2.5 Summary

In summary, a new technique for rapid phase rotation based on the characteristics of the liquid crystal mask in the pulse shaper was developed. By using the double liquid crystal mask as phase-only shaper, the reorientation of the crystals corresponds to a continuous phase change. The reorientation time and therefore the speed as well as the range of the phase change depends on the start and end voltages applied. A temporal calibration of the phase change allows to precisely predict the applied phase at every moment in time with microsecond resolution. The method was demonstrated for the extraction of Raman-like spectra in a multiplex single-beam CARS scheme. Using a special fast kinetics mode of the CCD camera, using the chip as temporal memory for recorded spectra, simultaneous phase change and recording was achieved down to an integration time of 76 µs. The possibility to retrieve Raman-like spectra

was shown on acetonitrile, whereas the applicability to the shortest integration time is momentarily only limited by stray background light. A better shielding of the chip from stray light and reflections should, however, allow for a measurement and automatic calculation based on the DQSI equations within about 2 ms (if only the measurement time is considered).

6 Pulse Compression by Sum-Frequency Generation

In this chapter, a new idea for the phase measurement and subsequent compression of an ultrashort pulse in the focus of a microscope will be presented. In contrast to most existing techniques, accurate measurement of the spectral phase is even possible in the weak spectral wings.

The most important prerequisite before performing experiments based on the control of a broadband spectrum with a pulse shaper is to assure the shortest pulses possible at the sample position. In this Fourier transform-limited case all frequencies arrive simultaneously, which corresponds to a constant flat phase throughout the spectrum. Only then, imprinting phase functions will result in the desired effects and enable advanced control experiments. Because most phase compression methods are based on the measurement of a broad nonlinear signal, intense frequencies have a higher influence on the feedback than the weak spectral wings. By reducing the ideas of coherent control to its simplest case, i.e. the interference of only two pathways that lead to the same target state, it is possible to overcome this limitation. By exploiting the phase dependence of the generated signal, it is possible to control an intense signal by a frequency with small intensity. This allows to not only compress the intense central part but also the weak wings of a broadband spectrum.

6.1 Pulse Compression in a Single-Beam Setup

Especially in femtosecond microscopy the high-NA objectives have a high effect on the temporal profile/spectral phase of the pulse. Static elements (e.g. grating or prism compressors) can compensate for high amounts of first-order chirp, whereas

femtosecond pulse shaping allows to compensate for higher-order dispersion, too. Because the working range of the shaper is limited, it is best to combine the approaches and precompensate for the chirp introduced by the objective and just use the shaper to correct for the remaining distortions in a fast and flexible fashion. In the present setup this is done by introducing negatively chirped mirrors with an adjustable number of bounces before the shaper (fig. 2.4 & appendix B).

There exist mainly two ways for the compensation of phase distortions. One option, also used throughout this thesis, can be used without knowledge of the phase. A nonlinear signal that scales with the pulse duration (SHG or *nonresonant* CARS) is generated in the focus and taken as feedback to be optimized in an evolutionary learning algorithm [130, 131]. Another option relies on the direct measurement of the spectral phase. By applying an inverted copy of the measured phase with the shaper, a flat phase is obtained and distortions are corrected for. The most common pulse characterization methods are autocorrelation measurements, frequency resolved optical gating (FROG) [143] or spectral interferometry for direct electric field reconstruction (SPIDER) [144]. All of the approaches can also be used in a collinear beam geometry and implemented with a pulse shaper [135, 136, 145, 146]. Another method referred to as multiphoton intrapulse interference (MIIPS) [147, 148] is actually directly based on the pulse shaper.

All of the above mentioned methods are based on the generation and subsequent analysis of nonlinear optical signals, typically SFG/SHG. Because the spectral profile usually follows a Gaussian shape, the central frequencies are naturally much more intense than the wings. Hence, small intensity changes due to improved phase compensation in the wings will get lost in the measurements because even very small phase changes around the central frequencies will have a much higher impact on the generated signal. The consequence is an unsatisfactory measurement and compensation of the phase in the spectral wings. While for many applications the wings play a minor role in the experiments, they can become very important in certain spectroscopy techniques. In single-beam CARS spectroscopy for example, the blue part of the spectrum can act as pump *and* probe and is therefore responsible for the blue-shift of the signal. The importance of the spectral wings becomes even clearer when considering the spectral focusing approach presented in chapter 3. When fo-

cusing on vibrations in the CH-region around $3000\,\mathrm{cm}^{-1}$, the wings are responsible for the excitation, while the central frequencies can only act as probe. In the context of this method, a perfect phase compensation even in the wings of the spectrum is therefore desired.

6.2 The Concept of SFG Pulse Compression

The concept of SFG pulse compression is based on the idea of coherent control. Narrow gates are cut out from the spectrum so that the same energy state can be reached by two different sum frequency combinations. Knowledge of the phase dependence of the interfering signal fields then allows to extract the phases of the generating laser frequencies in the focus of the microscope, enabling subsequent pulse compression.

In the experiment as well as the simulation, this is achieved by cutting out only three narrow frequency regions from the broadband spectrum (fig. 6.1, top). Focusing the shaped beam on a BBO crystal will generate sum-frequency signal at different spectral positions by all combinations of two interacting photons (fig. 6.1, bottom). Besides the SHG signal of each frequency, there are three possible SFG signals appearing. Due to the equal spacing of the excitation frequencies, two of the pathways lead to the same target state, which are $2\omega_0 = (\omega_0 - \Omega) + (\omega_0 + \Omega)$ and the SHG interaction of the central frequency $2\omega_0 = \omega_0 + \omega_0$. The electric fields will interfere to generate the central signal at $2\omega_0$ while all other signals do not show interfering pathways and are therefore independent of any phase changes. As depicted in the bottom part of fig. 6.1, a total of five spectrally separated signals is generated, in which only the central one can be controlled by changing the phase of one of the generating frequencies with a pulse shaper.

The SFG signal generation can be described in a general way by

$$S_{SFG}(2\omega_0) = \Big| \int_{-\infty}^{\infty} E\underbrace{(\omega_0 - \Omega)}_{-\Omega} E\underbrace{\omega_0 + \Omega)}_{\Omega}\, d\Omega \Big|^2. \tag{6.1}$$

$$= \Big| \int_{-\infty}^{\infty} |E_{-\Omega} E_{\Omega}|\ \cdot e^{i(\phi_{-\Omega} + \phi_{\Omega})} d\Omega \Big|^2 \tag{6.2}$$

$$= \Big| \int_{-\infty}^{\infty} A_{-\Omega\Omega}\ \cdot e^{i\phi_{-\Omega\Omega}} d\Omega \Big|^2 \tag{6.3}$$

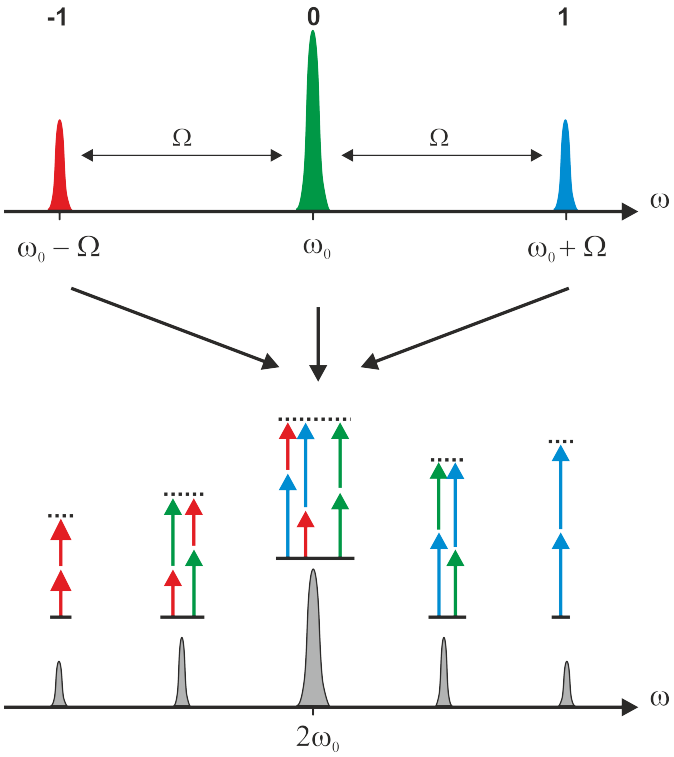

Figure 6.1: Excitation spectrum containing only three narrow frequency regions with equal energy spacing around ω_0. All possible energy schemes by mixing any two frequencies are shown below. Six signals are generated, whereas the SHG process from the central frequency and SFG from the wings lead to the same target state and signal interference. The total generated signal therefore depends on the relative phase difference between the two pathways.

Note that $A_{-\Omega\Omega}$ is the **product** of the amplitudes and $\phi_{-\Omega\Omega}$ is the **sum** of the phases of the two participating frequencies. SFG signal at $2\omega_0$ is generated by the interaction of *all* frequency pairs in a broadband spectrum that are centered around ω_0 as depicted in fig. 6.1. For the case of only three participating frequencies, the controllable signal generated at $2\omega_0$ is

$$S_{SFG}(2\omega_0) = \left| A_{-11} \cdot e^{i\phi_{-11}} + A_{00} \cdot e^{i\phi_{00}} + A_{1-1} \cdot e^{i\phi_{1-1}} \right|^2 \tag{6.4}$$

$$= \left| 2 \cdot A_{-11} \cdot e^{i\phi_{-11}} + A_{00} \cdot e^{i\phi_{00}} \right|^2 \tag{6.5}$$

$$\boxed{S_{SFG}(2\omega_0) = A_{00}^2 + 4A_{-11}^2 + 4A_{00}A_{-11} \cdot \cos[\phi_{00} - \phi_{-11}]}. \tag{6.6}$$

Eq. (6.6) reveals the dependence of the signal at the central frequency $2\omega_0$ on the phases of the incoming frequencies. While the amplitude terms represent a constant background, the mixing term is modulated when changing one of the phases. The equation also highlights the advantage of the method: if there are three frequencies with increasing intensity, $E_{-1} < E_0 < E_1$, the phase of the weakest one will still have a big influence on the signal since it is amplified by the most intense frequency as described by the term $A_{-11} = |E_{-1}E_1|$. The modulated signal will be maximized when the argument of the cosine equals 2π. When adding an additional phase $\Delta\phi$ with the pulse shaper to either ϕ_{-1} or ϕ_1 it follows for the maximum signal (applying $\pm\Delta\phi/2$ to both phases results in the same change)

$$\phi_{00} - (\phi_{-11} + \Delta\phi) = 2\pi n \tag{6.7}$$

$$\phi_1 = 2\phi_0 - \phi_{-1} - 2\pi n - \Delta\phi. \tag{6.8}$$

$\Delta\phi$ is the applied phase at which the maximum signal is generated.

To retrieve the phase of the pulse, the broadband spectrum is divided into many narrow gates while only three gates are set to transmission at a time by amplitude shaping (as shown in fig. 6.2). Thereby, the phase of one frequency can be scanned and, e.g. ϕ_1 can be calculated in dependence of the other phases as in eq. (6.8). The same procedure is then followed with other gate combinations to cover the whole spectrum. By measuring some gates twice in different combinations (compare figs. 6.2a & d), the obtained relations can be linked to one another and a set of linear equations is obtained. Because the temporal profile of the pulse is determined by the *relative* phase difference between the frequencies, the equations can be simplified by setting one phase arbitrarily as reference $\phi = 0$ (usually the central frequency $\phi_0 = 0$). A solution of the equations is obtained which now only depends on one phase. By applying the obtained function for different values of the missing phase, the maximum generated signal can be measured, which corresponds to the shortest possible pulse.

Fig. 6.2 depicts simulations of a phase scan for two gate combinations as indicated in fig. 6.2a & d. While all other kSHG and SFG signals are constant, only the central signal at around 450 nm is influenced upon changing the phase of one of the gates due to interference of two different pathways. As predicted by eq. (6.6), the signal

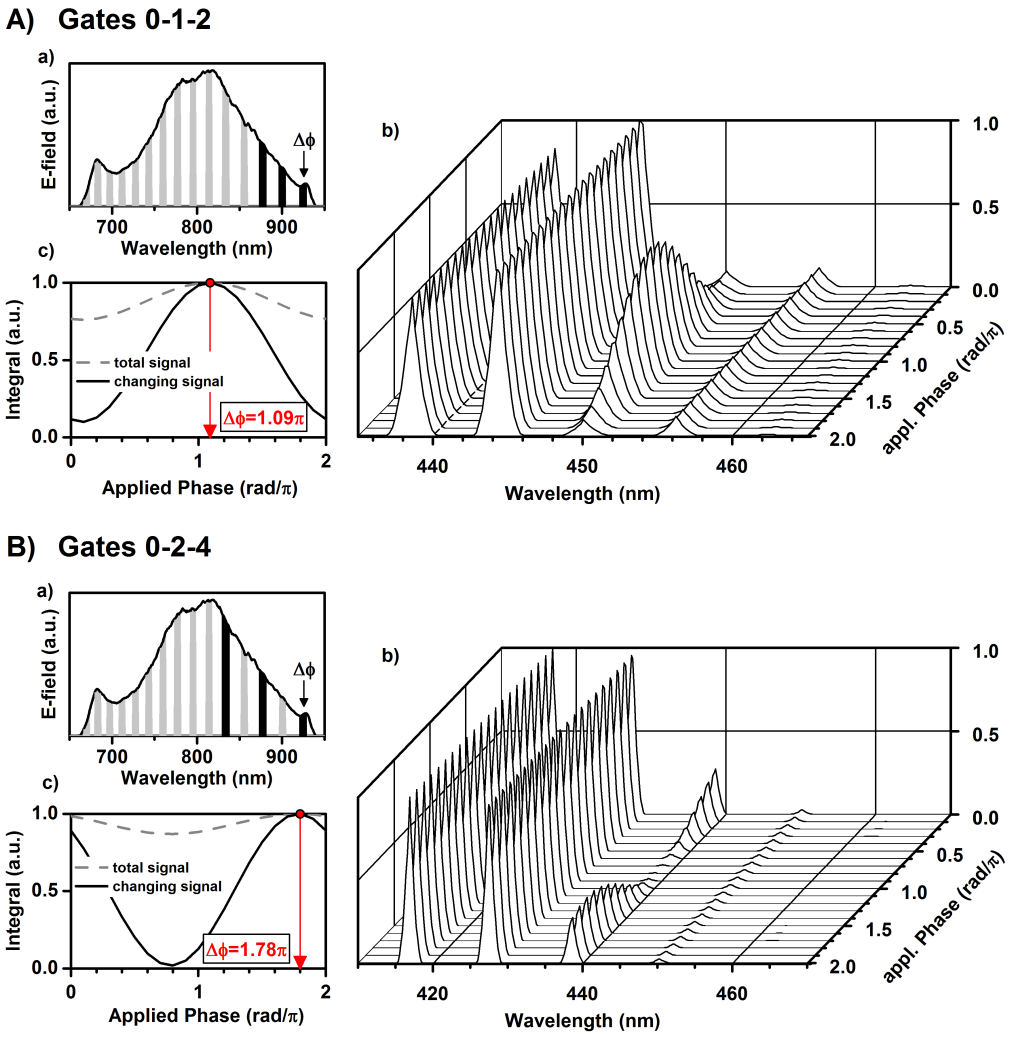

Figure 6.2: Simulations of SFG phase scans for two different gate combinations A) & B). a) The spectrum is divided into 15 equally spaced (on an energy scale) gates with equal width. The amplitude of the whole spectrum is set to zero except for the three indicated gates. Scanning the phase of the gate with the smallest amplitude leads to the SFG/SHG signal in b). The SFG signal is coherently controlled by the gate phase. c) shows the total integral of all contributions (dashed gray line) and when integrating only the phase-dependent SFG signal (solid black line). As expected (eq. (6.6)), the signal follows a cosine and the applied phase leading to the maximum signal can be extracted. The results from the extracted phase in A) are needed for subsequent calculations for phases in other gate combinations. In order to solve the resulting set of linear equations, some gates are measured several times in different combinations as shown in B).

follows a shifted cosine and the applied phase leading to the maximum signal can be extracted (eq. (6.8)). In fig. 6.2e the phase of the same gate is scanned for a different combination. While the SHG signal of the scanned gate (924 nm) at 462 nm cannot be seen anymore, the SFG signal is amplified due to interference with the intense field from the other gate. Still, the signal is controlled by the phase of the low-intensity gate, which emphasizes the advantages of the presented method. In the simulation a random phase was imprinted on the spectrum and an SFG phase at different gate combinations performed as described above. Following the linear set of equations obtained, the random phase could be retrieved and thereby corrected for (not shown because no new information would be obtained from the figure).

6.3 Experimental Results

For an efficient generation of SFG signal in the experiment, a BBO crystal was placed in the focus of the microscope. The generated signal was recorded with a standard optical spectrometer (Ocean Optics USB4000) after cutting off the laser light with an interference filter. The spectrum was divided into a number of energetically equally spaced gates as shown in fig. 6.3. For the sake of simplicity, only eight gates are shown while the maximum number of gates is only limited by the number of pixels. Different gate combinations were scanned in fig. 6.3A, B and C. As predicted by the equations and simulations in the previous section, the SFG signal (indicated by the black arrow) can be controlled by the gate phase in the experiment. A clear dependence of the signal intensity on the phase is obtained and, at a first glance, seems to follow a shifted cosine function. However, integrating the recorded signals reveals a changed period of the cosine. In contrast to the theoretical considerations, the cosine differs from the expected period of 2π. Consequently, extraction of the phase only leads to very inaccurate values and prevents the method from being used in the current setup. Also, apart from the considered SFG-signal, other signals are in some measurements changing their amplitude as indicated by the red arrow in fig. 6.3C. There are several possible explanations for the deviation:

(a) the applied phases differ from the defined phases

(b) a change of phase goes along with a change of amplitude

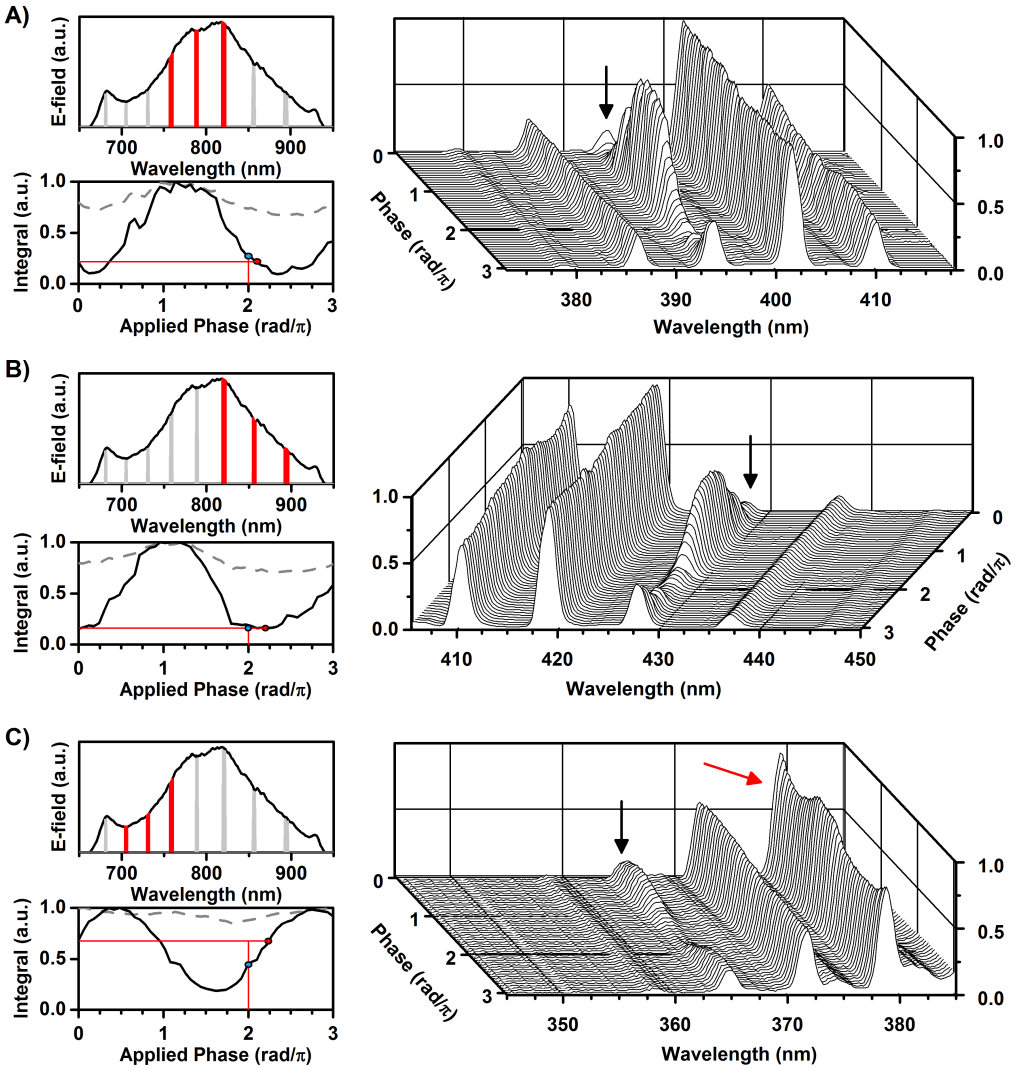

Figure 6.3: Experimental results of SFG phase scans. The graphs are explained in fig. 6.2. As expected from the simulations, the central signal can be controlled by changing the phase of a gate with small intensity. The integrated signal follows a shifted cosine. The period of the cosine, however, is slightly stretched and prevents direct extraction of the desired phase. The offset is increasing when the gate intensities are decreasing from A) to C). Due to decreased overall signal intensities in C), a relatively strong background signal is visible. Interferences with the background can lead to distortions of the cosine (see fig. 6.4 and corresponding explanations). As already seen in the SFG simulations, the SFG signal of a low and high intensity gate can be higher than the SHG signal of the strong gate because the SFG process is generated by two possible combinations while for SHG there is only one (fig. 6.1).

(c) insufficient amplitude modulation

(a) If the calibration is not accurate, there exists a deviation of the defined phase shift and the phase shift actually imprinted on the spectrum in the experiment. This would lead to a stretched or shrunk mapping of the phase (x-axis) in the graphs presented and account for the measured phase offset. However, the explanation is rather unlikely due to several reasons. For instance, several different calibrations were tested and the shaper and the calibration have been successfully applied throughout this thesis, where complicated phase functions led to the theoretically expected results (especially in the phase scan in chapter 5). On the other hand, there were always broad spectral regions interacting, even in chapter 5, and the phase change of single pixel was not as important as here, where already small deviations can be immediately seen. This leads to another possible explanation: potential crosstalk of the applied voltages of adjacent pixels has not been considered so far. Its effect is negligible when working with spectral regions of tens of pixels but can become important in the presented approach, where the gates are expanded over a few pixels only. Because at the pixels right next to the gates a very different voltage is applied to achieve amplitude shaping, the gate voltages can be influenced - an effect which is usually smoothed out by the size of chosen frequency regions. In either way, a resulting inaccuracy of the phase does not explain the amplitude change of the SHG signal and why the effect becomes larger with decreasing signal intensity (total signal intensity decreasing from A-C in fig. 6.3).

(b) Especially in fig. 6.3C a wavelike intensity change of the SHG signal generated by the scanned gate can be observed (red arrow). Since the phase of the gate does not have an influence on the SHG signal, the most straightforward explanation is given by a changing amplitude of the scanned gate. Because the modulated SFG signal (black arrow) naturally depends on the amplitude of the generating frequencies, the modulation will be determined by a mix of these two effects. This would lead to a stretched, shrunk or even a changing period of the SFG signal. As mentioned before, small changes of individual pixels would be smoothed out and not visible in normal measurements, where phases are usually applied to frequency regions spanning over tens or hundreds of pixels.

(c) A third explanation is given by a possibly insufficient amplitude modulation

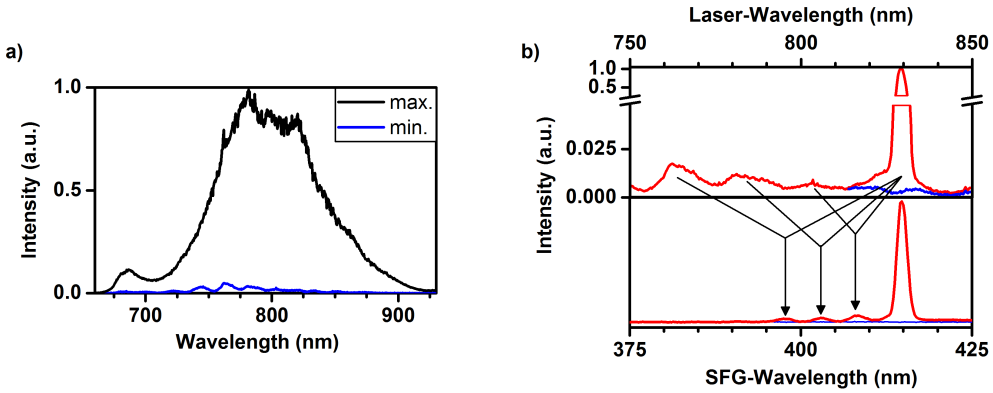

Figure 6.4: Insufficient amplitude modulation leads to background signal in the SFG experiments. a) Laser spectrum when the shaper is programmed for maximum (black) and for minimum transmission (blue). A small part of the spectrum is transmitted even in the minimum case. b) Zoomed in spectrum for minimum transmission (top panel, blue; as shown in a)) and when changing one gate to transmission (top panel, red). No SFG signal is generated for the minimum case (bottom panel, blue). The intense gate frequencies interact with the remaining laser light and lead to an amplification. The resulting SFG signal (bottom panel, red) at the corresponding sum-frequencies can lead to signal distortions and interferences in the performed measurements.

with the current SLM. Fig. 6.4a depicts the laser spectrum after the shaper when the mask is programmed for maximum (black) and minimum (blue) transmission. It can be seen that the spectrum is not completely blocked by the shaper. Further examination revealed that this effect is not due to an inaccurate calibration. The effect could be due to the small gaps between the pixels where phase and amplitude cannot be controlled. However, it is not clear why this would lead to a wavelike residual intensity distribution. In the experiment, the residual intensities are so small that it usually does not have any effect on measurements. With the settings from the measurements shown, not even an SFG spectrum could be measured (blue excitation and SFG-signal spectrum in fig. 6.4b). However, if setting one gate to transmission as shown by the red spectrum in the upper panel of fig. 6.4b the situation changes. The weak residual frequencies are amplified in the SFG process by the intense gate and become clearly visible in the SFG spectrum (fig. 6.4b, red curve lower panel). While here only one gate is shown, in the measurements there are three gates set to transmission and will therefore generate more background. For the analysis of the data it

is important to understand the effect of the gate phase change on this background. As is the desired signal dependent on the relative phase difference between the two interacting frequencies (eq. (6.6)), the same laws apply for interaction with residual frequencies generating background. This means that the background intensity will change with the phase scan and alter the modulation of the measured SFG signal (if generated at the same frequency). For strong signals this effect should play a minor role while for measuring the wings with less SFG intensity, these effects can have a stronger effect as confirmed by the experimental observations in fig. 6.3, especially subfigure C.

Altogether, the reason for the stretched period of the cosine in the experiment cannot be definitively identified at the current state. While explanation (a) is rather unlikely, either (b), (c), the pixel-crosstalk or even a combination of the three would explain the deviations.

6.4 Outlook

In order to solve the current problems, the underlying reasons have to be identified. Further experiments are needed to either be able to correct for the effects or suppress its generation in the first place. In order to do so several experiments can be conducted as explained in the following. In any case it should be excluded that the problems are not arising because of artifacts of this specific shaper by exchanging it with a different one.

A first approach that would benefit the whole setup is a spectral calibration of the mask. The usual approach, as briefly described in section 5.2.3, is to do the calibration with a HeNe-laser. The small spot of the laser only illuminates a few pixels. It is assumed that all pixels show exactly the same behavior so that the obtained calibration at 633 nm can not only be converted to different wavelengths but also to all pixels in the shaper. By using the broadband laser directly for the calibration, errors due to differences of pixels as well as small deviations from the underlying equation for the wavelength conversion could be minimized. All pixels would be illuminated simultaneously and the phase change of each pixel could be measured for each wavelength incident exactly on this pixel.

A second option would be to try to use the intensities of the other signals for normalization. When the scanned gate slightly changes its intensity, it can be seen in its SHG signal. Because the dependence on the generating amplitude is known from eq. (6.6), signal normalization should be possible. If this approach would account for the deviation from the expected cosine phase can, however not be predicted at the current state.

A third option is to repeat the experiments under new experimental conditions. As described in detail in appendix B, new chirped mirrors were implemented in the setup. At the time the presented measurements were performed, the chirped mirrors could not precompensate the chirp of the setup. A high remaining chirp was still present at the focus of the microscope and thus also during the measurements. Phase differences of 10π and more between the gates (depending on their spacing in the spectrum) might have corrupted the measurement. A chirp corresponds to a linear distribution of the frequencies in time. A strong remaining chirp would therefore correspond to a poor temporal overlap of the frequencies of the gates, which affects the measurement. With the new chirped mirrors, the present chirp can be almost completely compensated. The remaining distortions are within a span of 2π over the whole spectral range and effects due to reduced temporal overlap are eliminated.

Similarly, the SFG phase compensation method could be started with an already compressed phase. Since SHG/SFG signal is generated in the BBO crystal anyway, it will be advantageous to just run some cycles of an evolutionary pulse compression algorithm with the SHG signal as feedback. As a result, the phase will be reasonably well corrected, especially in the central part of the spectrum so that the new method can be directly applied afterwards to improve the compensation especially in the spectral wings. Because the first compression cycle does not have to be perfect, it can be stopped after as little as a 2-3 minutes.

One way to identify patterns in the deviation from the expected 2π-period of the cosine function (fig. 6.3) is to apply a known phase to a already compressed pulse with the shaper. The applied phase should hence be the result of the SFG phase measurements. In other words, the expected phase offset $\Delta\phi$ of each gate phase scan is known and can be used to identify patterns of deviations.

After eliminating the possibility of artifacts of the used pulse shaper, the presented

approaches should help to identify the underlying problems. Anyhow, if all the methods do not pay off and the small deviations cannot be resolved, e.g. because the problems are just intrinsic to the shaping with an liquid crystal mask, the idea mentioned in the last paragraph shows a way out of that. It allows to identify patterns of the deviations, which can be due to different reasons, and use them for correcting or normalizing the measured SFG signal. Because the deviations must be due to the setup or the shaper, they will be constant and only have to be measured once. Thus, considering how small the deviations are, a phase compression should be feasible when following the presented approaches. Anyhow, due to the much better correction of the phase at the focus with the new chirped mirrors, the deviations should now be even smaller, if still present at all.

Summary

The developments achieved within this thesis denote a big step forward towards the application of single-beam nonlinear microscopy for biomedical imaging. A considerable improvement of the generated nonlinear signal intensities enable their simultaneous detection for multimodal imaging. Additionally, new contrast mechanisms were established and are now available for microscopy applications that allow the discrimination of overlapping vibrational bands as well as their direct excitation by infrared light. In all avenues discussed in this thesis, the crucial parameter is the use and application of a femtosecond pulse shaper. The high degree of control over the spectral phase of a broadband pulse enables coherent control over different 2^{nd} and 3^{rd}-order nonlinear processes. With the shaper in place, a combination of fast, flexible spectroscopy with microscopic spectral and spatial resolution is achieved.

For nonlinear microscopy the CARS process is of particular importance due to its label-free three-dimensional contrast based on the vibrational motion of molecules. *Tailored spectral focusing* not only overcomes the drawbacks of broadband excitation but uses the spectral energy to its best advantage: the excitation of a single vibrational resonance by all available frequencies. In this thesis, especially the identification and individual shaping of frequencies acting solely as probe enabled a CARS signal increase of almost one order of magnitude. Simultaneously generated SHG and TPEF signals were boosted even more. As a result, the imaging of very complex biological samples with distinct and complementary contrast was achieved. The demonstration of contrast based on the vibrational coherence times of different energy levels adds a possibility for the discrimination of overlapping modes.

Vibrational motions are usually addressed via Raman-type interactions, like the CARS process. With an MIR light source at hand, however, the enhanced coupling between the field and molecular motions provided by direct excitation can be exploited for molecular spectroscopy. By transferring the ideas of spectral focusing to

the difference-frequency mixing process, a tunable broadband MIR light source was readily obtained. In first examples, characterization of the generated frequencies as well as the implementation of single-beam infrared absorption spectroscopy from 1250 to 3500 cm^{-1} was demonstrated. The narrow frequency regions generated can now be used to flexibly address specific resonances in future experiments.

Besides the investigation of single resonances, full spectra can be recorded in a single shot by implementing multiplex CARS spectroscopy. Taking four spectra at different phases of a narrow probing region allows to retrieve Raman-like spectra without background or dispersive lineshapes. In this thesis a novel rapid phase scan technique to overcome the slow switching speed inherent to liquid crystal masks was developed. By using the setup for phase-only shaping, fast and continuous phase scans of more than 2π could be carried out. The simultaneous acquisition of full CARS spectra on a μs-time scale allowed retrieving Raman-like spectra in only a few milliseconds. The method paves the way for rapid hyperspectral Raman-imaging in a single-beam CARS setup but can also be applied for any other experiment where a rapid phase scan is required.

The prerequisite for any successful shaping approach in the focus of a microscope is optimal pulse compression to guarantee a flat spectral phase. Unfortunately, most existing methods fail in sufficiently compressing the spectral wings, which are especially important for spectral focusing. To resolve this issue, a novel approach for the in situ phase measurement and subsequent compression was developed. Based on combined phase and amplitude shaping, the generation of a strong SFG signal can be controlled by a weak generating frequency. Overcoming the experimental challenges will enable accurate phase compression in a microscope focus even in the wings of a broadband spectrum.

The promising modalities developed during this thesis complement the versatile approach of coherently controlled nonlinear microscopy. Especially the progress made in tailored spectral focusing paves the way for future developments. For the first time, Raman and infrared vibrational properties can be investigated within the same setup, starting from just one broadband laser and a pulse shaper. Further exploring the potential arising from the achieved in situ generation of tunable MIR light will lead to exciting developments in the future.

Outlook: potential progress in future experiments

Based on the achievements presented in this work, many new experiments towards the development of additional contrast mechanisms are possible. In the following, some ideas based on the spectral focusing approach are presented. The explanations are based on the general time-frequency representation of the spectral focusing technique introduced in section 3.4.3 and fig. 3.10.

MIR and SFG microscopy: Besides IR-absorption spectroscopy, it is now possible to implement infrared microscopy by coupling the generated IR light into the microscope already present in the setup (fig. 2.4). Due to their limited transmission, standard refractive objectives have to be exchanged with reflective objectives. Detection of the transmitted light while scanning the sample in the focus of the microscope should allow to perform IR-microscopy straightaway. On top of that, the implementation of SFG microscopy should be feasible, too. Due to the collinear generation from a single beam, the IR light and the excitation laser light are intrinsically superimposed, as shown in fig. 6.1a. By independently adjusting the temporal overlap of the IR with the rest (i.e. frequencies not used for the IR generation) of the laser spectrum, the SFG process can be induced in a sample at the focal spot. The tight focusing of the visible frequencies leads to greatly increased spatial resolution of the SFG microscope compared to IR microscopy. In addition, the SFG signal is surface sensitive. Unfortunately, because of the weak IR light the SFG signal is expected to show small intensities as well. With the shaper in place it is, however, possible to implement a heterodyne detection scheme to boost the signal intensities. As depicted in fig. 6.1b, infrared light at $2850\,\mathrm{cm}^{-1}$ can be generated outside the microscope while independently shaping the visible frequencies for ideal temporal overlap in the

focus (green in fig. 6.1a & b). By choosing the right frequencies, SFG signal can be generated to spectrally overlap with the blue wing of the laser spectrum. Scanning of the phase of the blue wing enables to fully control the heterodyne measurements. It should actually be even possible to control the interference with the wing by changing the phase of the visible light (green). The concept should be flexibly applicable throughout the spectrum to address also lower lying energy levels. Increasing the IR intensity for efficient SFG generation will be an important challenge since the weak IR intensity is the bottleneck of the experiment.

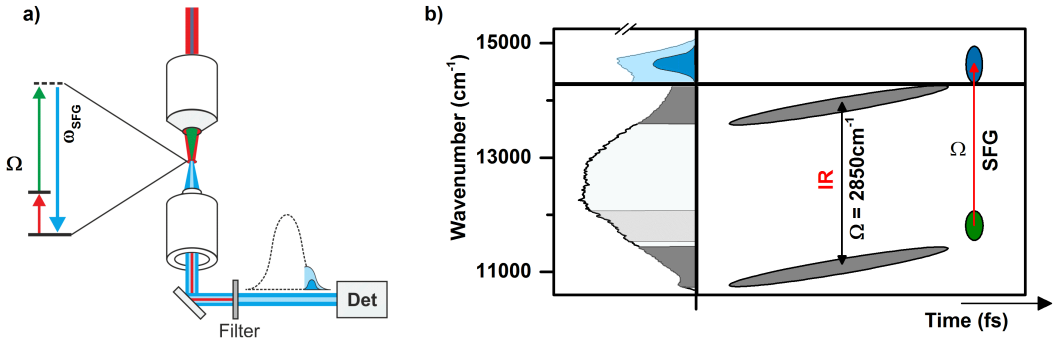

Figure 6.1: Approach for SFG microscopy with heterodyne detection. a) IR light is generated outside the microscope. By interaction with frequencies from the superimposed laser spectrum SFG signal can be generated in the focus. Spectral overlap with the blue wing enables heterodyne measurements. b) Time-frequency picture of the IR generation (gray) and its subsequent interaction with visible laser frequencies (green) generating SFG signal at the blue wing of the spectrum (blue wing and signal are orders of magnitude waeker than shown).

CARS imaging in the fingerprint region: A different application of heterodyne detection is spectral focusing CARS spectroscopy in the fingerprint region (see section 3.4.7), shown in fig. 6.2. Whereas CARS microscopy is mostly applied for imaging lipid-rich structures (because of the high Raman cross sections of CH-vibrations and the high density of lipids in biological tissue) signal intensities in the fingerprint region are usually too weak for imaging. As before, the pulse shaper allows to choose the position of the probing frequencies in a way to generate the CARS signal on top of the blue wing of the laser. Possible amplification by orders of magnitude and the linear signal dependence of heterodyne detection has the potential to

enable single-beam CARS microscopy in the fingerprint region.

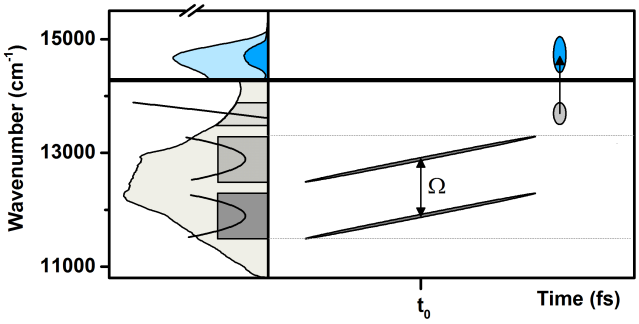

Figure 6.2: Implementation of spectral focusing heterodyne amplification of the usually very weak CARS signal in the fingerprint region. The probe frequencies are chosen such as to achieve overlap with the blue spectral wing of the spectrum, which can be controlled in amplitude and phase for optimum heterodyne detection.

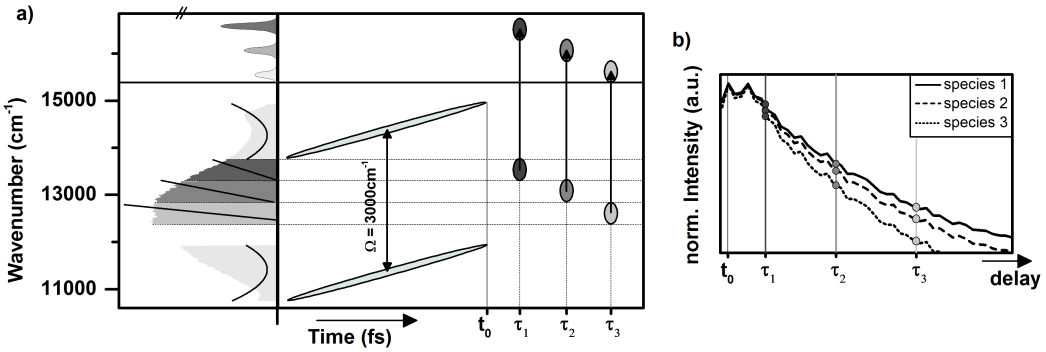

Figure 6.3: Coherence time imaging. a) The time-frequency picture shows the spectral regions of pump & Stokes (light gray) and three probe regions with different time delay as indicated by the phase functions (black lines). The decay of the coherence is probed at three different time-delays τ_1, τ_2&τ_3. b) Decay of the vibrational coherence of one vibration present in three different species/molecules. By probing at the time indicated in a), the molecules can be identified based on the signal ratios at the delays.

Coherence time imaging: In section 3.4.5 spectral focusing CARS with contrast based on different coherence times was achieved. While vibrational spectra can be usually easily discriminated by their fingerprint region, the peaks of CH-stretching vibrations are often overlapping, which can lead to a simultaneous excitation of different molecules. The proposed method of coherence time imaging represents a way to discriminate between molecules with spectrally overlapping signal solely based on their coherence properties! The idea is illustrated in fig. 6.3. Instead of scanning the probe delay to record the coherence decay as shown in fig. 6.3b, the broad probe is divided into three frequency regions. This allows to probe the coherence of a vibration (determined by spectral focusing, here $3000\,\mathrm{cm}^{-1}$) at three different time-delays simultaneously at a fixed phase function without scanning. A value specific for each coherence decay (for example in the form of $I(\tau_1) : I(\tau_2) : I(\tau_3)$) can be calculated from the integral of the three spectrally separated signals shown in fig. 6.3a. When collecting an image of a sample consisting of three different molecules, each with a resonance at $3000\,\mathrm{cm}^{-1}$, the coherence will be probed at the indicated points in each pixel. By assigning the measured values to the different molecules, it should be possible to differentiate the molecules from each other despite the overlapping vibration.

Spectral hyperfocusing: The idea of spectral hyperfocusing is presented in fig. 6.4. It can be applied to any of the spectral focusing approaches presented so far and could be particularly useful for increasing the IR intensity in the developed DFG approach. To achieve a high spectral resolution, a high chirp must be applied to pump and Stokes frequencies, dispersing them in time. As a result, the frequency difference addressing the vibrational level is very narrow and the coherence is built up over a long period of time. The new concept of spectral hyperfocusing is simple but effective. The pump and Stokes regions are divided into two parts. The same amount of positive and negative chirp is applied as shown in fig. 6.4 in blue and red, respectively. As indicated in the time frequency map, the same constant frequency difference is achieved for the positive and the negative chirp. Because of the changing frequency difference between blue and red ellipses, no significant excitation besides the desired resonance will be generated by other frequency interactions. The excitation energy that was dispersed over a longer time (gray ellipses in the background) is now incident on the sample in only half the time. This leads to a faster and stronger build-

up of the coherence and therefore to a stronger response when probing. Additionally, the maximum applicable chirp (before the Nyquist limit is reached, see appendix A for a detailed explanation) is greatly enhanced because the frequency regions are narrower. First simulations already showed a signal increase by a factor of two without optimization of any other parameters.

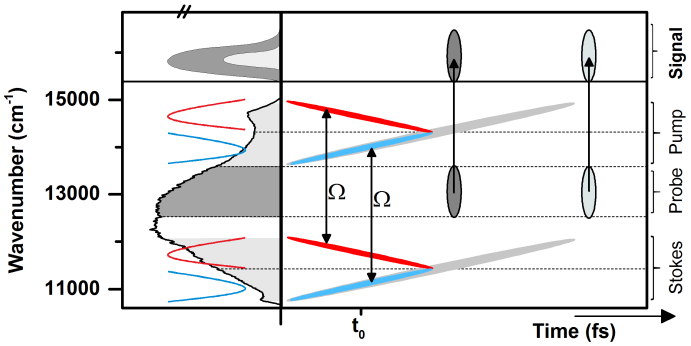

Figure 6.4: Approach for spectral hyperfocusing. Pump and Stokes regions are divided into two equal parts. A positive (blue) and a negative (red) chirp of equal magnitude is applied. As a result, the coherence is built up in half the time leading to a stronger response of the molecule and therefore to a stronger signal.

Altogether, especially the development of tailored spectral focusing opened a door for many new possibilities, some of which have been presented above. The suggested approaches of MIR and SFG microscopy, amplified CARS imaging in the fingerprint region, coherence time imaging and spectral hyperfocusing have the potential to investigate molecular properties not accessible with other methods. However, the future of the single-beam approach lies not only in the development of modalities and methods but actually in their application to important scientific and biomedical problems. The possibility to investigate complex samples by a multitude of approaches ranging from Raman to SHG, TPEF and even to IR measurements in one setup is a major advantage compared to other methods.

Appendices

A Maximum Shaping Range

The maximum possible phases that can be applied with the pulse shaper are limited by the Nyquist sampling theorem, which establishes a condition for the minimum sampling interval. In order to correctly describe a function, the sampling frequency must at least be twice as high as the highest frequency of the function. For a sine wave, for example, two data points must be known per period. In pulse shaping, the spectrum is spatially dispersed over a limited number of pixels. The desired phase can thus be only approximated in a step-wise fashion with a maximum slope limited by the Nyquist theorem: the phase change between two adjacent pixels must not exceed a value of π. The maximum applicable delay or chirp are therefore also limited by the pixilation. The more pixels per spectral region are available, the higher is the maximum applicable delay or phase. In the following, these limits are calculated for the setup as used throughout this thesis.

Delay

The expressions for the application of delay or chirp are known from the Taylor-expansion of the spectral phase (eq. (2.10)). The maximum delay can be calculated from the phase difference of two adjacent pixels (with $\phi_1 = a$).

$$\phi(\omega) = a\ (\omega - \omega_0) \tag{A.1}$$

$$\phi(\omega_i) = a\ (\omega_i - \omega_0) \tag{A.2}$$

$$\Delta\phi = \phi(\omega_{i+1}) - \phi(\omega_i) = a\ \Delta\omega\ \leq \pi \tag{A.3}$$

$$a_{max} = \frac{\pi}{\Delta\omega} \qquad \text{with} \quad \Delta\omega = (\omega_{i+1} - \omega_i) \tag{A.4}$$

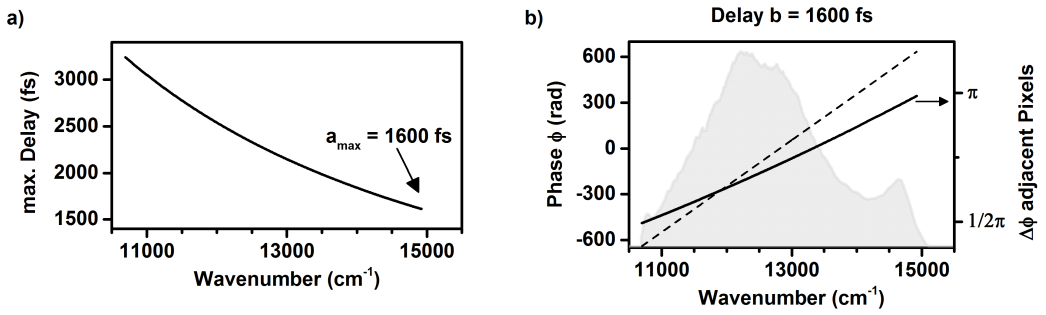

Figure A.1: Maximum possible delay applicable with the pulse shaper in the current setup. a) The maximum delay depends on the frequency difference of two adjacent pixels, which is changing over the mask. Therefore, the calculated max. delay is changing, too. b) Phase function for generating a delay of 1600 fs (dashed line) and the phase difference of adjacent pixels (solid line), which must not exceed a value of π.

Fig. A.1a shows the maximum possible delay a_{max} as calculated from eq. (A.4). Because the mapping of the frequencies on the pixels of the shaper is not linear, the frequency difference of adjacent pixels changes and thereby the maximum applicable delay. The smallest value shown in the figure fulfills the theoretical limit for each pair of neighboring pixels. In fig. A.1b, the calculated phase function for $b = 1600\,\mathrm{fs}$ (dashed line, left axis) and the phase difference of adjacent pixels (solid line, right axis) is depicted. As known from subfigure a), the maximum phase difference of π is reached in the region around $15\,000\,\mathrm{cm}^{-1}$. The maximum possible delay will be different for different regions of the spectrum and can change up to a factor of two. When the frequency difference of adjacent pixels is changing (which is the case when spatially separating the frequencies with an optical grating), reducing these limitations to a simple formula with a constant $\Delta\omega$ [36, 149] oversimplifies the actual behavior and can lead to false conclusions regarding the limitations. This becomes even more important when considering the maximum chirp.

Chirp

In the same way as shown above, the maximum possible chirp can be calculated from the phase difference of two adjacent pixels (eq. (2.10) with $\phi_2 = b$).

$$\phi(\omega) = \tfrac{1}{2}b\,(\omega - \omega_0)^2 \tag{A.5}$$

$$\phi(\omega_i) = \tfrac{1}{2}b\,(\omega_i - \omega_0)^2 \tag{A.6}$$

$$\Delta\phi(\omega_{i+1} - \omega_i) = \tfrac{1}{2}b\left[(\omega_{i+1} - \omega_0)^2 - (\omega_i - \omega_0)^2\right] \leq \pi \tag{A.7}$$

$$b_{max} = \frac{2\pi}{(\omega_{i+1} - \omega_0)^2 - (\omega_i - \omega_0)^2} \tag{A.8}$$

In contrast to the delay, possible values do not only depend on the frequency difference of adjacent pixels (i.e. ω_i & ω_{i+1}) but also on their distance from the central frequency ω_0. This fact is easy to understand when picturing the parabolic function applied to achieve chirp, as done in fig. A.2b. Since the slope of a parabola is constantly increasing, the phase jump from one pixel to the next will increase when going away from the central frequency. Fig. A.2a shows the maximum possible chirp that can theoretically be applied as calculated from eq. (A.8) at a center frequency $\omega_0 = 2413\,\mathrm{THz} \hat{=} 12\,821\,\mathrm{cm}^{-1} \hat{=} 780\,\mathrm{nm}$. Only when choosing a value of $4090\,\mathrm{fs}^2$ or below, the theorem is fulfilled throughout the spectrum. The negative sign arises from the definition of ω_0 in the equations and does not have to be considered here. Only the absolute value of the slope between pixels is important. Fig. A.2b again illustrates the corresponding phase function and phase difference of adjacent pixels. While $\Delta\phi$ reaches its limit in the blue wing of the spectrum, the phase difference in the red part is only $\frac{\pi}{4}$. As before, this is because of the changing difference frequency $\Delta\omega$ between pixels. This can be compensated for by changing the central frequency accordingly to $13\,514\,\mathrm{cm}^{-1}$ (fig. A.2c & d). The maximum applicable chirp is greatly increased to $6100\,\mathrm{fs}^2$.

However, in the context of spectral focusing (chapter 3) a chirp of more than $7000\,\mathrm{fs}^2$ was applied successfully, which seems to contradict the theoretical predictions made above. This again highlights the problems arising when oversimplifying the considerations about the shaping limitations. Calculating one value for the whole spectrum does not take the dependence on the spectral position and the distance

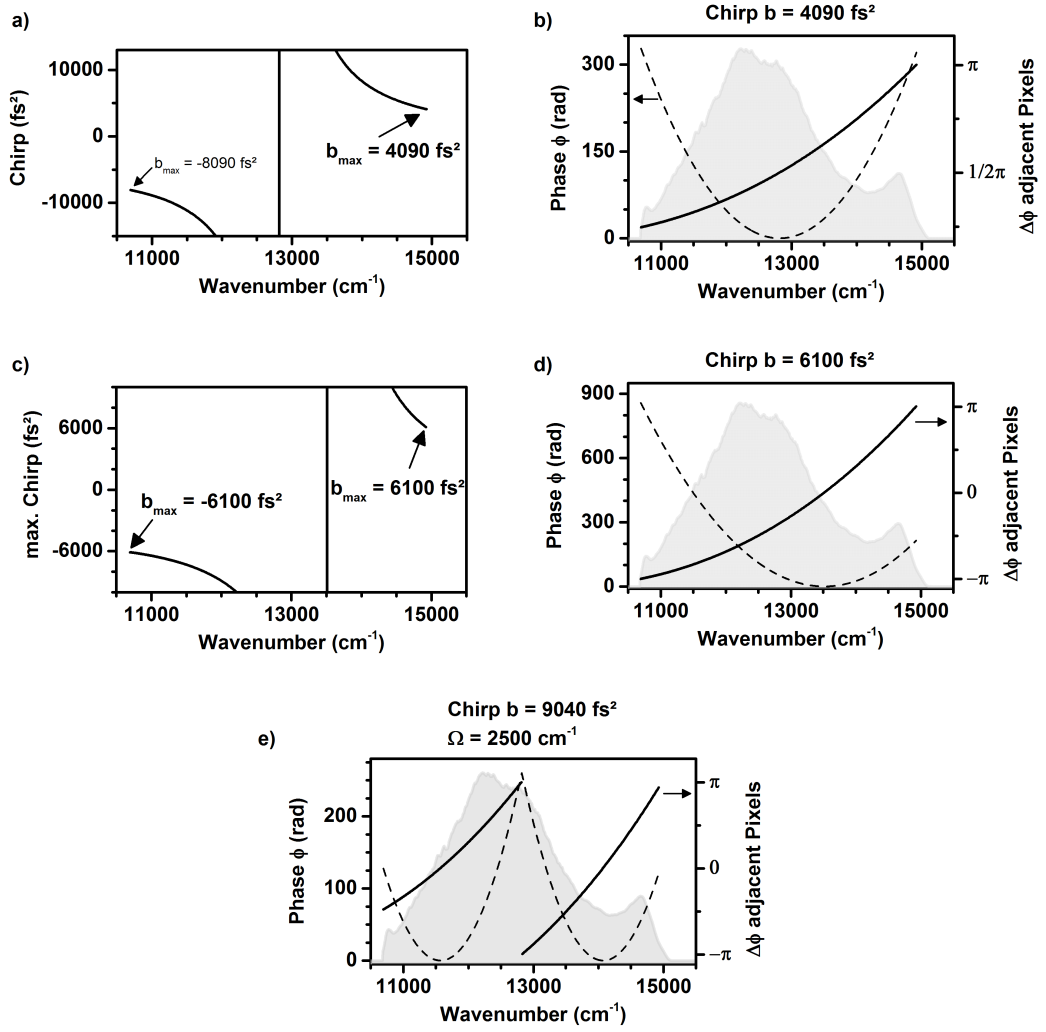

Figure A.2: Maximum possible chirp applicable with the pulse shaper in the current setup. a) The maximum chirp depends on the frequencies of two adjacent pixels as well as the central frequency. b) Phase function (dashed line) and phase difference of adjacent pixels (solid line) when chirping the pulse with a maximum of 4900 fs^2 (dashed line) obtained from a). the theoretical limit is only reached in the blue wing of the spectrum. c) Shifting the parabola allows to increase the applicable chirp. d) By centering the parabola around 740 nm ($\hat{=}13\,514\,\mathrm{cm}^{-1}$), the limit of a π phase-step is reached in both spectral wings by chirping with 6100 fs^2. e) Theoretical limits for spectral focusing with equal parabolas defined around 780 nm ($\hat{=}12\,821\,\mathrm{cm}^{-1}$). Due to the narrowed spectral regions covered by each parabola, higher chirp can be applied.

from the defined central frequency (eq. (A.8)) into account. In spectral focusing, two parabolas are applied to the spectrum in order to equally chirp the pump and Stokes frequencies. The spectral width covered by one parabola is therefore much smaller than in the case presented in fig. A.2, where the whole spectrum was considered. As a consequence, the maximum applicable chirp is increased as shown in fig. A.2e for spectral focusing with a distance of $2500\,\mathrm{cm}^{-1}$ defined around the center frequency $12\,821\,\mathrm{cm}^{-1}$. Accordingly, even higher chirp can be applied when narrowing the spectral region. In the case of spectral focusing in the fingerprint region with narrow pump and Stokes regions (fig. 3.15), a chirp of $15\,000\,\mathrm{fs}^2$ still was well within the limits.

B Chirped Mirrors

In order to use the pulse shaper to control the spectral phase of an ultrabroadband pulse in a microscope, phase distortions present in the focus have to be compensated. Especially when working with refractive objectives (which is usually the case), the optical components within lead to a strong dispersion of the pulse. Although the shaper could be used for phase correction, its actual function is to implement the ideas of coherent control. The working range of a pulse shaper is limited (see A) according to the Nyquist theorem, which states that the phase difference between each pixel must not exceed the theoretical value of π. If a high negative chirp is applied for phase correction, the working range of the shaper is limited even more, which can have a negative effect on the control experiments. Hence, it is best to correct strong phase distortions with static optical elements like prism compressors, grating compressors or negatively chirped mirrors (CM). Higher-order chirp and other remaining distortions can then still be corrected with the shaper.

As shown in fig. 2.4, negatively chirped mirrors were used to correct for the dispersion mainly introduced by the microscope objective. With the shaper in place, measuring the amount of chirp present in the focus is straightforward. Although due to other phase distortions the measurement is not perfectly accurate, the chirp is by far the most dominant distortion. The accuracy is therefore sufficient for an estimation of the number of required bounces on a CM pair. A microscope slide is used as sample to generate nonresonant CARS signal and the signal recorded while scanning the chirp with the pulse shaper. Maximum signal is achieved for the shortest pulses, which in return corresponds to the best phase correction. The top panel in fig. B.1a depicts the results of a chirp scan for CM previously used in the setup. Without the CM (0 bounces), a chirp of $2125\,\mathrm{fs}^2$ is present in the setup. As indicated in b), the mirrors can compensate for $-46\,\mathrm{fs}^2$ per bounce. To guarantee a good spot quality and prevent overlapping laser spots on the CM, no more than 13 bounces should be

used. This corresponds to a compensation of only 1196 fs^2 while the ramaining 929 fs^2 have to be corrected with the shaper. If introducing additional optical elements or a different objective, it can even become worse. Also, with a distance of 5 cm between the CM, a total number of 26 bounces results in an additional distance of 1.3 m the light has to travel before entering the shaper.

In order to allow for a full compensation of the dispersion, new CM (Thorlabs DCMP175) were implemented in the setup and characterized as explained above. The bottom panel in fig. B.1a, as well as the red curve in b) show the results of the chirp scan. With the new mirror pair, each bounce introduces a negative chirp of $-173\,fs^2$ and therefore allows to fully compensate the dispersion of the optical elements with only 7 bounces on each mirror. The results correlate well with the value of $-175\,fs^2$ given by the manufacturer.

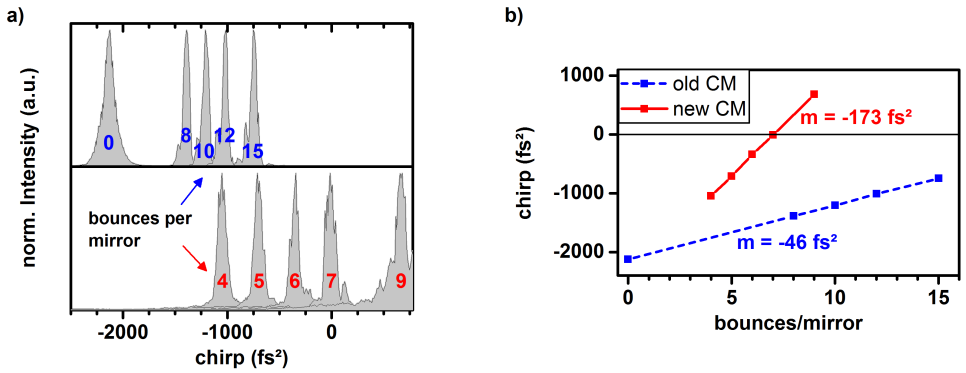

Figure B.1: Characterization of two different chirped mirror pairs by scanning the chirp parameter with the pulse shaper and recording the generated nonresonant CARS signal. a) Nonresonant CARS signal generated in dependence of the chirp applied with the shaper. The chirp compensation of the mirrors can be measured by changing the number of bounces. The maximum phase compensation is achieved at the maximum signals, which are transferred to the graph in b). In b) the slope gives the chirp compensation of the old (blue) and the new (red) mirror pair. Only with the new CM, the chirp can be fully compensated and allows the shaper to work at its full potential.

C Space-Time Coupling

The effect of space-time coupling can be directly shown in the experiment by measuring the beam displacement upon application of a temporal delay. A CCD camera is placed at about one meter distance from the second grating in the pulse shaper and different amounts of delay are applied, as shown in fig. C.1.

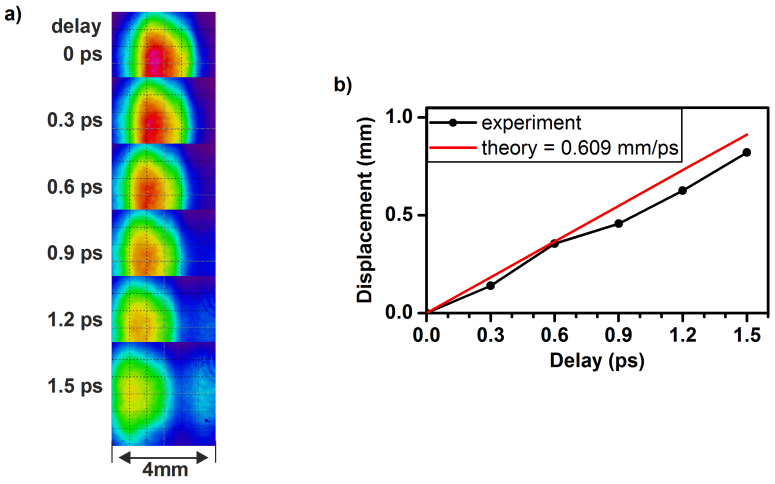

Figure C.1: Space-time coupling measurements. a) The laser spot is imaged on a CCD camera, which is placed behind the pulse shaper. The spot is shifted when applying a delay. b) Displacement of the laser spot for different delays as extracted from a). The experimental result (black) follows the theoretical prediction (red).

The expected spatial shift for a certain time-delay can be derived from theoretical considerations [82], as shown below. According to the derived space-time coupling constant $\frac{\Delta x}{\Delta t}$, the influence of space-time coupling is mainly determined by the grating parameters and cannot be circumvented by simply optimizing the experiment, as long as the optical components in the shaper remain the same.

$$\frac{\Delta x}{\Delta t} = \frac{\omega_0 \, G \cos(\alpha)}{2\pi \, m} = 0.609 \frac{\text{mm}}{\text{ps}}$$

ω_0	800 nm = 2354.56 THz
G	$(600/mm)^{-1}$
α	13°
m	1

ω_0 is the center frequency, G is the grating constant, α is the angle of incidence on the grating and m is the reflected order. For the values given in the table, a linear shift in space of 0.609 mm is expected when delaying the pulse by 1 ps as depicted in fig. C.1. Note that the beam displacement can lead to reduced intensity in the microscope focus (see also fig. 3.11) because parts from the laser beam will be prevented from entering the microscope objective. However, due to the tight focusing, the quality of the focal spot is not affected.

D Spectral Focusing in the Time-Picture

The electric field of an ultrashort pulse in the time domain can be described by

$$E(t) = |E(t)| \ \exp\left(i\left[\omega_0 t + \varphi(t)\right]\right). \tag{D.1}$$

If an equal chirp $\varphi(t) = \frac{1}{2}\beta t^2$ is introduced to the pump and the Stokes beam, where the latter is additionally delayed by Δt, the fields are

$$E_p(t,\beta) = |E_p(t,\beta)| \ \exp\left(i\left[\omega_p t + \tfrac{1}{2}\beta t^2\right]\right) \tag{D.2}$$

$$E_{St}(t+\Delta t,\beta) = |E_{St}(t+\Delta t,\beta)| \ \exp\left(i\left[\omega_{St}(t+\Delta t) + \tfrac{1}{2}\beta(t+\Delta t)^2\right]\right) \tag{D.3}$$

The coherence of a molecule in the CARS process is driven by the interaction of the pump and Stokes pulses $A(t)$. Using the definitions of the chirped and delayed electric fields of pump and Stokes shown above, the interaction is

$$A(t) = E_p(t) \cdot E^*_{St}(t) \quad \text{and substituting} \quad C = |E_p(t,\beta)||E_{St}(t+\Delta t,\beta)|. \tag{D.4}$$

$$A(t,\beta) = C \cdot \ \exp\left(i\left[\tfrac{1}{2}\beta(t^2 - \{t^2 + 2\Delta t\, t + \Delta t^2\}) + \omega_p t - \omega_{St} t - \omega_{St}\Delta t\right]\right) \tag{D.5}$$

$$A(t,\beta) = C \cdot \ \exp\left(i\left[-\beta\Delta t\, t - \tfrac{1}{2}\beta\Delta t^2 + \omega_p t - \omega_{St} t - \omega_{St}\Delta t\right]\right) \tag{D.6}$$

$$A(t,\beta) = C \cdot \ \exp\left(i\left[\{\omega_p - \omega_{St} - \beta\Delta t\}t - \left\{\omega_{St} + \tfrac{1}{2}\beta\Delta t\right\}\Delta t\right]\right) \tag{D.7}$$

The right term can be dropped because it affects both the resonant and nonresonant part in the same way by adding an identical phase term [94]. When omitting these constant amplitude and phase factors, the pump-Stokes convolution becomes

$$A(t,\beta) \propto \exp\big(i[\underbrace{\omega_p - \omega_{St} - \beta\Delta t}_{\Omega}]t\big). \tag{D.8}$$

E Double Quadrature Spectral Interferometry

The phase of the narrowband signal in eq. (5.4) consists of the unknown initial phase $\phi_{g,0}$ and the known controllable gate phase ϕ_g. The phase difference can therefore be written as a constant and the changing gate phase as

$$\Delta\phi(\omega) = (\phi_{g,0} + \phi_g) - \phi_{b,0} = C + \phi_g \tag{E.1}$$

$$C = \phi_{g,0} - \phi_{b,0} \tag{E.2}$$

The measured signals in dependence of the gate phase are therefore

$$S(\omega)_{\phi_g=0} = |E_{LO}(\omega)|^2 + |E^{Sig}_{gate}(\omega)|^2 + 2|E_{LO}(\omega)\ E^{Sig}_{gate}(\omega)|\ \cos\left(C + 0\right) \tag{E.3}$$

$$S(\omega)_{\phi_g=\pi} = |E_{LO}(\omega)|^2 + |E^{Sig}_{gate}(\omega)|^2 + 2|E_{LO}(\omega)\ E^{Sig}_{gate}(\omega)|\ \cos\left(C + \pi\right) \tag{E.4}$$

$$S(\omega)_{\phi_g=\frac{\pi}{2}} = |E_{LO}(\omega)|^2 + |E^{Sig}_{gate}(\omega)|^2 + 2|E_{LO}(\omega)\ E^{Sig}_{gate}(\omega)|\ \underbrace{\cos\left(C + \tfrac{\pi}{2}\right)}_{-\sin(C)} \tag{E.5}$$

$$S(\omega)_{\phi_g=-\frac{\pi}{2}} = |E_{LO}(\omega)|^2 + |E^{Sig}_{gate}(\omega)|^2 + 2|E_{LO}(\omega)\ E^{Sig}_{gate}(\omega)|\ \underbrace{\cos\left(C - \tfrac{\pi}{2}\right)}_{\sin(C)} \tag{E.6}$$

Subtraction of the signals with a phase difference of π gives

$$S(\omega)_{\phi_g=0} - S(\omega)_{\phi_g=\pi} = 4|E_{LO}(\omega)\ E^{Sig}_{gate}(\omega)|\ \cos\left(C\right) \tag{E.7}$$

$$S(\omega)_{\phi_g=\frac{\pi}{2}} - S(\omega)_{\phi_g=-\frac{\pi}{2}} = -4|E_{LO}(\omega)\ E^{Sig}_{gate}(\omega)|\ \sin\left(C\right) \tag{E.8}$$

$$|E_g(\omega)| = \frac{1}{4|E_{LO}(\omega)|}\left[\left(S(\omega)_{\phi_g=0} - S(\omega)_{\phi_g=\pi}\right)^2 + \left(S(\omega)_{\phi_g=\frac{\pi}{2}} - S(\omega)_{\phi_g=-\frac{\pi}{2}}\right)^2\right]^{\frac{1}{2}} \tag{E.9}$$

$$\phi_{b,0} - \phi_{g,0} = \arctan\left[\frac{S(\omega)_{\phi_g=\frac{\pi}{2}} - S(\omega)_{\phi_g=-\frac{\pi}{2}}}{S(\omega)_{\phi_g=0} - S(\omega)_{\phi_g=\pi}}\right] \tag{E.10}$$

References

[1] E. Betzig, "Proposed method for molecular optical imaging", Opt. Lett. **20**, 237 (1995).

[2] E. Betzig, G. H. Patterson, R. Sougrat, O. W. Lindwasser, S. Olenych, J. S. Bonifacino, M. W. Davidson, J. Lippincott-Schwartz, and H. F. Hess, "Imaging Intracellular Fluorescent Proteins at Nanometer Resolution", Science **313**, 1642 (2006).

[3] W. E. Moerner, and L. Kador, "Optical detection and spectroscopy of single molecules in a solid", Phys. Rev. Lett. **62**, 2535 (1989).

[4] R. M. Dickson, A. B. Cubitt, R. Y. Tsien, and W. E. Moerner, "On/off blinking and switching behaviour of single molecules of green fluorescent protein", Nature **388**, 355 (1997).

[5] S. W. Hell, and J. Wichmann, "Breaking the diffraction resolution limit by stimulated emission: stimulated-emission-depletion fluorescence microscopy", Opt. Lett. **19**, 780 (1994).

[6] T. A. Klar, S. Jakobs, M. Dyba, A. Egner, and S. W. Hell, "Fluorescence microscopy with diffraction resolution barrier broken by stimulated emission", Proc. Natl. Acad. Sci. USA **97**, 8206 (2000).

[7] E. E. Hoover, and J. A. Squier, "Advances in multiphoton microscopy technology", Nat. Photonics **7**, 93 (2013).

[8] W. Denk, J. H. Strickler, and W. W. Webb, "Two-photon laser scanning fluorescence microscopy", Science **248**, 73 (1990).

[9] W. R. Zipfel, R. M. Williams, and W. W. Webb, "Nonlinear magic: multiphoton microscopy in the biosciences", Nat. Biotechnol. **21**, 1369 (2003).

[10] F. Helmchen, and W. Denk, "Deep tissue two-photon microscopy", Nat. Methods **2**, 932 (2005).

[11] W. Min, C. W. Freudiger, S. Lu, and X. S. Xie, "Coherent nonlinear optical imaging: beyond fluorescence microscopy", Annu. Rev. Phys. Chem. **62**, 507 (2011).

[12] J. L. Suhalim, J. C. Boik, B. J. Tromberg, and E. O. Potma, "The need for speed", J. Biophotonics **5**, 387 (2012).

[13] C.-Y. Chung, J. Boik, and E. O. Potma, "Biomolecular imaging with coherent nonlinear vibrational microscopy", Annu. Rev. Phys. Chem. **64**, 77 (2013).

[14] M. J. Winterhalder, and A. Zumbusch, "Nonlinear optical microscopy with vibrational contrast", J. Microsc. **255**, 1 (2014).

[15] C. L. Evans, E. O. Potma, M. Puoris' haag, D. Côté, C. P. Lin, and X. S. Xie, "Chemical imaging of tissue in vivo with video-rate coherent anti-Stokes Raman scattering microscopy", Proc. Natl. Acad. Sci. USA **102**, 16807 (2005).

[16] J.-X. Cheng, and X. S. Xie, "Vibrational spectroscopic imaging of living systems: An emerging platform for biology and medicine", Science **350**, aaa8870 (2015).

[17] A. Alfonso-García, R. Mittal, E. S. Lee, and E. O. Potma, "Biological imaging with coherent Raman scattering microscopy: a tutorial", J. Biomed. Opt. **19**, 071407 (2014).

[18] M. Fleischmann, P. Hendra, and A. McQuillan, "Raman spectra of pyridine adsorbed at a silver electrode", Chem. Phys. Lett. **26**, 163 (1974).

[19] S. Schlücker, "Surface-Enhanced Raman Spectroscopy: Concepts and Chemical Applications", Angew. Chem. Int. Ed. **53**, 4756 (2014).

[20] W. R. Zipfel, R. M. Williams, R. Christie, A. Y. Nikitin, B. T. Hyman, and W. W. Webb, "Live tissue intrinsic emission microscopy using multiphoton-excited native fluorescence and second harmonic generation", Proc. Natl. Acad. Sci. USA **100**, 7075 (2003).

[21] S. Yue, M. N. Slipchenko, and J.-X. Cheng, "Multimodal nonlinear optical microscopy", Laser & photonics reviews **5**, 496 (2011).

[22] J. Rehbinder, L. Brückner, A. Wipfler, T. Buckup, and M. Motzkus, "Multimodal nonlinear optical microscopy with shaped 10 fs pulses", Opt. Express **22**, 28790 (2014).

[23] N. Vogler, T. Meyer, D. Akimov, I. Latka, C. Krafft, N. Bendsoe, K. Svanberg, B. Dietzek, and J. Popp, "Multimodal imaging to study the morphochemistry of basal cell carcinoma", J. Biophotonics **3**, 728 (2010).

[24] T. Meyer, N. Bergner, C. Bielecki, C. Krafft, D. Akimov, B. F. Romeike, R. Reichart, R. Kalff, B. Dietzek, and J. Popp, "Nonlinear microscopy, infrared, and Raman microspectroscopy for brain tumor analysis", J. Biomed. Opt. **16**, 021113 (2011).

[25] X. Nan, E. O. Potma, and X. S. Xie, "Nonperturbative Chemical Imaging of Organelle Transport in Living Cells with Coherent Anti-Stokes Raman Scattering Microscopy", Biophys. J. **91**, 728 (2006).

[26] R. K. Lyn, D. C. Kennedy, A. Stolow, A. Ridsdale, and J. P. Pezacki, "Dynamics of lipid droplets induced by the hepatitis C virus core protein", Biochem. Biophys. Res. Commun. **399**, 518 (2010).

[27] M. Zimmerley, R. A. McClure, B. Choi, and E. O. Potma, "Following dimethyl sulfoxide skin optical clearing dynamics with quantitative nonlinear multimodal microscopy", Appl. Opt. **48**, D79 (2009).

[28] S. Heuke, N. Vogler, T. Meyer, D. Akimov, F. Kluschke, H.-J. Röwert-Huber, J. Lademann, B. Dietzek, and J. Popp, "Multimodal mapping of human skin", British Journal of Dermatology **169**, 794 (2013).

[29] A. Zumbusch, G. R. Holtom, and X. S. Xie, "Three-Dimensional Vibrational Imaging by Coherent Anti-Stokes Raman Scattering", Phys. Rev. Lett. **82**, 4142 (1999).

[30] J.-X. Cheng, and X. S. Xie, "Coherent anti-Stokes Raman scattering microscopy: instrumentation, theory, and applications", J. Phys. Chem. B **108**, 827 (2004).

[31] A. F. Pegoraro, A. Ridsdale, D. J. Moffatt, Y. Jia, J. P. Pezacki, and A. Stolow, "Optimally chirped multimodal CARS microscopy based on a single Ti: sapphire oscillator", Opt. Express **17**, 2984 (2009).

[32] A. Volkmer, "Vibrational imaging and microspectroscopies based on coherent anti-Stokes Raman scattering microscopy", J. Phys. D: Appl. Phys. **38**, R59 (2005).

[33] C. L. Evans, and X. S. Xie, "Coherent Anti-Stokes Raman Scattering Microscopy: Chemical Imaging for Biology and Medicine", Annu. Rev. Anal. Chem. **1**, 883 (2008).

[34] J.-X. Cheng, and X. S. Xie, *Coherent Raman scattering microscopy* (CRC press, 2012).

[35] M. Wefers, and K. Nelson, "Space-time profiles of shaped ultrafast optical waveforms", IEEE J. Quantum. Electron. **32**, 161 (1996).

[36] A. M. Weiner, "Femtosecond pulse shaping using spatial light modulators", Rev. Sci. Instrum. **71**, 1929 (2000).

[37] A. Präkelt, M. Wollenhaupt, A. Assion, C. Horn, C. Sarpe-Tudoran, M. Winter, and T. Baumert, "Compact, robust, and flexible setup for femtosecond pulse shaping", Rev. Sci. Instrum. **74**, 4950 (2003).

[38] A. Monmayrant, S. Weber, and B. Chatel, "A newcomer's guide to ultrashort pulse shaping and characterization", J. Phys. B: At., Mol. Opt. Phys. **43**, 103001 (2010).

[39] W. S. Warren, H. Rabitz, and M. Dahleh, "Coherent control of quantum dynamics: the dream is alive", Science **259**, 1581 (1993).

[40] Y. Silberberg, "Quantum coherent control for nonlinear spectroscopy and microscopy", Annu. Rev. Phys. Chem. **60**, 277 (2009).

[41] N. Dudovich, D. Oron, and Y. Silberberg, "Single-pulse coherent anti-Stokes Raman spectroscopy in the fingerprint spectral region", J. Chem. Phys. **118**, 9208 (2003).

[42] A. C. Eckbreth, *Laser Diagnostics for Combustion Temperature and Species* (Abacus, 1988).

[43] A. M. Zheltikov, "Coherent anti-Stokes Raman scattering: from proof-of-the-principle experiments to femtosecond CARS and higher order wave-mixing generalizations", J. Raman Spectrosc. **31**, 653 (2000).

[44] H. Kano, and H. Hamaguchi, "Vibrationally resonant imaging of a single living cell by supercontinuum-based multiplex coherent anti-Stokes Raman scattering microspectroscopy", Opt. Express **13**, 1322 (2005).

[45] C. Krafft, B. Dietzek, M. Schmitt, and J. Popp, "Raman and coherent anti-Stokes Raman scattering microspectroscopy for biomedical applications", J. Biomed. Opt. **17**, 040801 (2012).

[46] C. H. Camp, and M. T. Cicerone, "Chemically sensitive bioimaging with coherent Raman scattering", Nat. Photonics **9**, 295 (2015).

[47] C. H. Camp, Y. J. Lee, J. M. Heddleston, C. M. Hartshorn, W. R. Hight, J. N. Rich, J. D. Lathia, and M. T. Cicerone, "High-speed coherent Raman fingerprint imaging of biological tissues", Nat. Photonics **8**, 627 (2014).

[48] I. Pope, L. Payne, G. Zoriniants, E. Thomas, O. Williams, P. Watson, W. Langbein, and P. Borri, "Coherent anti-Stokes Raman scattering microscopy of single nanodiamonds", Nat. Nanotechnol. **9**, 940 (2014).

[49] Y. Zhang, Y.-R. Zhen, O. Neumann, J. K. Day, P. Nordlander, and N. J. Halas, "Coherent anti-Stokes Raman scattering with single-molecule sensitivity using a plasmonic Fano resonance", Nat. Commun. **5** (2014).

[50] A. S. Duarte, J. Rehbinder, R. R. B. Correia, T. Buckup, and M. Motzkus, "Mapping Impurity of Single-Walled Carbon Nanotubes in Bulk Samples with Multiplex Coherent Anti-Stokes Raman Microscopy", Nano Lett. **13**, 697 (2013).

[51] R. W. Boyd, *Nonlinear optics*, 3rd ed. (Academic press, 2008).

[52] R. Brakel, and F. W. Schneider, "Polarization CARS Spectroscopy", in, edited by R. J. H. Clark, and R. E. Hester, (Wiley & Sons, 1988) Chap. 4, pp. 149–192.

[53] S. Akhmanov, A. Bunkin, S. Ivanov, and N. Koroteev, "Coherent ellipsometry of Raman scattering of light", Soviet Journal of Experimental and Theoretical Physics Letters **25**, 416 (1977).

[54] J. Song, G. Eesley, and M. Levenson, "Background suppression in coherent Raman spectroscopy", Appl. Phys. Lett. **29**, 567 (1976).

[55] J.-L. Oudar, R. W. Smith, and Y. Shen, "Polarization-sensitive coherent anti-Stokes Raman spectroscopy", Appl. Phys. Lett. **34**, 758 (1979).

[56] J.-X. Cheng, L. D. Book, and X. S. Xie, "Polarization coherent anti-Stokes Raman scattering microscopy", Opt. Lett. **26**, 1341 (2001).

[57] H. Lotem, R. T. Lynch, and N. Bloembergen, "Interference between Raman resonances in four-wave difference mixing", Phys. Rev. A **14**, 1748 (1976).

[58] J.-x. Cheng, A. Volkmer, L. D. Book, and X. S. Xie, "An epi-detected coherent anti-Stokes Raman scattering (E-CARS) microscope with high spectral resolution and high sensitivity", J. Phys. Chem. B **105**, 1277 (2001).

[59] F. M. Kamga, and M. G. Sceats, "Pulse-sequenced coherent anti-Stokes Raman scattering spectroscopy: a method for suppression of the nonresonant background", Opt. Lett. **5**, 126 (1980).

[60] A. Volkmer, L. D. Book, and X. S. Xie, "Time-resolved coherent anti-Stokes Raman scattering microscopy: Imaging based on Raman free induction decay", Appl. Phys. Lett. **80**, 1505 (2002).

[61] Y. J. Lee, and M. T. Cicerone, "Vibrational dephasing time imaging by time-resolved broadband coherent anti-Stokes Raman scattering microscopy", Appl. Phys. Lett. **92**, 041108 (2008).

[62] E. O. Potma, C. L. Evans, and X. S. Xie, "Heterodyne coherent anti-Stokes Raman scattering (CARS) imaging", Opt. Lett. **31**, 241 (2006).

[63] S.-H. Lim, A. G. Caster, and S. R. Leone, "Single-pulse phase-control interferometric coherent anti-Stokes Raman scattering spectroscopy", Phys. Rev. A **72**, 041803 (2005).

[64] B. von Vacano, and M. Motzkus, "Time-resolving molecular vibration for microanalytics: single laser beam nonlinear Raman spectroscopy in simulation and experiment", Phys. Chem. Chem. Phys. **10**, 681 (2008).

[65] B. von Vacano, T. Buckup, and M. Motzkus, "Highly sensitive single-beam heterodyne coherent anti-Stokes Raman scattering", Opt. Lett. **31**, 2495 (2006).

[66] D. Oron, N. Dudovich, and Y. Silberberg, "Femtosecond phase-and-polarization control for background-free coherent anti-Stokes Raman spectroscopy", Phys. Rev. Lett. **90**, 213902 (2003).

[67] A. Wipfler, T. Buckup, and M. Motzkus, "Multiplexing single-beam coherent anti-stokes Raman spectroscopy with heterodyne detection", Appl. Phys. Lett. **100**, 071102 (2012).

[68] J.-X. Cheng, A. Volkmer, L. D. Book, and X. S. Xie, "Multiplex coherent anti-Stokes Raman scattering microspectroscopy and study of lipid vesicles", J. Phys. Chem. B **106**, 8493 (2002).

[69] H. A. Rinia, M. Bonn, M. Müller, and E. M. Vartiainen, "Quantitative CARS spectroscopy using the maximum entropy method: the main lipid phase transition", ChemPhysChem **8**, 279 (2007).

[70] N. Dudovich, D. Oron, and Y. Silberberg, "Single-pulse coherently controlled nonlinear Raman spectroscopy and microscopy", Nature **418**, 512 (2002).

[71] B. von Vacano, W. Wohlleben, and M. Motzkus, "Single-beam CARS spectroscopy applied to low-wavenumber vibrational modes", J. Raman Spectrosc. **37**, 404 (2006).

[72] P. J. Wrzesinski, D. Pestov, V. V. Lozovoy, B. Xu, S. Roy, J. R. Gord, and M. Dantus, "Binary phase shaping for selective single-beam CARS spectroscopy and imaging of gas-phase molecules", J. Raman Spectrosc. **42**, 393 (2011).

[73] C. Rullière, *Femtosecond Laser Pulses: Principles and Experiments*, 2nd ed. (Springer, 2005).

[74] A. Wipfler, T. Buckup, and M. Motzkus, "Fast single-beam-CARS imaging scheme based on in silico optimization of excitation phases", J. Raman Spectrosc. (2015).

[75] A. Wipfler, "Nichtlineare optische Mikroskopie mit geformten Femtosekundenlaserimpulsen", PhD thesis (Universität Heidelberg, 2014).

[76] A. Wipfler, J. Rehbinder, T. Buckup, and M. Motzkus, "Full characterization of the third-order nonlinear susceptibility using a single-beam coherent anti-Stokes Raman scattering setup", Opt. Lett. **37**, 4239 (2012).

[77] A. Van Rhijn, M. Jurna, A. Jafarpour, J. Herek, and H. Offerhaus, "Phase-shaping strategies for coherent anti-Stokes Raman scattering", J. Raman Spectrosc. **42**, 1859 (2011).

[78] B. von Vacano, L. Meyer, and M. Motzkus, "Rapid polymer blend imaging with quantitative broadband multiplex CARS microscopy", J. Raman Spectrosc. **38**, 916 (2007).

[79] L. Brückner, "Multimodale nichtlineare Mikroskopie mit geformten ulktrakurzen Laserpulsen", MA thesis (Universität Heidelberg, 2012).

[80] JenoptikGmbH, *Technical Documentation SLM-640* (July 2009).

[81] B. J. Sussman, R. Lausten, and A. Stolow, "Focusing of light following a 4-f pulse shaper: Considerations for quantum control", Phys. Rev. A **77**, 043416 (2008).

[82] F. Frei, A. Galler, and T. Feurer, "Space-time coupling in femtosecond pulse shaping and its effects on coherent control", J. Chem. Phys. **130**, 034302 (2009).

[83] E. T. Nibbering, D. A. Wiersma, and K. Duppen, "Ultrafast nonlinear spectroscopy with chirped optical pulses", Phys. Rev. Lett. **68**, 514 (1992).

[84] A. Naumov, and A. Zheltikov, "Frequency–time and time–space mappings with broadband and supercontinuum chirped pulses in coherent wave mixing and pump–probe techniques", Appl. Phys. B **77**, 369 (2003).

[85] E. Gershgoren, R. A. Bartels, J. T. Fourkas, M. Murnane, and H. Kapteyn, "Simplified setup for high-resolution spectroscopy that uses ultrashort pulses", Opt. Lett. **28**, 361 (2003).

[86] T. Hellerer, A. M. Enejder, and A. Zumbusch, "Spectral focusing: High spectral resolution spectroscopy with broad-bandwidth laser pulses", Appl. Phys. Lett. **85**, 25 (2004).

[87] I. Rocha-Mendoza, W. Langbein, and P. Borri, "Coherent anti-Stokes Raman microspectroscopy using spectral focusing with glass dispersion", Appl. Phys. Lett. **93**, 201103 (2008).

[88] K. Knutsen, J. Johnson, A. Miller, P. Petersen, and R. Saykally, "High spectral resolution multiplex CARS spectroscopy using chirped pulses", Chem. Phys. Lett. **387**, 436 (2004).

[89] K. P. Knutsen, B. M. Messer, R. M. Onorato, and R. J. Saykally, "Chirped coherent anti-Stokes Raman scattering for high spectral resolution spectroscopy and chemically selective imaging", J. Phys. Chem. B **110**, 5854 (2006).

[90] R. M. Onorato, N. Muraki, K. P. Knutsen, and R. J. Saykally, "Chirped coherent anti-Stokes Raman scattering as a high-spectral-and spatial-resolution microscopy", Opt. Lett. **32**, 2858 (2007).

[91] W. Langbein, I. Rocha-Mendoza, and P. Borri, "Coherent anti-Stokes Raman micro-spectroscopy using spectral focusing: theory and experiment", J. Raman Spectrosc. **40**, 800 (2009).

[92] W. Langbein, I. Rocha-Mendoza, and P. Borri, "Single source coherent anti-Stokes Raman microspectroscopy using spectral focusing", Appl. Phys. Lett. **95**, 081109 (2009).

[93] I. Rocha-Mendoza, W. Langbein, P. Watson, and P. Borri, "Differential coherent anti-Stokes Raman scattering microscopy with linearly chirped femtosecond laser pulses", Opt. Lett. **34**, 2258 (2009).

[94] B.-C. Chen, J. Sung, and S.-H. Lim, "Chemical imaging with frequency modulation coherent anti-Stokes Raman scattering microscopy at the vibrational fingerprint region", J. Phys. Chem. B **114**, 16871 (2010).

[95] B.-C. Chen, J. Sung, X. Wu, and S.-H. Lim, "Chemical imaging and microspectroscopy with spectral focusing coherent anti-Stokes Raman scattering", J. Biomed. Opt. **16**, 021112 (2011).

[96] I. Rocha-Mendoza, P. Borri, and W. Langbein, "Quadruplex CARS microspectroscopy", J. Raman Spectrosc. **44**, 255 (2013).

[97] A. Wipfler, J. Rehbinder, T. Buckup, and M. Motzkus, "Elimination of two-photon excited fluorescence using a single-beam coherent anti-Stokes Raman scattering setup", J. Raman Spectrosc. **44**, 1379 (2013).

[98] P. K. Upputuri, L. Gong, and H. Wang, "Chirped time-resolved CARS microscopy with square-pulse excitation", Opt. Express **22**, 9611 (2014).

[99] H.-W. Wang, T. T. Le, and J.-X. Cheng, "Label-free imaging of arterial cells and extracellular matrix using a multimodal CARS microscope", Opt. Commun. **281**, 1813 (2008).

[100] H. Chen, H. Wang, M. N. Slipchenko, Y. Jung, Y. Shi, J. Zhu, K. K. Buhman, and J.-X. Cheng, "A multimodal platform for nonlinear optical microscopy and microspectroscopy", Opt. Express **17**, 1282 (2009).

[101] Y.-H. Zhai, C. Goulart, J. E. Sharping, H. Wei, S. Chen, W. Tong, M. N. Slipchenko, D. Zhang, and J.-X. Cheng, "Multimodal coherent anti-Stokes Raman spectroscopic imaging with a fiber optical parametric oscillator", Appl. Phys. Lett. **98**, 191106 (2011).

[102] N. Olivier, M. A. Luengo-Oroz, L. Duloquin, E. Faure, T. Savy, I. Veilleux, X. Solinas, D. Débarre, P. Bourgine, A. Santos, et al., "Cell lineage reconstruction of early zebrafish embryos using label-free nonlinear microscopy", Science **329**, 967 (2010).

[103] Q. Sun, Y. Li, S. He, C. Situ, Z. Wu, and J. Y. Qu, "Label-free multimodal nonlinear optical microscopy reveals fundamental insights of skeletal muscle development", Biomed. Opt. Express **5**, 158 (2014).

[104] J. Lin, F. Lu, W. Zheng, S. Xu, D. Tai, H. Yu, and Z. Huang, "Assessment of liver steatosis and fibrosis in rats using integrated coherent anti-Stokes Raman scattering and multiphoton imaging technique", J. Biomed. Opt. **16**, 116024 (2011).

[105] X. Xu, J. Cheng, M. J. Thrall, Z. Liu, X. Wang, and S. T. Wong, "Multimodal non-linear optical imaging for label-free differentiation of lung cancerous lesions from normal and desmoplastic tissues", Biomed. Opt. Express **4**, 2855 (2013).

[106] S. Postma, A. van Rhijn, J. Korterik, P. Gross, J. Herek, and H. Offerhaus, "Application of spectral phase shaping to high resolution CARS spectroscopy", Opt. Express **16**, 7985 (2008).

[107] F. Lu, W. Zheng, J. Lin, and Z. Huang, "Integrated coherent anti-Stokes Raman scattering and multiphoton microscopy for biomolecular imaging using spectral filtering of a femtosecond laser", Appl. Phys. Lett. **96**, 133701 (2010).

[108] S.-H. Lim, A. G. Caster, O. Nicolet, and S. R. Leone, "Chemical imaging by single pulse interferometric coherent anti-Stokes Raman scattering microscopy", J. Phys. Chem. B **110**, 5196 (2006).

[109] C. Müller, T. Buckup, B. von Vacano, and M. Motzkus, "Heterodyne single-beam CARS microscopy", J. Raman Spectrosc. **40**, 809 (2009).

[110] J. Rehbinder, C. Pohling, T. Buckup, and M. Motzkus, "Multiplex coherent anti-Stokes Raman microspectroscopy with tailored Stokes spectrum", Opt. Lett. **35**, 3721 (2010).

[111] C. W. Freudiger, W. Min, G. R. Holtom, B. Xu, M. Dantus, and X. S. Xie, "Highly specific label-free molecular imaging with spectrally tailored excitation-stimulated Raman scattering (STE-SRS) microscopy", Nat. Photonics **5**, 103 (2011).

[112] L. Brückner, T. Buckup, and M. Motzkus, "Enhancement of coherent anti-Stokes Raman signal via tailored probing in spectral focusing", Opt. Lett. **40**, 5204 (2015).

[113] L. Brückner, T. Buckup, and M. Motzkus, "Exploring the potential of tailored spectral focusing", J. Opt. Soc. Am. B **33**, 1482 (2016).

[114] H. Sadeghi-Jorabchi, P. Hendra, R. Wilson, and P. Belton, "Determination of the total unsaturation in oils and margarines by Fourier transform Raman spectroscopy", J. Am. Oil Chem. Soc. **67**, 483 (1990).

[115] I. Pope, W. Langbein, P. Watson, and P. Borri, "Simultaneous hyperspectral differential-CARS, TPF and SHG microscopy with a single 5 fs Ti: Sa laser", Opt. Express **21**, 7096 (2013).

[116] A. H. Zewail, "Femtochemistry: Atomic-Scale Dynamics of the Chemical Bond", J. Phys. Chem. A **104**, 5660 (2000).

[117] J. L. Herek, W. Wohlleben, R. J. Cogdell, D. Zeidler, and M. Motzkus, "Quantum control of energy flow in light harvesting", Nature **417**, 533 (2002).

[118] T. Buckup, and M. Motzkus, "Multidimensional Time-Resolved Spectroscopy of Vibrational Coherence in Biopolyenes", Annu. Rev. Phys. Chem. **65**, 39 (2014).

[119] A. Lohner, P. Kruck, and W. Rühle, "Generation of 200 femtosecond pulses tunable between 2.5 and 5.5 μm", Appl. Phys. B **59**, 211 (1994).

[120] J. M. Fraser, D. Wang, A. Haché, G. R. Allan, and H. M. van Driel, "Generation of high-repetition-rate femtosecond pulses from 8 to 18 μm", Appl. Opt. **36**, 5044 (1997).

[121] S. Ehret, and H. Schneider, "Generation of subpicosecond infrared pulses tunable between 5.2 μm and 18 μm at a repetition rate of 76 MHz", Appl. Phys. B: Lasers Opt. **66**, 27 (1998).

[122] G. Cerullo, and S. De Silvestri, "Ultrafast optical parametric amplifiers", Rev. Sci. Instrum. **74**, 1 (2003).

[123] S. M. Foreman, D. J. Jones, and J. Ye, "Flexible and rapidly configurable femtosecond pulse generation in the mid-IR", Opt. Lett. **28**, 370 (2003).

[124] M. R. de Barros, R. S. Miranda, T. M. Jedju, and P. C. Becker, "High-repetition-rate femtosecond mid-infrared pulse generation", Opt. Lett. **20**, 480 (1995).

[125] R. Kaindl, D. Smith, M. Joschko, M. Hasselbeck, M. Woerner, and T. Elsaesser, "Femtosecond infrared pulses tunable from 9 to 18 μm at an 88-MHz repetition rate", Opt. Lett. **23**, 861 (1998).

[126] R. Kaindl, F. Eickemeyer, M. Woerner, and T. Elsaesser, "Broadband phase-matched difference frequency mixing of femtosecond pulses in GaSe: experiment and theory", Appl. Phys. Lett. **75**, 1060 (1999).

[127] F. Eickemeyer, R. Kaindl, M. Woerner, T. Elsaesser, and A. Weiner, "Controlled shaping of ultrafast electric field transients in the mid-infrared spectral range", Opt. Lett. **25**, 1472 (2000).

[128] T. Zentgraf, R. Huber, N. C. Nielsen, D. S. Chemla, and R. A. Kaindl, "Ultrabroadband 50-130 THz pulses generated via phase-matched difference frequency mixing in LiIO 3", Opt. Express **15**, 5775 (2007).

[129] J. E. Midwinter, and J. Warner, "The effects of phase matching method and of uniaxial crystal symmetry on the polar distribution of second-order non-linear optical polarization", Br. J. Appl. Phys. **16**, 1135 (1965).

[130] T. Baumert, T. Brixner, V. Seyfried, M. Strehle, and G. Gerber, "Femtosecond pulse shaping by an evolutionary algorithm with feedback", Appl. Phys. B: Lasers Opt. **65**, 779 (1997).

[131] D. Zeidler, S. Frey, K.-L. Kompa, and M. Motzkus, "Evolutionary algorithms and their application to optimal control studies", Phys. Rev. A **64**, 023420 (2001).

[132] J. P. Foing, J. P. Likforman, M. Joffre, and A. Migus, "Femtosecond pulse phase measurement by spectrally resolved up-conversion: application to continuum compression", IEEE J. Quantum. Electron. **28**, 2285 (1992).

[133] M. Joffre, A. Bonvalet, A. Migus, and J.-L. Martin, "Femtosecond diffracting Fourier-transform infrared interferometer", Opt. Lett. **21**, 964 (1996).

[134] J. Köhler, M. Wollenhaupt, T. Bayer, C. Sarpe, and T. Baumert, "Zeptosecond precision pulse shaping", Opt. Express **19**, 11638 (2011).

[135] B. von Vacano, T. Buckup, and M. Motzkus, "In situ broadband pulse compression for multiphoton microscopy using a shaper-assisted collinear SPIDER", Opt. Lett. **31**, 1154 (2006).

[136] B. von Vacano, T. Buckup, and M. Motzkus, "Shaper-assisted collinear SPIDER: fast and simple broadband pulse compression in nonlinear microscopy", J. Opt. Soc. Am. B **24**, 1091 (2007).

[137] D. Oron, N. Dudovich, and Y. Silberberg, "Single-pulse phase-contrast nonlinear Raman spectroscopy", Phys. Rev. Lett. **89**, 273001 (2002).

[138] Y. Liu, M. D. King, H. Tu, Y. Zhao, and S. A. Boppart, "Broadband nonlinear vibrational spectroscopy by shaping a coherent fiber supercontinuum", Opt. Express **21**, 8269 (2013).

[139] C. L. Evans, E. O. Potma, and X. S. Xie, "Coherent anti-Stokes Raman scattering spectral interferometry: determination of the real and imaginary components of nonlinear susceptibility χ (3) for vibrational microscopy", Opt. Lett. **29**, 2923 (2004).

[140] M. Jurna, J. Korterik, C. Otto, J. Herek, and H. Offerhaus, "Background free CARS imaging by phase sensitive heterodyne CARS", Opt. Express **16**, 15863 (2008).

[141] L. Lepetit, G. Cheriaux, and M. Joffre, "Linear techniques of phase measurement by femtosecond spectral interferometry for applications in spectroscopy", J. Opt. Soc. Am. B **12**, 2467 (1995).

[142] G. Thalhammer, R. W. Bowman, G. D. Love, M. J. Padgett, and M. Ritsch-Marte, "Speeding up liquid crystal SLMs using overdrive with phase change reduction", Opt. Express **21**, 1779 (2013).

[143] D. J. Kane, and R. Trebino, "Characterization of arbitrary femtosecond pulses using frequency-resolved optical gating", IEEE J. Quantum. Electron. **29**, 571 (1993).

[144] C. Iaconis, and I. A. Walmsley, "Spectral phase interferometry for direct electric-field reconstruction of ultrashort optical pulses", Opt. Lett. **23**, 792 (1998).

[145] G. Stibenz, and G. Steinmeyer, "Interferometric frequency-resolved optical gating", Opt. Express **13**, 2617 (2005).

[146] A. Galler, and T. Feurer, "Pulse shaper assisted short laser pulse characterization", Appl. Phys. B **90**, 427 (2008).

[147] V. V. Lozovoy, I. Pastirk, and M. Dantus, "Multiphoton intrapulse interference. IV. Ultrashort laserpulse spectral phase characterization and compensation", Opt. Lett. **29**, 775 (2004).

[148] V. V. Lozovoy, B. Xu, Y. Coello, and M. Dantus, "Direct measurement of spectral phase for ultrashort laser pulses", Opt. Express **16**, 592 (2008).

[149] T. Hornung, "Amplituden- und Phasenmodulation von ultrakurzen Lichtimpulsen mit einer Flüssigkristallmaske und ihre Anwendung zur Kontrolle von Photonenübergängen in Na", MA thesis (Max-Planck-Institute for Quantum Optics, 1999).

Danksagung

An erster Stelle möchte ich mich ganz besonders bei Herrn Prof. Dr. Marcus Motzkus bedanken, der mir eine Dissertation auf diesem äußerst interessanten und vielseitigen Forschungsgebiet ermöglicht hat. Besonders seine Begeisterungsfähigkeit für alle Facetten und Details des ‘Pulse-Shaping‘ sowie sein ansteckender Enthusiasmus haben diese Arbeit stark geprägt und so manche Entwicklung überhaupt erst möglich gemacht.

Für die bereitwillige Übernahme des Zweitgutachtens danke ich Herrn Prof. Dr. Dirk-Peter Herten.

Auch möchte ich mich bei Dr. Tiago Buckup bedanken, dessen Tür stets für Diskussionen offen stand und der immer ein paar Lösungsvorschläge parat hatte.

Jean Rehbinder möchte ich für die Einarbeitung und intensive Zusammenarbeit während meiner Masterarbeit und weit darüber hinaus danken. Die exzellente Unterhaltung, vor allem durch allerlei Wortschöpfungen und Geschichten soll nicht unerwähnt bleiben. Mit Alexander Wipfler habe ich viele Stunden im Labor verbracht. Ihm danke ich vor allem für die Ideen und Anregungen sowie seine Hilfsbereitschaft zum Beginn meiner Doktorarbeit. Die gemeinsamen Zeiten mit euch – damals als ‚der Botanik‘ noch angerufen hat – werden mir definitiv in Erinnerung bleiben.

Hans-Robert Volpp möchte ich für die witzigen Geschichten danken, welche jeden Gruppenausflug zum Erlebnis werden lassen.

Meinen langjährigen Bürokollegen Elisabeth Brühl und Takeshi Miki danke ich für die gemeinsame Zeit und die gute Arbeitsatmosphäre und Man Jiang für die netten Gespräche im Arbeitsalltag.

Julia Herz danke ich für die unermüdliche Unterstützung während der gesamten Doktorarbeit. Unabhängig von Ihrer Arbeitslast war sie immer für mich da. Vor allem ihr Humor und ihre lockere Art sind eine echte Bereicherung für jede Gruppe.

An dieser Stelle wird es endlich mal Zeit, meiner Familie und natürlich meinen Eltern im Speziellen zu danken. Ich bin froh, dass ich euch habe und ich mich immer auf euch verlassen kann. Ich konnte stets das tun, worauf ich Lust hatte und ihr habt es überhaupt erst möglich gemacht - danke!

Eidesstattliche Versicherung gemäß §8 der Promotionsordnung der Naturwissenschaftlich-Mathematischen Gesamtfakultät der Universität Heidelberg

1. Bei der eingereichten Dissertation zu dem Thema "Exploring the Potential of Nonlinear Optical Microscopy with Tailored Femtosecond Pulses" handelt es sich um meine eigenständig erbrachte Leistung.

2. Ich habe nur die angegebenen Quellen und Hilfsmittel benutzt und mich keiner unzulässigen Hilfe Dritter bedient. Insbesondere habe ich wörtlich oder sinngemäß aus anderen Werken übernommene Inhalte als solche kenntlich gemacht.

3. Die Arbeit oder Teile davon habe ich bislang nicht an einer Hochschule des In- oder Auslands als Bestandteil einer Prüfungs- oder Qualifikationsleistung vorgelegt.

4. Die Richtigkeit der vorstehenden Erklärungen bestätige ich.

5. Die Bedeutung der eidesstattlichen Versicherung und die strafrechtlichen Folgen einer unrichtigen oder unvollständigen eidesstattlichen Versicherung sind mir bekannt.

   Ich versichere an Eides statt, dass ich nach bestem Wissen die reine Wahrheit erklärt und nichts verschwiegen habe.